Transverse Shear Microscopy: A Novel Microstructural Probe for Organic Semiconductor Thin Films

A DISSERTATION
SUBMITTED TO THE FACULTY OF THE GRADUATE SCHOOL
OF THE UNIVERSITY OF MINNESOTA
BY

Vivek Kalihari

IN PARTIAL FULFILLMENT OF THE REQUIREMENTS
FOR THE DEGREE OF
DOCTOR OF PHILOSOPHY

Adviser: C. Daniel Frisbie

July 2010

Acknowledgements

I would like to start by thanking my advisor Dan Frisbie, who has helped me become a better scientist during the five years at University of Minnesota. He has been a great source of ideas and knowledge during my thesis and taught me how to approach a problem scientifically. He also helped me become a much more confident public speaker and always encouraged me to become a well-rounded materials scientist. His reliable constant support and guidance is the reason I was able to finish my thesis project satisfactorily and timely. I am grateful to Dr. Greg Haugstad for the help and guidance he provided me through out my thesis. I definitely consider him as my “unofficial” co-advisor. He taught me a lot about the AFM technique, which was the heart and soul of my thesis project, and also helped me in analyzing a lot of experimental data.

I am grateful to all the collaborators for their assistance in completing my research projects: Prof. Ellad Tadmor for helping me derive the complex mathematical equations for TSM signal; Dr. Primoz Ribic for collaboration in the polymeric substrates project; Dr. Jinping Dong for teaching me a variety of characterization techniques such as Raman, FTIR, and friction force microscopy; David Ellison for Kelvin probe force microscopy; Yu Xia and Wei Xie for synthesizing various organic semiconductor single crystals for my experiments; Mandy Woo for helping me out in studying the organic semiconductor thin film growth on different insulating substrates. I would also like to specially thank former Frisbie group member Kanan Puntambekar for “passing on” this wonderful and exciting project to me. I would like to thank all the Frisbie group members, both former and present, for being a wonderful source of research ideas and for the help in maintaining various group instruments: Matt Panzer, Xiuyu Cai, Lei Dao, Bong Soo Kim, Seongho Choi, Bryan Boudoris, Jiyoul Lee, Jeongho Cho, Derek Stevens, Yan Liang, Mingjing Ha, Bryan Paulson, Moon Sung Kang, Keun Hyung Lee, Sipei Zhang, Salil Bapat and Yanfei.

Finally I would like to thanks my parents, Mr. H. R. Kalihari and Mrs. Shakun Kalihari and my wife Disha Kalihari for always encouraging me to move forward and providing me the constant support I needed to complete my PhD thesis.

Dedication

This dissertation is dedicated to my dad Mr. H. R. Kalihari, my mom Mrs. Shakun Kalihari, and my lovely wife Mrs. Disha Kalihari

Abstract

The microstructure of ultrathin organic semiconductor films (1-2nm) on gate dielectrics plays a pivotal role in the electrical transport performance of these films in organic field effect transistors. Similarly, organic/organic interfaces play a crucial role in organic solar cells and organic light emitting diodes. Therefore, it is important to study these critical organic interfaces in order to correlate thin film microstructure and electrical performance. Conventional characterization techniques such as SEM and TEM cannot be used to probe these interfaces because of the requirement of conducting substrates and the issue of beam damage.

Here, we introduce a novel contact mode variant of atomic force microscopy, termed transverse shear microscopy (TSM), which can be used to probe organic interfaces. TSM produces striking, high contrast images of grain size, shape, and orientation in ultrathin films of polycrystalline organic materials, which are hard to visualize by any other method. It can probe epitaxial relationships between organic semiconductor thin film layers, and can be used in conjunction with other techniques to investigate the dependence of thin film properties on film microstructure. In order to explain the TSM signal, we used the theory of linear elasticity and developed a model that agrees well with the experimental findings and can predict the signal based on the components of the in-plane elastic tensor of the sample. TSM, with its ability to image elastic anisotropy at high resolution, can be very useful for microstructural characterization of soft materials, and for understanding bonding anisotropy that impacts a variety of physical properties in molecular systems.

Table of Contents

List of Tables

List of Figures

Chapter 1

INTRODUCTION

Organic electronics is emerging as a viable option for creating new and improved electrical and optical products. The excitement in the organic electronics field stems from its innovative devices and components which are derived from tailored organic materials. The extensive scope of organic electronics includes illumination, information displays,[1]energy sources,[2] sensors, actuators and radio frequency identification tags.[3] The compatibility of organic materials with plastic substrates makes these materials an excellent choice for low cost and easily processable flexible electronics.[4,5]

Identifying specific microstructure-property relationships in polycrystalline organic semiconductor films is a key goal for the field of organic electronics.[6,7,8] Polycrystalline organic semiconductor films play a central role in different device structures because their inherent order, relative to amorphous films, facilitates more efficient charge transport. Carrier mobilities in crystalline organic semiconductors are generally at least a factor of one hundred greater than in their amorphous counterparts, which is attractive for certain device applications, such as organic thin film transistors (OTFTs), where higher charge mobilities result in better performance.[9,10,11,12,13]

In an OTFT, the current modulation is restricted to the accumulation layer, which corresponds to a few monolayers of organic semiconductor on top of the gate dielectric.[14,15]As a result, it is the crystalline packing and microstructure of the first few molecular monolayers of organic semiconductor immediately adjacent to the dielectric surface that are critical for transistor performance. Organic interfaces are also important in determining the performance of other device structures such as organic solar cells and organic light emitting diodes.[16,17] In a typical organic bilayer solar cell, it is the interface of donor and acceptor thin films where the charge separation takes place resulting in a current. Similarly, in an organic light emitting diode, it is the interface of conductive layer and emissive layer where the charges of opposite sign recombine resulting in light emission.

Any structural disorder in these ultrathin organic semiconductor films near the interface, such as dislocations, impurities, or grain boundaries, can hamper the charge transport and can significantly affect device performance. For example, in an OTFT, structural disorder in thin films can reduce the saturation current, increase the threshold voltage and increase the response time, which are all detrimental to the transistor performance. Indeed, recognition of the importance of microstructure has lead to extensive structural characterization of organic semiconductor films by X-ray diffraction[18,19,20,21] and electron,[22,23,24] and scanning probe microscopy.[25,26,27,28,29] Yet there are still many aspects of organic semiconductor microstructure that are not well understood and detailed correlations with transport are rare. One surprising bottleneck to understanding microstructure-property relationships has been the difficulty of producing clear images of grains in extremely thin, coalesced layers of organic semiconductors on technologically relevant substrates.

In my thesis, I have worked towards developing a new variant of contact mode atomic force microscopy (AFM), called transverse shear microscopy (TSM),[30,31,32,33,34] which can be used to probe microstructure of ultrathin organic semiconductor films near the interface. TSM produces striking, high contrast images of grain size, shape, and *orientation* in films of polycrystalline organic materials. The grain orientation mapping by TSM can be employed to quantify grain morphology, grain boundary density and the relative proportion of high- and low-angle grain boundaries in ultra-thin organic semiconductor monolayers.[32] TSM can also probe epitaxial relationships between organic semiconductor thin film layers. It can be used in conjunction with other surface characterization techniques such as friction force microscopy (FFM) and Kelvin probe force microscopy (KFM) to investigate the dependence of thin film properties such as friction and surface electrostatic potential on film microstructure.[33] The thesis project also involved understanding the fundamental physics of the novel TSM method by comparing it with widely used FFM. We have modeled the TSM signal based on the theory of linear elasticity, which proves that the TSM signal is sensitive to elastic anisotropy at the sample surface.[34] Further, we also developed a model for strain and interfacial reconstruction for organic semiconductor thin films near the interface in order to rationalize the observed homo-epitaxial and thin film growth mode transitions.

Thesis Organization:

Chapter 2: This is a background chapter that discusses various intermolecular forces present in organic solids and different molecular packing arrangements. It gives a synopsis of possible thin film growth mechanisms and describes basic rate equations that govern nucleation and growth in organic thin films. Basic differences between an organic and an inorganic thin film growth are also highlighted. A summary of pentacene (a benchmark p-type organic semiconductor) sub-monolayer growth on various insulating substrates as a function of deposition parameters is presented.

Chapter 3: The chapter mainly discusses the origin of friction measured by FFM. As the TSM is new and still in its developmental stage, there is not enough literature that describes the fundamentals of this novel technique. This chapter is an attempt to familiarize the reader with the basic concepts and applications of contact mode FFM, which is similar to TSM in terms of the working mechanism.

Chapter 4: The work described in this chapter has been published as "Distinguishing Elastic Shear Deformation from Friction on the Surfaces of Molecular Crystals", *Physical Review Letters* **104** (2010). The chapter gives an introduction to the working mechanism of TSM. It highlights the non-activated behavior of TSM, compared to the activated FFM signal. A mechanical model describing the origin of TSM signal is also discussed and a comparison is drawn between the modeled data and the experimental findings.

Chapter 5: The work described in this chapter has been published as "Grain Orientation Mapping of Polycrystalline Organic Semiconductor Films by Transverse Shear Microscopy", *Advanced Materials,* **20** (2008). The chapter describes the microstructure characterization of polycrystalline monolayer thick pentacene films. Pentacene single crystal measurements are reported in order to generate grain orientation maps for polycrystalline monolayer films. Further, monolayer microstructure is quantified in terms of grain orientation, grain size, grain shape, and grain boundary angles.

Chapter 6: The work described in this chapter has been published as "Observation of Unusual Homoepitaxy in Ultrathin Pentacene Thin Films and Correlation with Surface Electrostatic Potential", *Advanced Materials* **21** (2009). For the first time, an unusual non commensurate homo-epitaxy in pentacene thin films near the SiO_2 interface has been reported. The TSM is used in conjunction with other surface characterization techniques such as FFM and KFM to investigate the friction and electrostatic surface potential dependence on the observed mode of epitaxy.

Chapter 7: The work described in this chapter is a part of a submitted manuscript titled "Strain Induced Homo-Epitaxial Transitions and the Growth Mode of Organic Semiconductor Thin Films". The chapter discusses a strain model developed for rationalizing the observed homo-epitaxial and thin film growth mode transitions during the initial growth of organic semiconductor thin films. We have also investigated the generality of the observed microstructure transitions by performing TSM analysis on a variety of organic semiconducting thin films on different substartes.

Chapter 8: The future work describes two current projects. The first project is related to the friction and TSM studies of organic semiconductor single crystals and the second project involves the TSM studies of crystalline semiconducting polymer films.

Chapter 2

Organic Semiconductors: Thin Film Deposition and Various Growth Mechanisms

Understanding the correlation between morphology and electronic behavior of organic semiconductor thin films requires an intensive study of different growth mechanisms found in organic thin films. The first part of the chapter describes different types of bonding that hold the molecules together in organic solids. The second part discusses first principle rate equations governing nucleation density and subsequent growth of thin films on solid substrates. It also describes some common growth modes observed in thin films. The final section of the chapter concentrates specifically on the literature related to the initial growth of pentacene (a benchmark organic semiconductor) thin films on a variety of insulating substrates.

2.1 Organic Semiconductors: Types of Bonding and Molecular Packing

Solid state molecular packing and the type of bonding, in general, determine the electronic properties of semiconductors. For organic semiconductors, it plays an important role because of the weak forces holding the molecules together as compared to their inorganic counterparts where the atoms are strongly held together by strong covalent bonds. In inorganic semiconductors, the strong interactions in the form of covalent bonds give rise to a three dimensional network of interconnected atoms resulting in highly delocalized charge carriers and large mobility of charge carriers. While in organic semiconductors, a large delocalization of charge carriers is not possible because each molecule is bonded to others via weak forces, like London and quadrupolar forces. All organic semiconductors are conjugated molecules and some are crystalline with a high degree of π overlap between molecules. The π overlap between the molecules depends on the packing symmetry[35] and provides delocalized states for charge carriers and an efficient pathway for electrons and holes. There is a significant difference between the conductivity values of organic and inorganic semiconductors. For example, anthracene (an organic semiconductor) has a typical room temperature conductivity of ~ 10^{-22} (ohm-cm)$^{-1}$ and the corresponding value for undoped germanium (an inorganic semiconductor) is ~ 10^{-2}(ohm-cm)$^{-1}$.[36] Some common organic semiconductors are shown in Fig. 2.1.

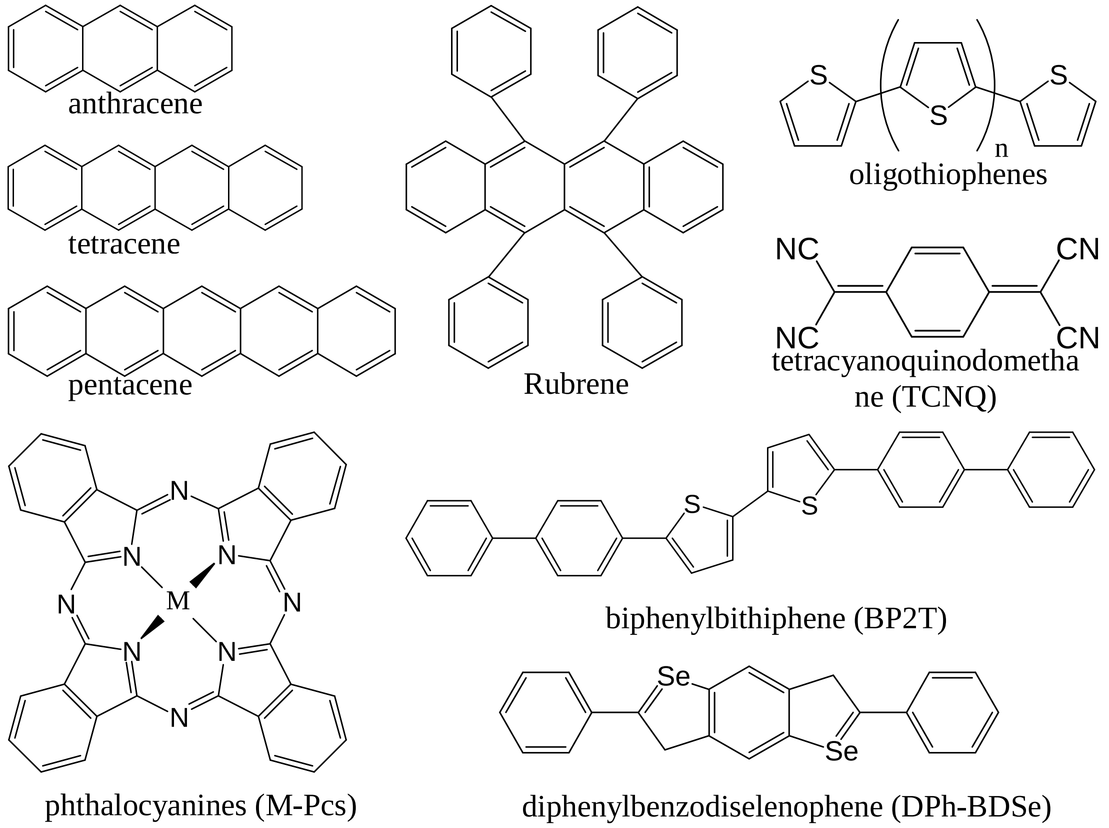

Figure 2.1 Chemical structures of common organic semiconductors

There are two classes of organic semiconductors: polymers and small molecules. Polymers are generally solution processed and give either amorphous or semi-crystalline films, while most of the small molecules are thermally evaporated resulting in polycrystalline or single crystal films. Polymers usually exhibit lower mobility because of the lower crystallinity and inefficient packing which results in weaker π overlap between the polymeric chains.[37] For example, the mobility of holes in small molecules is about two orders of magnitude greater than that in conducting polymers. Small molecules typically consist of low molecular weight oligomers and fused aromatics.

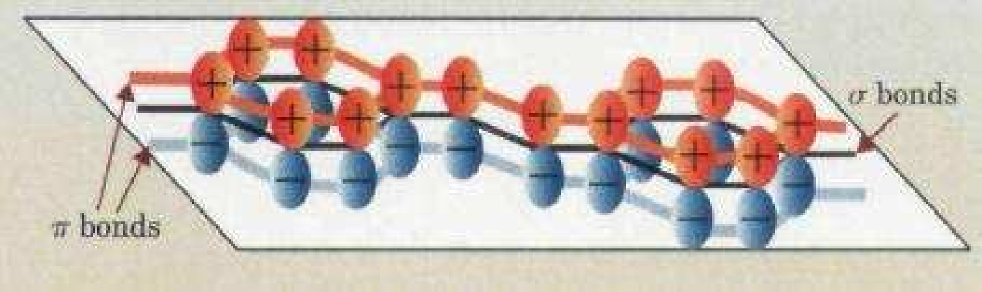

Figure 2.2 poly(p-phenylene vinylene) (PPV): π molecular orbital[36]

The charge transport in organic molecules contains two separate processes: intramolecular transport and intermolecular transport. Intramolecular transport is feasible along the so called conjugated bond (*i.e.,* alternating sequence of single and double bonds, such as the aromatic rings and polyacetylene chains). Electrons in the π-orbital are easy to excite, and therefore contribute to the fast charge transport along the conjugated bonds of the molecule.

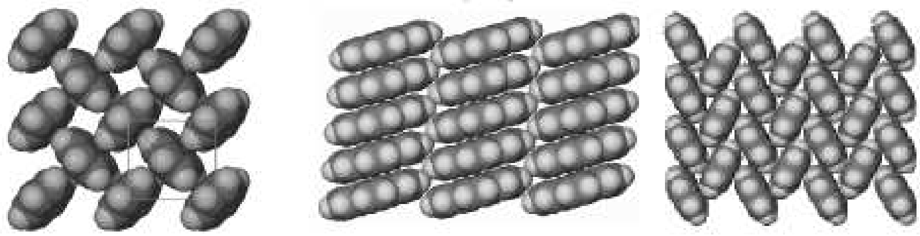

Figure 2.3 Three possible packings in organic molecules: edge-to-face (left), π-stack (middle) and herringbone (right)

(a) London Forces

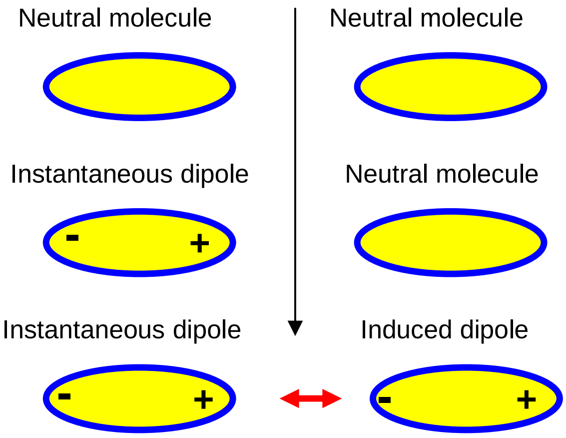

(b) Quadrupolar Forces

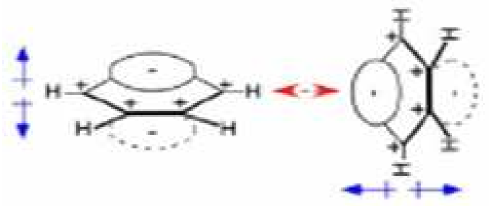

Figure 2.4 Competing forces in organic molecules, where red arrows show the dominating interaction. (a) Schematic shows the origin of London force and the resultant π stack arrangement, and (b) origin of quadrupolar force and the resultant edge-to-face packing motif[38]

Crystallization in organic solids is an interplay between weak forces such as London forces, quadrupole forces, charge transfer induced interactions and hydrogen bonding. London force arises from the instantaneous electron density shift in a molecule, which induces a dipole in the neighboring molecule. The attractive interaction between the two dipoles is termed as London force. π electron delocalization on top and bottom faces of a molecule, along with slightly positive backbone results in two back-to-back permanent dipole moments, as shown in Fig. 2.4. This configuration gives rise to a quadrupole and the molecules prefer edge-to-face alignment as the like charges repel each other. Dominating quadrupolar interaction results in edge-to-face packing motif, while stronger London interaction results in π stack packing motif.

Herringbone packing is an intermediate packing where both the London and quadrupolar forces are comparable, as shown in Fig. 2.3. Family of acenes[39] and thiophenes[40] pack in a herringbone arrangement, DMCT[41] and series of PTCDI[42] derivates are π stacked structures and benzene exhibits edge-to-face packing motif. All the molecular arrangements lack in symmetry which results in anisotropic mobility of charge carriers in organic semiconductors.

2.2 Ultra Thin Film Growth: Atomistic View

Growth of thin films from the vapor phase is a non-equilibrium phenomenon. Growth mechanism and resulting film morphology depends on the outcome of the competition between thermodynamics and kinetics of the thin film growth. Understanding the basic physics of the thin film growth is critical in order to tailor make the desired quality of films.

2.2.1 Growth Modes

There are three modes of thin film growth on solid substrates as shown in Fig. 2.5: layer-by-layer mode (the Frank-van der Merwe mode), layer-plus-island mode (the Stranski-Krastanov mode) and island mode (the Volmer-Weber mode). When the interaction between an adsorbed molecule and the substrate is stronger than the interaction between two molecules, molecules nucleate on the substrate forming 2-D island and grow laterally until islands completely coalesce. Only after the completion of the first monolayer, second monolayer islands nucleate on the first layer and follow the same growth process giving rise to layer-by-layer growth. In the island growth mode, small clusters nucleate on the substrate and start growing into 3-D islands of the condensed phase without waiting for the lower layers to completely coalesce as shown in the Fig. 2.5. This mode is favored when the interaction between adsorbed molecules is stronger than the molecule-substrate interaction.

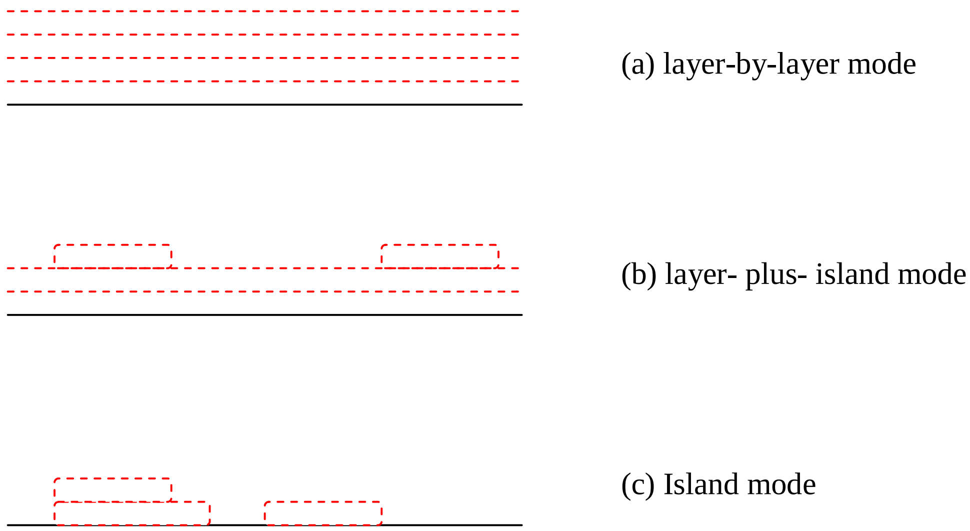

Figure 2.5 Thin film growth modes. (a) layer-by-layer, (b) layer plus island, and (c) island mode

The third mode, layer plus island growth mode is an intermediate case. Growth follows layer-by-layer growth for a single monolayer or a few monolayers and then 3-D islands start growing on top of the 2-D grown layers, *i.e.*, there is a shift in the growth mode from 2-D to 3-D. Possible reasons for the growth mode shift can be lattice mismatch or orientation mismatch with respect to the substrate, which cannot be continued to the bulk phase, resulting in high energy interface and finally leading to island formation. Film growth by the Stranski-Krastanov mode is fairly common and is observed in many metal-metal and metal-semiconductor systems.[43]

Young's equation also provides a criterion to distinguish and understand the three modes of thin film growth.

$$\gamma_{sv} < \gamma_{fs} + \gamma_{fv} \text{ ....(island growth)}$$

$$\gamma_{sv} \geq \gamma_{fs} + \gamma_{fv} \text{ ....(layer by layer growth)}$$

where γ_{sv} = substrate-vapor surface energy

γ_{fs} = substrate-film surface energy

γ_{fv} = film-vapor surface energy

For the Stranski-Krastanov growth, initially at least, layer-by-layer growth condition applies, but after a few monolayers high energy at the deposit intermediate-layer interface triggers island formation.[44]

2.2.2 Atomistic Processes

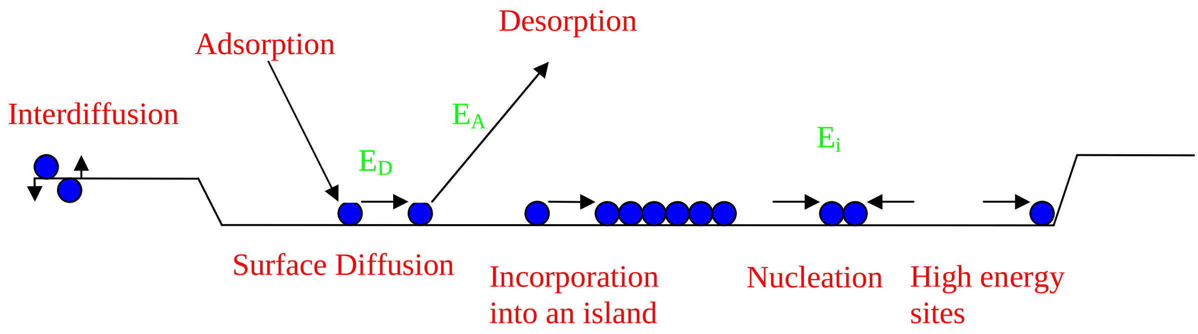

Figure 2.6 Atomic processes and characteristic energies involved in nucleation and growth

During thin film deposition when a molecule gets adsorbed from the vapor phase onto a substrate, it keeps diffusing on the substrate until it is lost by any one of these modes: (i) gets desorbed from the substrate back to the vapor phase, (ii) nucleates 2-D or 3-D islands by combining with other moving molecules on the substrate, (iii) gets captured by the existing islands, (iv) diffuses into the substrate, or (v) gets captured by a high energy site such as a step. Different energies shown in Fig. 2.6 are:

(i) E_D = Activation energy for diffusion of molecules on the substrate, depends on the size of the molecule and the molecule-substrate interaction

(ii) E_A = Activation energy for desorption, depends on the amount of supersaturation and the molecule-substrate interaction

(iii) E_i = It is defined as the difference in free energy between i adsorbed molecules on the substrate (non-interacting) and i molecules forming an island. It depends on both the substrate-molecule and the molecule-molecule interactions. Critical number i is a critical cluster size and represents that any nucleating island having i atoms is the most unstable: clusters having more than i molecules tend to grow while the clusters having less than *i* molecules will decay, in order to minimize their excess free energies.[45]

Relative contribution of each process on the overall growth depends on the single molecule concentration on the substrate, substrate coverage and the temperature of the substrate. As mentioned earlier, film deposition from the vapor phase is a non-equilibrium phenomenon. All the processes shown in the Fig. 2.6 are re-arrangement processes. Unstable clusters formed at various stages of growth can re-arrange in many ways like island shape change due to edge diffusion, downward transfer of molecules impinging on top of the existing islands, annealing of defects *etc*. Diffusion thus occurs at various stages of film growth: the motion of single molecules to form clusters, the mobility of clusters themselves and the edge diffusion during coalescence of islands.

2.2.3 Thermodynamics and Kinetics

Various thermodynamic and kinetic processes compete at different stages of thin film growth. The principle of detailed balance is important in describing the properties of thermodynamic equilibrium state. In order to have an adsorption equilibrium, surface processes such as condensation, desorption, growth and decay of 2-D or 3-D islands should balance each other. Net growth is zero and the system can be denoted by a set of intensive variables such as pressure and temperature, even though the system is continuously changing at a microscopic level.[46]

Thin film growth, on the contrary, is a non-equilibrium kinetic process. The final state of the system does not depend on the intensive macroscopic variables but depend on the path taken to reach that state. The states may not be thermodynamically stable, *i.e.*, in their lowest free energy configuration, but are kinetically favored. Some of the kinetic rate limiting processes elucidating the non-equilibrium nature of the film growth are as follows:

(i) In diffusion limited aggregation, surface diffusion of molecules on a substrate is the dominating mechanism which governs the growth rate and shape of islands. Mostly, the islands grow as dendrite which is not thermodynamically stable.

(ii) Nucleation is toughest on inert, atomically flat surfaces. The rate limiting step is the formation of small clusters which can grow because their high surface to volume ratio increases free energy.[47]

2.2.4 Nucleation and Growth: Rate Equations

The submonolayer film growth on solid substrates can be described as follows: when a substrate is exposed to the incident vapor, the molecules get adsorb on the substrate and form clusters or islands. At this stage the prior nuclei incorporates impinging molecules and sub-critical clusters grow in size while the island density rapidly saturates. This is followed by the growth of stable clusters. The next stage is the merging of the growing islands by coalesce phenomenon. Crystallographic facets and orientations are generally preserved on islands during the coalescence. Continued coalescence results in network formation resulting in channel voids. With further deposition, channels fill in leaving voids behind. Finally even the voids fill up and the film is said to be continuous.

In this subsection, few important rate equations related to submonolayer growth are discussed with emphasis on the physical concepts behind them rather than the rigorous mathematics involved in deriving them. Assuming that only single molecules are mobile on the substrate, the nucleation and formation of the first monolayer can be understood with the help of the following equations:

$$\frac{dn_1}{dt} = R - \frac{n_1}{\tau_a} - 2U_1 - \sum_{j=2}^{\infty} U_j \tag{2.1}$$

$$\frac{dn_j}{dt} = U_{j-1} - U_j \tag{2.2}$$

Where n_1 and n_j are concentration per unit area of molecules and of clusters of size j respectively, R is the incident flux of molecules per unit area per unit time, τ_a is the mean re-evaporation time, U_j is the capture rate of molecules by an island of size j. Dividing clusters into stable ($j > i$) and unstable ($j \le i$) and defining n_x as the sum of all the stable clusters via $n_x = \sum_{j=i+1}^{\infty} n_j$, the above equations (2.1 and 2.2) can be simplified to:

$$\frac{dn_1}{dt} = R - \frac{n_1}{\tau_a} - \frac{d(n_x w_x)}{dt} \tag{2.3}$$

$$\frac{dn_j}{dt} = 0 \qquad (2 \le \mathrm{j} \le \mathrm{i}) \tag{2.4}$$

$$\frac{dn_x}{dt} = U_i - U_c - U_m \tag{2.5}$$

The last term in equation 2.3 represents the loss of admolecules to n_x stable clusters with an average number of w_x molecules per cluster. As stated earlier, clusters with size $j < i$ are not stable and will decay with time resulting in equation 2.4. The last two terms in equation 2.5 deals with coalescence: if stable clusters impinge on each other by growth (U_c) or by mobility across the substrate (U_m), then the number of stable clusters will reduce. The term U_i in equation 2.5 is the nucleation rate.[48]

$$\frac{d(n_x w_x)}{dt} = (i+1)U_i + \sigma_x D.n._1.n._x + RZ \qquad (2.6)$$

The above equation 2.6 governs the growth process of stable clusters on a substrate. The three terms on the right hand side of equation 2.6 represents, respectively, the contribution of nucleation, capture by surface diffusion and direct impingement on growing clusters which cover a fraction Z on the surface. The capture number σ_x represents the diffusional flow of admolecules to stable clusters. The nucleation term is always negligible during the growth process and the last term dominates only at high coverages, especially at higher temperatures when the diffusive flow of the admolecules is limited by fast re-evaporation. If the nucleation is not biased (*i.e.,* no surface impurities or high energy steps on the surface) and only single admolecules are mobile on the surface, the nucleation and growth can be predicted based on the above described rate equations. Various important parameters such as E_a, E_d, E_i and i can be calculated by measuring the nucleation rate dependence on deposition rate, temperature and time.

Any growth process can be classified as one of the three regimes of condensation: extreme incomplete, initially incomplete and complete, based on the discussed rate equations. The general equation for the nucleation density is given by:

$$\frac{n_x(Z)}{N_o} \approx \left(\frac{R}{N_o}\right)^P \exp(\beta E) \qquad (2.7)$$

where parameters p and E define the regime of condensation.

Regime	2-D islands	3-D islands
Extreme incomplete	$p = i$ $E = [E_i + (i+1)E_a - E_d]$	$p = 2i/3$ $E = 2[E_i + (i+1)E_a - E_d]/3$
Initially incomplete	$p = i/2$ $E = [E_i + i E_a]/2$	$p = 2i/5$ $E = 2[E_i + iE_a]/5$
Complete	$p = i/(i+2)$ $E = [E_i + i E_d]/(i+2)$	$p = i/(i+2.5)$ $E = [E_i + iE_d]/(i+2.5)$

Table 2.1 Parameter dependencies of the maximum cluster density in various regimes of condensation[48]

Various characteristics which define three different regimes of condensation are:

Extreme incomplete condensation:

- $n_1 \approx R\,\tau_a$ (considerable re-evaporation from the substrate)
- clusters grow upon direct incorporation of impinging molecules on the cluster surface

Complete condensation:

- no re-evaporation from the substrate
- cluster growth dominated by incorporation of diffusing molecules on the substrate

Initially incomplete condensation:

- Intermediate between complete and extreme incomplete condensation

2.2.5 CAPTURE ZONE MODEL

Most of the growth equations discussed in the previous subsection for nucleation and growth are mean field in nature because fluctuations in the environment of the islands are neglected in the theory. Capture Zone Model discusses the effects of local environment of the islands on their growth to fully understand the scaling in different growth systems. As shown in Fig. 2.7, Capture Zone of an island is represented by a Voronoi polygon constructed around an island and each island grows inside its own Voronoi polygon. Voronoi polygon is defined as a polygon whose interior consists of all points in the plane which are closer to a particular lattice point than to any other. Any atom or molecule falling inside the capture zone of an island will get absorbed into the island. This is same as saying that the islands with bigger capture zones will grow faster than the islands with smaller capture zones.[49]

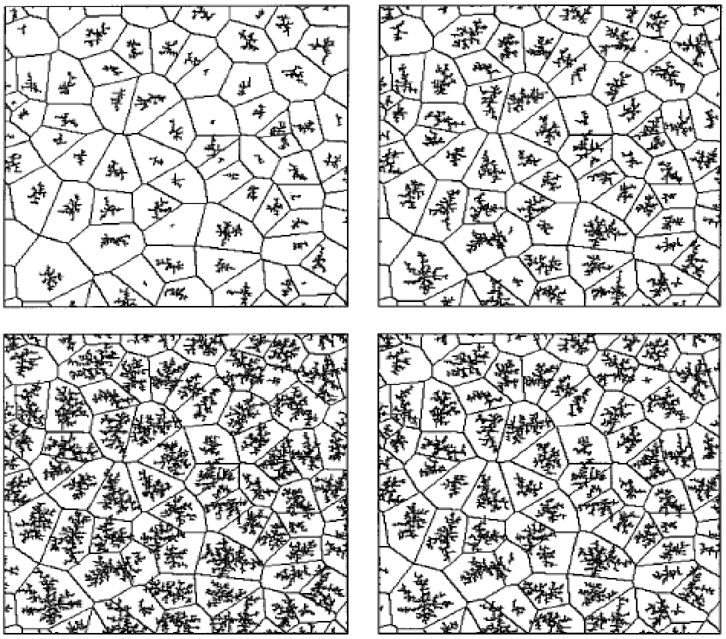

Figure 2.7 Pictures of evolving island structures in the simulation of dendritic islands. Starting from top left the coverage θ = 5%, 10%, 15% and 20% moving clockwise[49] Reprinted figure with permission from P.A. Mulheran and J.A. Blackman, *Physical Review B*, 53, 10261, 1996. Copyright 1996 by the American Physical Society. http://link.aps.org/abstract/PRB/v53/p10261

On an average, each island will absorb those molecules which will arrive in its capture zone area. At any stage of growth, an island's size is equal to the product of coverage and its capture zone area and the average island size is the product of the coverage and the average capture zone area. Consequently at any stage of growth, the island size relative to the average island size is equal to its capture zone relative to the average capture zone size in the network. This fixed ratio give rise to the island size scaling in systems where the correlated growth of neighboring islands is observed.[50]

2.2.6 Diffusion Limited Aggregation vs Reaction Limited Aggregation

Diffusion and reaction are two important microscopic processes that govern the nucleation and growth behavior. Depending on the rate limiting process, diffusion-limited and reaction-limited regimes can be defined.

Diffusion Limited Aggregation (DLA)

DLA was originally introduced by Tom Witten and Len Sander as a model for irreversible colloidal aggregation. It is one of the most widely used models for describing the irreversible fractal growth. A fractal is defined as an object or a shape that displays self-similarity at all length scales. The shape need not be same at different scales but should exhibit same "type" of structures at any length scale. A typical DLA monitored cluster morphology is shown in Fig. 2.8.

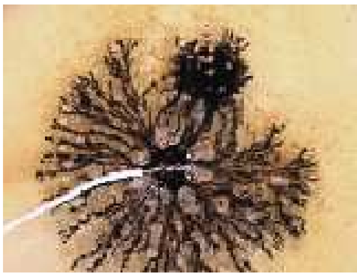

Figure 2.8 Schematic showing dendritic shape of a growing crystal[51] http://www.smart.tii.se/smart/events/events2003_se.php

The basic concept of the DLA model is the irreversible adherence of the molecules performing Brownian motion. Highly branched and fractal shapes are obtained for the growth systems following DLA. The system's fractal shape arises due to the faster growth of the branches which effectively shields the inner part, which become less accessible for the incoming molecules. A particle undergoing random walk is more probable to hit the tip of the branches and get attached, rather than penetrating into one of cluster's "fjords" without touching any surface site. The rate limiting step is the diffusion of molecules and diffusion barriers decide the growth. Many mathematical models have been developed describing DLA growth. Number of particles (n) and the size of the cluster (r) are related by the following equation:

$$n = r^D$$

where D is defined as the fractal dimension. DLA model suggests $D = 1.71$ in two dimension and $D = 2.5$ in three dimension.[52,53,54]

Reaction Limited Aggregation

Reaction limited aggregation (RLA) is other extreme of the growth kinetics, where compact clusters are formed compared to the branched structures observed in DLA regime. In this regime there is an energy barrier at the reaction site, significantly higher than the diffusion barrier, which governs the nucleation and growth.

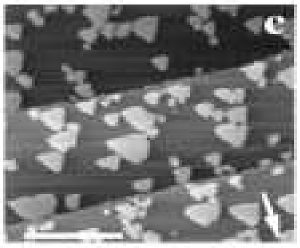

Figure 2.9 Topography showing 2D Ge islands on Pb covered Si.[55] Reprinted figure with permission from T. C. Chang, I. S. Hwang, T. T. Tsong, *Physical Review Letters*, 83, 1191, 1999. Copyright 1999 by the American Physical Society.
http://link.aps.org/abstract/PRL/v83/p1191

The reason behind this significant difference in shape of the growing islands is a difference in the sticking coefficient of molecules diffusing on the substrate to the growing islands. Sticking coefficient of molecules in RLA regime is very small compared to DLA regime (its almost 1 in DLA). In RLA regime, growth of certain planes is energetically favorable over the others. If the incorporated molecules result in the growth of less favorable plane, they will bounce off the growing surface and try to look for the site which is energetically favorable. This reorganization of molecule is responsible for the low sticking coefficient in RLA. The observed fractal dimension D for the clusters growing in RLA regime is ~ 2.1.[55, 56]

Transition from fractal to compact island morphology also occurs at high temperatures. When the edge diffusion becomes faster than the rate at which new admolecule arrives at the island, due to an increase in temperature, morphology transition takes place and growing islands become compact in shape. Lower deposition rates favor fractal shapes over the compact shapes because at lower deposition rates the concentration of admolecules on the substrate is significantly low and the admolecules can perform Brownian motion before getting absorbed by any island surface site.

2.2.7 Dislocation Assisted Growth

Dislocation, a one dimensional crystal defect, provides high energy site as it disrupts the periodic nature of the crystal around it. There are two types of dislocations: screw dislocation and edge dislocation. An extra plane or a half plane of atoms, the edge of which terminates inside the crystal is called an edge dislocation as shown in the Fig. 2.10 (a). This defect is centered on the dislocation line which is defined by the atoms at the end of extra half plane. Screw Dislocation can be thought of as being a distorted state when top upper front is being displaced to right with respect to lower part, as shown in the Fig. 2.10 (b). As the name suggests if one traces atomic planes along the dislocation line, a helix is traced in case of a screw dislocation. Most of the crystalline materials have dislocations, which have both edge and screw components, and are called mixed dislocations.[57]

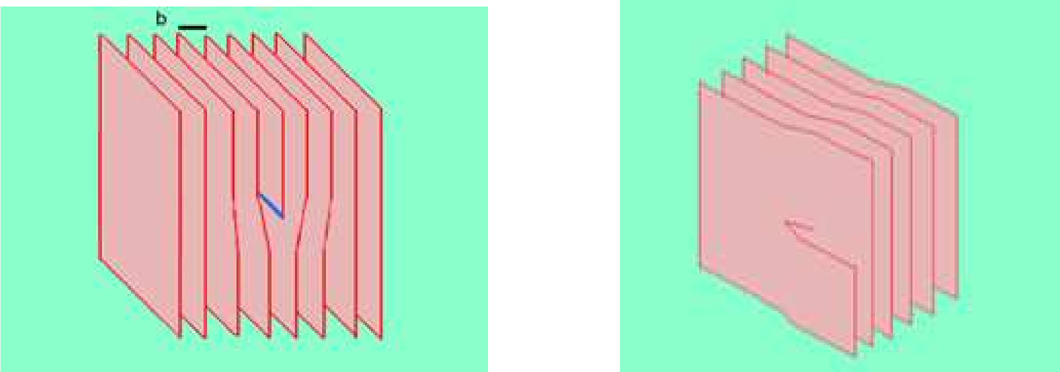

(a) (b)

Figure 2.10 Schematic showing (a) Edge dislocation and (b) Screw dislocation[58] http://en.wikipedia.org/wiki/Dislocation

Any high energy sites such as impurities, grain boundaries or dislocations, can act as potential nucleating centers. During the growth of single crystals or layer-by-layer thin film growth, these potential nucleating centers can disrupt the normal growth behavior. Spiral surface growth is the most common growth mechanism for crystals with atomically flat surfaces. Such crystals grow by incorporation of new atoms (or molecules) at the step sites. If steps are pinned at a screw dislocation, they wind around the dislocation and grow as spirals. The screw displacement is evident on the final crystal surface as a step, as shown in Fig. 2.11.

Recently screw dislocation assisted spiral growth has been also observed in thin films. Hawley et al. observed the spiral growth in sputtered films of $YBa_2Cu_3O_7$, as shown in Fig.2.12.[59] The probability of screw dislocation assisted growth increases at low super-saturations especially for compounds like $YBa_2Cu_3O_7$. Because of the layered structure, the fastest growing direction will be pointing perpendicular to the film and thus adatom is most easily added at the edge. An alternative growth mechanism, layer-by-layer growth needs nucleation of islands on top the fully coalesced, atomically flat surface which seems very improbable for a compound like $YBa_2Cu_3O_7$ because of its anisotropic and highly inhomogeneous unit cell. Springholz et al. observed the spiral growth in epitaxially grown PbTe on BaF_2 (111) surface as shown in Fig. 2.12.[60] They postulated that the 4.2% mismatch between the film and the substrate resulted in the origin of screw dislocations and hence spiral growth.

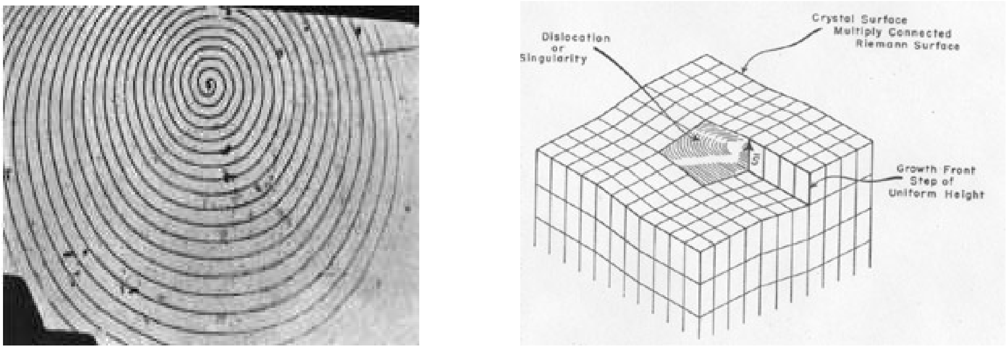

(a) (b)

Figure 2.11 (a) Spiral growth observed in carborundum, and (b) A step on a crystal face arising from a screw dislocation which gives a growth front for extension of the crystal as a Riemann surface generated by the spiral[61, 62] Reprinted by permission from Macmillan Publishers Ltd: A. R. Verma, Nature, 168,783 (1951), copyright 1951.

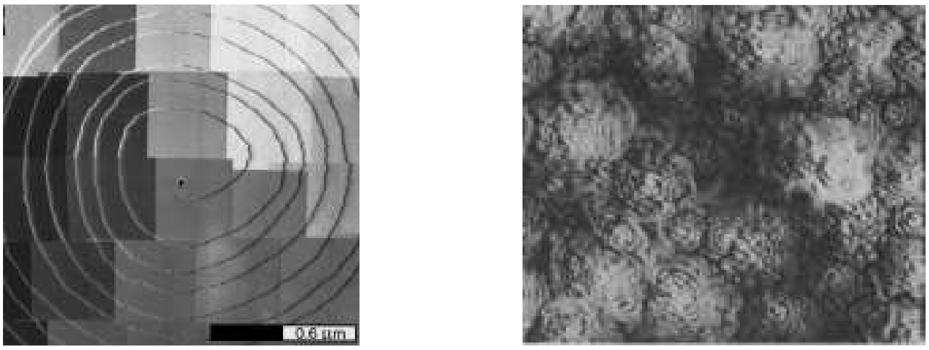

Figure 2.12 STM image of PbTe on BaF_2 and $YBa_2Cu_3O_7$ on $SrTiO_3$[59,60] From M. Hawley, I. D. Raistrick, J. G. Beery, R. J. Houlton, Science, 251, 1587 (1991). Reprinted with permission from AAAS. Reprinted with permission from G. Springholz et al., Applied Physics Letters, 69, 2821 (1996). Copyright 1996, American Institute of Physics.

2.3 Organic vs Inorganic Film Growth

In comparison to the growth of organic molecules on inorganic or organic substrates, growth of inorganic single atoms or dimers has been studied in considerable detail. In contrast to the molecular case- there is no problem related to anisotropy in inorganic film growth. Atoms are assumed to have isotropic spherical shapes such that the interaction between deposited adatom and substrate does not depend on the relative orientation of adatom with respect to the substrate.[43]

Complexity of the situation increases when the deposition of organic molecules on solid substrates is considered. Position of the particle (organic molecule) can no longer be represented by just three numbers defining its center of mass; in addition three Euler angles need to be defined describing the orientation of the molecule. This pronounced anisotropy in the organic molecules effectively introduces a new dimensionality in the study of film growth. In contrast to inorganic atoms or dimers, organic molecules are held together by relatively weak forces and the admolecule-substrate interaction depends on the relative orientation of organic molecule with respect to the substrate. Final morphology of the films is a delicate interplay between anisotropic interactions between the molecules, their neighbors and the substrate.[63] For example, pentacene on SiO_2 has its long axis oriented perpendicular to the substrate because pentacene-pentacene interactions are favored, while pentacene on Si has its long axis oriented parallel to the substrate because pentacene-Si interaction is favored.

Other dissimilarities include the existence of polymorphs in organic materials. Many organic solids do not have a unique bulk structure. In bulk, some molecules can have a different molecular packing from the rest of the molecules but with similar lattice energies. Some of the polymorphs are meta-stable and irreversibly gets transformed to thermodynamically stable phases, in other cases stable structures show reversible phase transitions. Another important point is the flexibility of the organic molecules. When brought in contact with the substrate they can distort and sometimes a part of it reacts with the substrate forming a bond, the strength of which varies over a large range of values.[63]

2.3.1 Organic Thin Films on Solid Substrates

A) Diindenoperylene (DIP)

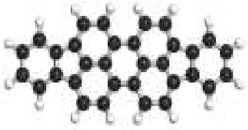

Figure 2.13 Chemical structure of diindenoperylene ($C_{32}H_{16}$)[63]

High degree of molecular ordering is observed, when DIP is deposited on atomically flat SiO_2 surface at elevated temperature of about 145°C. This molecule shows the best layer-by-layer growth among all the organic semiconductors. Fig. 2.14 shows the cross-section TEM image a of 40 nm thick film of DIP on SiO_2 with large planar terraces separated by steps with heights corresponding to 16.5 Å. The comparison of this distance with the length of the molecule (18.4 Å) suggests an upright orientation of the molecule on the substrate with a tilt of 15-20° relative to the substrate normal, as shown in the Fig. 2.14. This thin film phase is referred as σ phase.

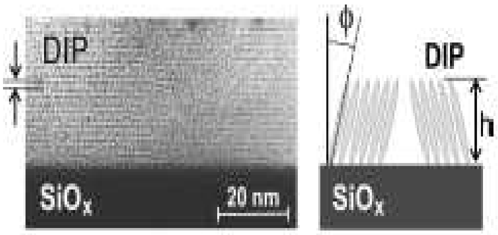

Figure 2.14 TEM micrograph of DIP film grown on SiO_2 showing a high order of molecular ordering and schematic representation of relative tilt of molecules[64] A. C. Durr, F. Schreiber, M. Kelsch, H.D. Carstanjen, and H. Dosch: Morphology and Thermal Stability of Metal Contacts on Crystalline Organic Thin Films. *Advanced Materials*. 2002. 14. 961. Copyright Wiley-VCH Verlag GmbH & Co. KGaA. Reproduced with permission.

Quantitative analysis of the films revealed a lot of roughness despite a good ordering. This roughness is attributed to different crystallographic domains (grains) within a layer, which occurs due to inhomogeneous lateral growth of the films. A different direction of tilt in these symmetry equivalent domains is the suggested reason behind the polycrystallinity. When DIP is deposited on Au, the same ordering is seen but the molecules are oriented with their molecular axis parallel to the substrate.[64, 65]

(B) Perylene-tetracarboxylicacid-dianhydride (PTCDA)

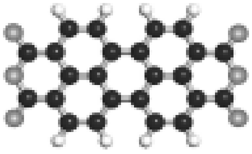

Figure 2.15 Chemical structure of PTCDA[63]

PTCDA crystallizes in a herringbone structure with each plane containing interlocking molecules as shown in the Fig. 2.16. This crystal structure is stabilized by dispersion forces and quadrupole interactions. Two monoclinic polymorphs, α and β, exist for PTCDA.

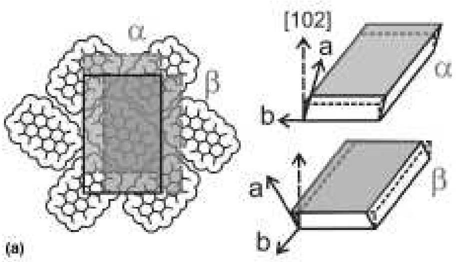

Figure 2.16 Molecular packing and structure of α and β polymorphs of PTCDA[66]

Epitaxial growth of PTCDA is observed on NaCl (100) and KCl (100) substrates for low deposition rates (~ 1.5 monolayer per minute) and for elevated substrate temperatures of above 200°C. The resulting organic thin films consist of non-connected plate like crystallites in which molecules form regular stacks with PTCDA plane (102) parallel to the substrate. Strong substrate-molecule interaction is responsible for the azimuthal orientation of the PTCDA crystallites on these substrates.[66]

2.4 PENTACENE GROWTH

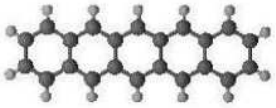

Figure 2.17 Chemical structure of pentacene

Pentacene ($C_{22}H_{14}$), a polycyclic aromatic hydrocarbon molecule consisting of five linearly-fused benzene rings, is one of the most promising organic semiconductor in the field of OTFTs due to its high hole mobility ($\mu_h \sim 1\text{cm}^2/\text{Vsec}$).[67] Because of the relative ease with which pentacene forms well-ordered crystalline films on various substrates, it is considered as a model molecule among other organic semiconductors. As discussed in Chapter 1, most of the charge transport between the source and the drain occurs in the first few layers, or perhaps the first monolayer, on top of the dielectric, making organic-semiconductor/insulator (O/I) interface critically important to the OTFT functioning.[14] Structural disorder at the (O/I) interface can hamper the OTFT performance by lowering the OTFT ON current, decreasing the switching speed and by increasing the threshold voltage. Understanding the growth mechanism of pentacene on different dielectrics and minimizing the disorder at the interface paves way for an improved device performance.

Bulk pentacene has a triclinic crystal structure (space group P1) and there are two molecules per unit cell arranged in a herringbone packing motif.[68] Bulk pentacene is reported to have two polymorphs and vacuum-deposited films are reported to have a different structure from the bulk phase which has been named “thin film phase” as shown in the Fig. 2.18. The bulk phase has been found to coexist with the “thin film phase” beyond a critical thickness (d_c). Characterization of pentacene monolayer has revealed unit cell dimensions for “thin film phase” (a = 5.916 Å, b = 7.588 Å, and γ = 89.95°), which are different from its bulk counterpart (a = 6.266 Å, b = 7.775 Å, and γ = 84.684°).[18, 69] The volume of the unit cell in the thin film phase is very identical to that of the bulk phase, indicating that the molecular packing efficiency is similar in both the phases.

Thermodynamics and kinetics of pentacene island formation on various substrates are governed by various depositing parameters such as the substrate temperature, the surface coverage and the rate of deposition (flux), as well as the chemical and crystalline nature of the substrate. The substrate material defines the diffusion pre-factor D_o and the activation energy for diffusion E_a, the substrate temperature decides the kinetic energy of the admolecules and the deposition flux decides the rate of molecules diffusing on the substrate per unit area per unit time. The following subsections discuss the importance and impact of depositing parameters on the growth of pentacene on various substrates.

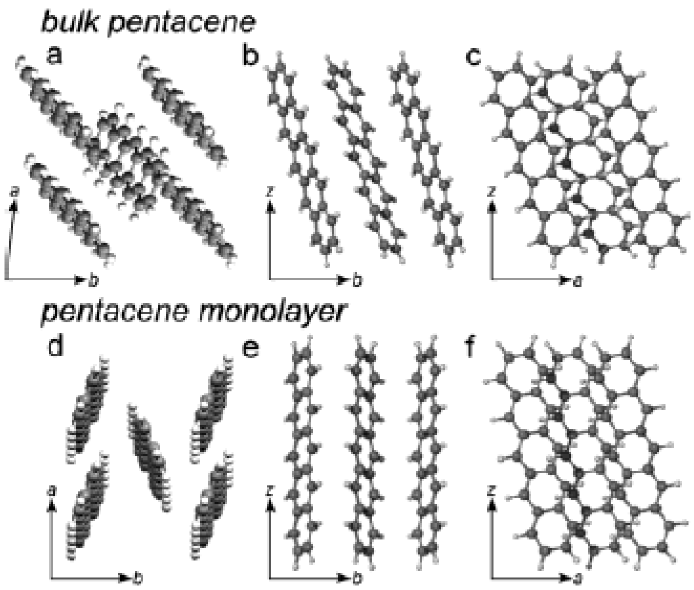

Figure 2.18 Normal and side views of the pentacene bulk phase and the thin film phase[18] Reprinted with permission from S. E. Fritz, S. M. Martin, C. D. Frisbie, M. D. Ward, M. F. Toney, *J. Am. Chem. Soc.*, 126(13) 4084 (2004). Copyright 2004 American Chemical Society.

2.4.1 DEPOSITION RATE AND SUBSTRATE TEMPERATURE

$$\frac{n_x(Z)}{N_o} \approx \left(\frac{R}{N_o \upsilon}\right)^P \exp(\beta E)$$

The above equation (same as equation 2.7 (with $\beta = 1/kT$)) relates the nucleation density to deposition rate (R) and substrate temperature (T). Nucleation density varies as a power law with the deposition flux and as an activated Arrhenius law with the substrate temperature such that higher temperature and low depositing flux result in low nucleation density and larger average grain size. Morphology dependence on the substrate temperature and the depositing flux are shown in Fig. 2.19. As seen in the figure, keeping constant substrate temperature and increasing the deposition flux increases the nucleation density of pentacene islands on SiO_2, and increasing the substrate temperature for fixed deposition flux results in a decrease in nucleation density.

Pratontep et al. observed that the islands shown in the Fig. 2.19 are 1.5 ± 0.1 nm in height above the SiO_2 substrate, which is approximately same as the length of the long axis of the pentacene molecule, suggesting that the molecules are standing upright on top of the substrate with a very little tilt. They observed that the nucleation density changes by two orders of magnitude when the deposition rate is changed by the same order, while even a small change in the substrate temperature (29 ^{o}C to 80 ^{o}C) changes the nucleation density by few orders of magnitude.[70] This result completely validates the use of basic rate equations described in section 2.2.4, where the nucleation density varies (i) as a power law with deposition rate and (ii) as an activated Arrhenius law with the substrate temperature.

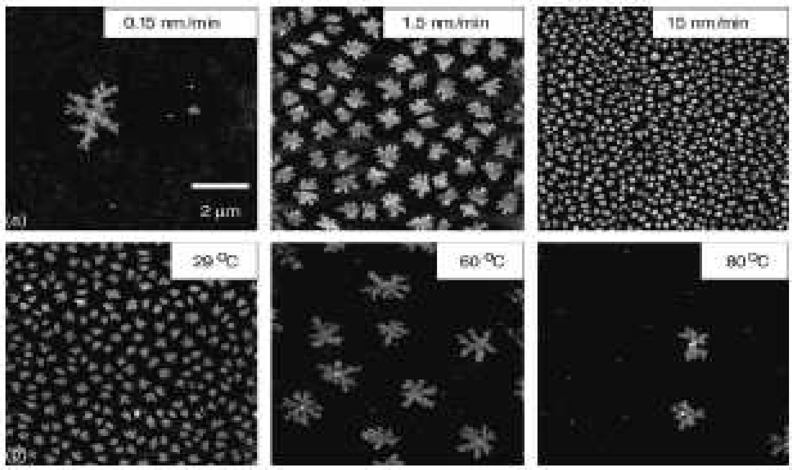

Figure 2.19 AFM topography images of 10 X 10 μm^2 size of 0.5 nm thick pentacene films on SiO_2.(a) for various deposition rates at same substrate temperature of 65^{o}C. (b) for different substrate temperatures at fixed deposition rate of 0.45nm/min[70]

Another important feature in the AFM images shown in Fig. 2.19 is the uniform distribution of the pentacene islands on the SiO_2 substrate, especially for the deposition rates above 1.5 nm/min. The narrow size distribution of the growing islands indicates that there is no secondary nucleation during the growth of existing islands. This observation underlines the existence of extended depletion zones around the growing nuclei which prevents secondary nucleation. The compactness of the growing islands increases with increasing deposition rate. The compactness of an island is defined by a form factor (f) which is given by $(f) = 4\pi\langle A\rangle/\langle P\rangle^2$, where <A> and <P> are the mean area and the mean perimeter of an island respectively. At very low deposition rates, dendritic islands are observed with very low value of f ($f = 0.2$), which tends to increase to 0.65 at higher rates more than 10 nm/min.[71] Dendritic shape at low deposition rates is indicative of the diffusion limited aggregation (DLA).[22] Ideally, the value of f is zero for fractal growth and is one for the circular island growth. Variation of coverage, island density, island size and form factor with deposition rate is shown in Fig. 2.20.

Increasing the substrate temperature helps in growing larger grains but it also decreases the value of d_c (thickness beyond which phase changes for a thin film), which puts an upper limit for the substrate temperature when looking for a single phase film.[72] Reported values of d_c for pentacene growth on SiO_2 are around 100-150 nm for films grown at room temperature and it goes down to 30 nm for films grown at ~ 90°C.[72, 73, 74] Deposition flux is reported to have negligible effect on the value of d_c. Diffusion of molecules on the surface depends on the substrate temperature. Too low a temperature can freeze the admolecules, resulting in high nucleation densities and finally leading to an amorphous film. This sets a lower bound for the substrate temperature. Flash evaporation also leads to an amorphous film revealing that even high deposition rates can lead to loss in crystallinity of films.[75,76]

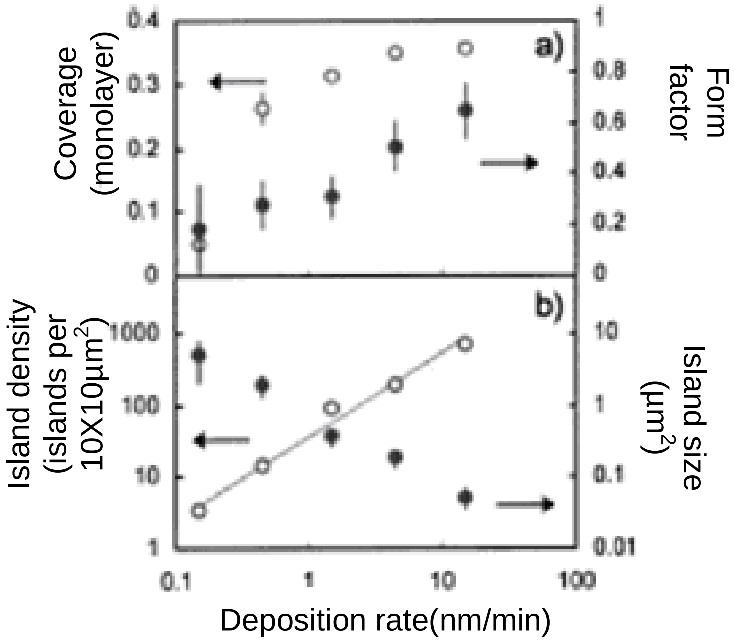

Figure 2.20 Morphology dependence of 0.5nm thick pentacene grown on SiO_2. (a) Coverage and form variation with deposition rate. (b) island density and size variation with deposition rate[71] Reprinted figure with permission from S. Pratontep and M. Brinkmann, *Physical Review B*, 69, 165201, 2004. Copyright 2004 by the American Physical Society. http://link.aps.org/abstract/PRB/v69/e165201

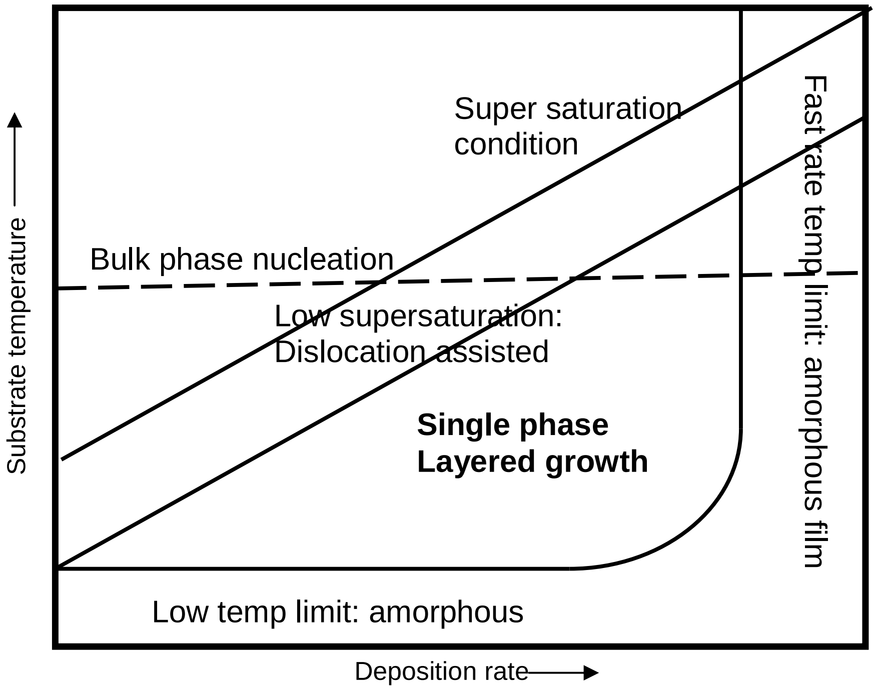

Figure 2.21 Dominating growth mechanisms at different sets of substrate temperature and deposition rate. A crystal can be grown below the line of super-saturation condition. Low temperature and high flux results in an amorphous film. Low super-saturation can lead to defect assisted growth. The upper limit of the temperature is being set by the bulk phase nucleation line[75] Reprinted with permission from R. Ruiz et al., *Chem. Mater.*, 16, 4497 (2004). Copyright 2004 American Chemical Society.

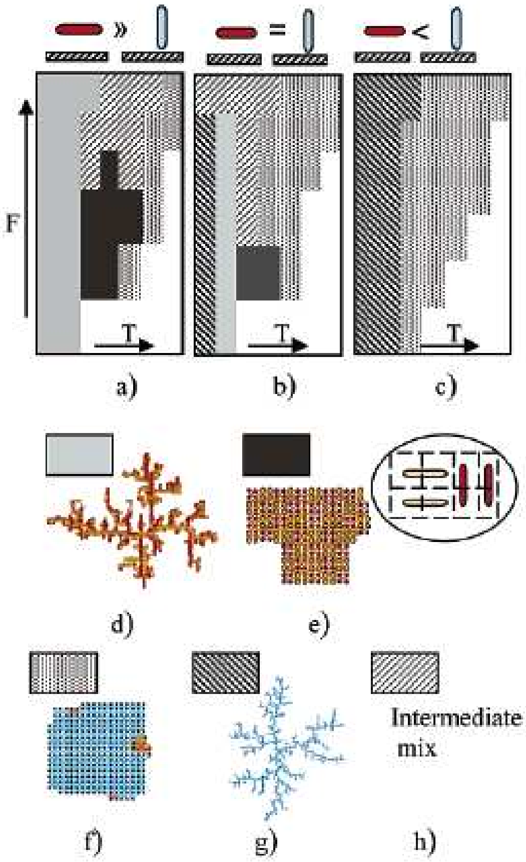

Figure 2.22 Different morphologies of the pentacene molecule on different substrates as a function of the deposition rate (F) and the substrate temperature (T), derived using Kinetic Monte Carlo simulations. (a) molecule-substrate interaction favor parallel orientation, (b) molecule-substrate and molecule-molecule interactions are comparable and (c) molecule-molecule interaction favors upright orientation than parallel orientation. Color coded representations of different morphologies: (d) Gray-all molecules lie parallel to the substrate with dendritic structure, (e) Black-all molecules lie parallel to the substrate with compact arrangement, (f) Light gray dots-majority of the molecules are in a perpendicular orientation and compact arrangement, (g) Dark grey diagonal lines-majority of the molecules lie in perpendicular orientation with dendritic arrangement, and (h) Light grey diagonal line-transitional structures, not belonging to any group[76,77] D. Choudhary, P. Clancy, R. Shetty, F. Escobedo. Advanced Functional Materials. 2006. 16. 1768. Copyright Wiley-VCH Verlag GmbH & Co. KGaA. Reproduced with permission.

Fig. 2.21 summarizes different limitations imposed on the substrate temperature and the deposition flux in order to get a single phase layered growth. Lower super-saturation at lower deposition rate and higher substrate temperature can give rise to a defect assisted growth. In layer-by-layer growth mode, new nucleating sites have to be formed every time a layer is fully grown. The energy barrier for this nucleation is considerably high, so at low supersaturations the growth can predominantly occur at existing surface steps associated with screw dislocations.

Although lower deposition rates and higher temperatures are needed to grow large grains, care should be taken because lowering the deposition rate beyond a point or increasing the temperature above a certain limit can lead to other growth mechanisms such as bulk phase growth or defect assisted growth, which can dampen the 2-D growth of the islands.[74] Fig. 2.22 shows the morphologies of pentacene monolayer on different substrates as a function of the deposition rate (F) and the substrate temperature (T), obtained from Kinetic Monte Carlo simulations.[77]

2.4.2 SUBSTRATE

Nature of the substrate defines the orientation of the pentacene molecule with respect to the substrate and has a major impact on the growth mechanism of first monolayer. When pentacene is deposited on inert-flat substrates such as oxides and polymeric substrates, the molecules tend to orient with their long molecular axis perpendicular to the substrate exposing (001) plane, which is the lowest energy plane in pentacene. Strong interaction within the pentacene molecules compared to pentacene-substrate interaction forces pentacene molecules to stand vertically on the substrate such that (001) plane is parallel to the substrate. In the case of high energetic surfaces like metals and Si, the strong pentacene-substrate interaction forces pentacene molecules to lie flat on the substrates such that (001) plane is perpendicular to the substrate. In the latter case some charge transfer also takes place at the interface.

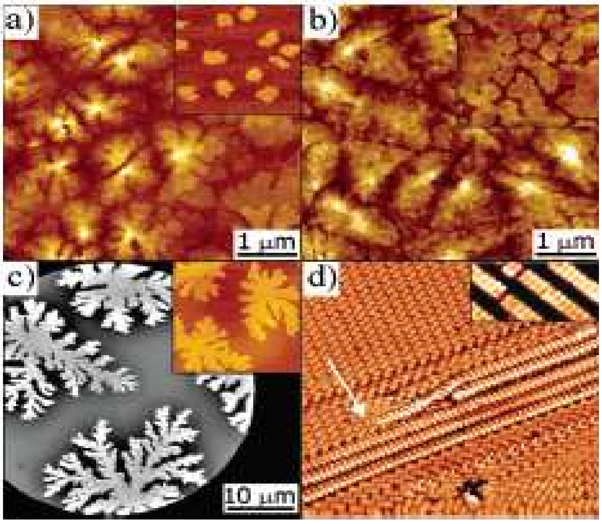

Figure 2.23 Pentacene morphology on various substrates. (a) Three monolayer thick pentacene films on SiO_2.Inset: First monolayer islands of pentacene on SiO_2.[75] (b) Pentacene on PEDOT: PSS. Inset: First monolayer islands of pentacene on PMMA.[75] (c) Submonolayer islands of pentacene on Si (after a layer of pentacene lying flat on the substrate. Inset: pentacene islands on H-terminated Si.[22] (d) STM image of pentacene molecules on Ag. Inset: STM image of pentacene on Cu showing molecules lying flat on the substrate[78] Reprinted with permission from R. Ruiz et al., *Chem. Mater.*, 16, 4497 (2004). Copyright 2004 American Chemical Society. Reprinted figure with permission from S. Lukas et al., *Physical Review Letters*, 88, 028301, 2002. Copyright 2002 by the American Physical Society. http://link.aps.org/abstract/PRL/v88/e028301 Reprinted with permission from Macmillan Publishers Ltd: Nature, Heringdorf et al., 412, 517, 2001, copyright 2001

Morphology of pentacene thin films has been studied on various substrates which include oxides and nitrides such as SiO_2, Al_2O_3 and SiN, polymeric materials like

PMMA, PEDOT/PSS and PVP, and some high-k dielectrics such as BZT, BST and $BaTiO_3$. The first monolayer morphologies of pentacene on various kinds of substrates are shown in Fig. 2.23.

Considering the importance of the first monolayer on top of the dielectric, the early stages of the film formation demands a detailed study. Nucleation and subsequent growth dependence on substrates can be studied by either changing the substrate or by changing the surface termination. Sirapat et al. compared the nucleation and growth of pentacene islands in the submonolayer regime onto organic substrates of poly(methyl-metacrylate) (PMMA) and inorganic substrates of SiO_2 and Al_2O_3.[26] They found that at similar substrate temperature and deposition rate, nucleation density changes with the substrate type, as shown in Fig. 2.24.

At very low deposition rates, Al_2O_3 and SiO_2 substrates result in dendritic pentacene islands which is a characteristic of an irreversible “hit and stick” picture of the diffusion-limited aggregation model. But at high deposition rates the shape of the islands becomes compact. In case of PMMA substrate, the islands are always found to be compact in shape at all deposition rates. As clearly seen in Fig. 2.25, at same substrate temperature and deposition rate, the nucleation density on PMMA is an order of magnitude higher than on Al_2O_3 and SiO_2.

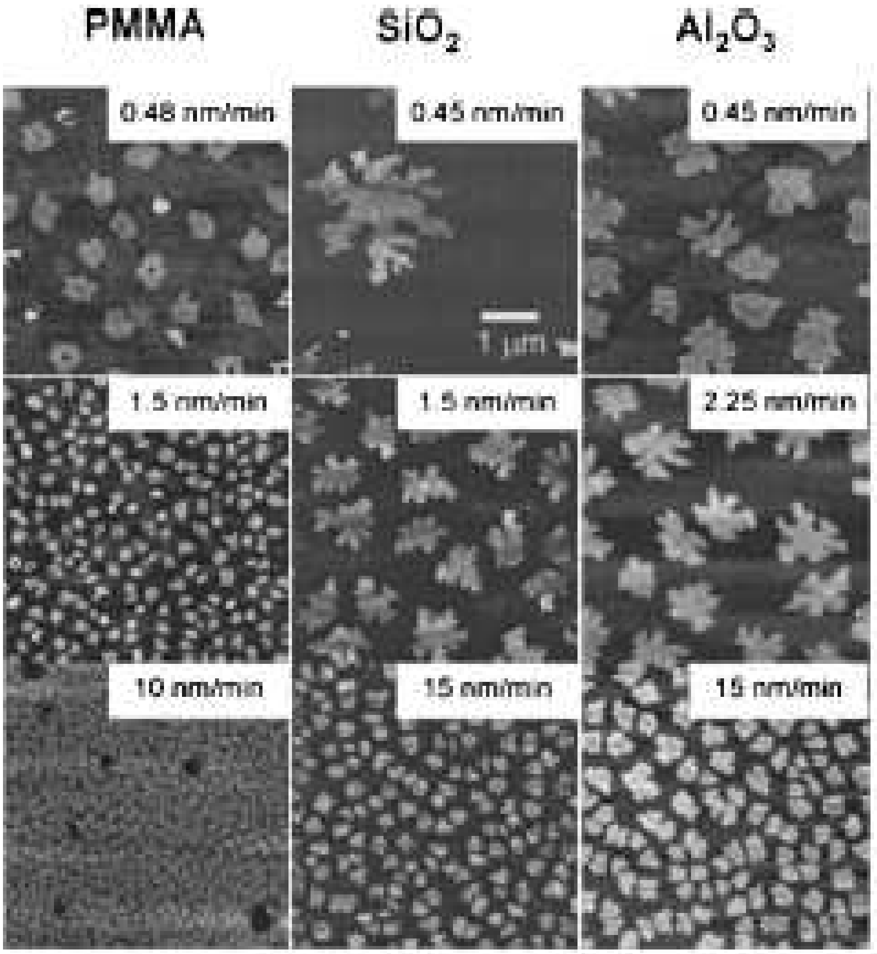

Figure 2.24 Effect of substrate on the nucleation density of pentacene islands. All the images are 10 X 10 µm^2. Substrate temperature = 65 ^{o}C and the nominal thickness of pentacene films = 0.5 nm[26] Reprinted figure with permission from S. Pratontep et al., *Physical Review B*, 72, 085211, 2005. Copyright 2005 by the American Physical Society. http://link.aps.org/abstract/PRB/v72/e085211

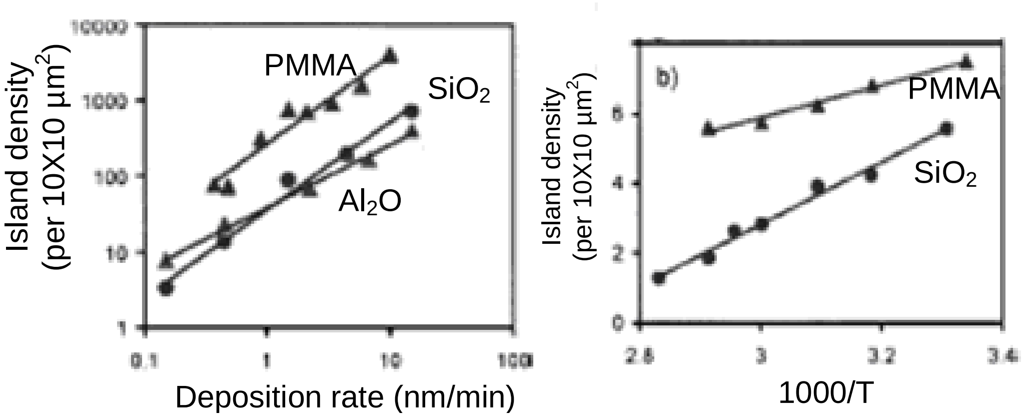

Figure 2.25 Nucleation density dependence on deposition rate and temperature for different substrates (PMMA, SiO_2 and Al_2O_3)[26] Reprinted figure with permission from S. Pratontep et al., *Physical Review B*, 72, 085211, 2005. Copyright 2005 by the American Physical Society. http://link.aps.org/abstract/PRB/v72/e085211

Figure 2.25 shows the nucleation density dependence on the substrate temperature and the deposition rate. Deposition rate plot clearly indicates that the nucleation density in all the cases can be described by a scaling law, N = const. $(R)^{\delta}$. The exponent δ for different substrates has been listed in Table. 2.2. Temperature plot shows the Arrhenius behavior for both, PMMA and SiO_2 at fixed deposition rate, which justifies Venable's rate equations N = const. $(R)^{\delta}\exp(E_{Nucl}/kT)$, where N is the nucleation density.

Substrate	SiO_2	Al_2O_3	PMMA
Exponent δ	1.16	0.8	1.18
E_{Nucl} (eV)	0.4-0.5	-	<0.1

Table 2.2 Experimental data for nucleation of pentacene on various substrates[26]

Comparison of the nucleation density of pentacene islands on reduced and oxidized surfaces is done in Fig. 2.27. For the reduced surface the nucleation density is 0.007 μm^{-2}, while for an oxidized surface it is 100 times larger (around 0.7 μm^{-2}). In case of reduced surface, second monolayer islands start nucleating at coverage of 0.6 monolayer and first layer completely coalesce at a coverage of 2 monolayer, while the corresponding numbers for an oxidized surface are 0.6 monolayer and 1.1 monolayer respectively (Fig. 2.28).[19]

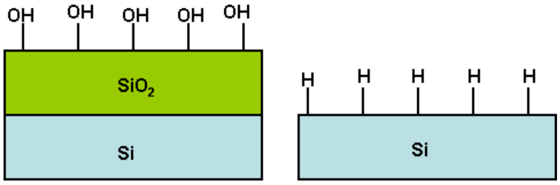

Figure 2.26 O/OH terminated silicon dioxide and H atom terminated Si[19]

Conventional cleaning processes leave SiO_2 surface quite hydrophilic. The hydrophilic surfaces adsorb water and this can result in a film of water on the substrate which can change the growth mechanism of pentacene. To avoid this, SiO_2 is generally treated with SAMs because it changes the wetting properties of SiO_2 by making it hydrophobic in nature. Generally surface roughness of SiO_2 increases on treating with SAMs, which leads to more nucleation density but the dislocation density goes down significantly (discussed in the following subsection).[19]

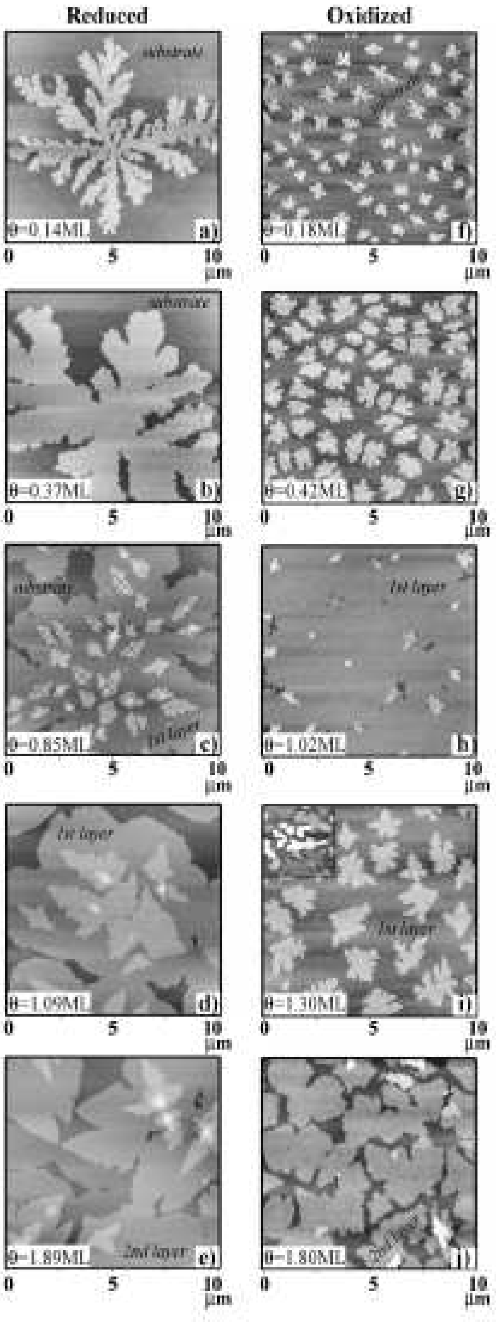

Figure 2.27 AFM images of pentacene films on oxidized and reduced substrates, at various coverages[19] Reprinted figure with permission from R. Ruiz et al., *Physical Review B,* 67, 125406, 2003. Copyright 2003 by the American Physical Society. http://link.aps.org/abstract/PRB/v67/p125406

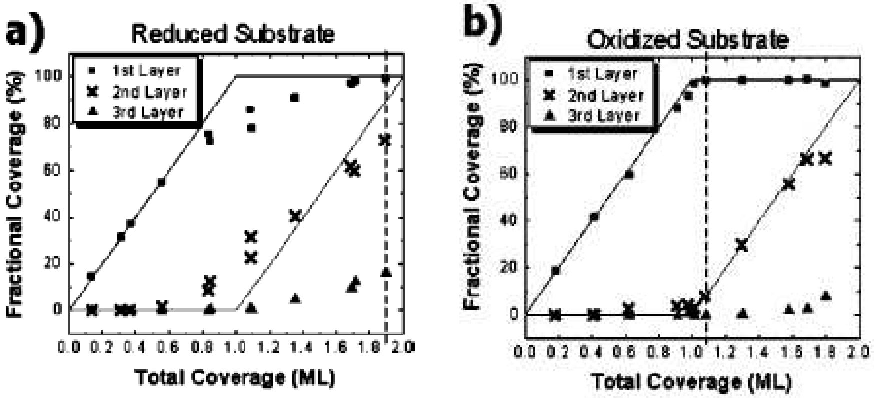

Figure 2.28 Fractional coverage as a function of total coverage for (a) a reduced substrate and (b) an oxidized substrate[19] Reprinted figure with permission from R. Ruiz et al., *Physical Review B,* 67, 125406, 2003. Copyright 2003 by the American Physical Society. http://link.aps.org/abstract/PRB/v67/p125406

2.4.3 Dislocations in Pentacene

Dislocations can play an important role in the growth of thin films, as discussed in subsection 2.2.7. Recently evidence of dislocations in pentacene thin films has been reported by two groups. Nickel et al. used synchrotron x-ray diffraction to detect screw and edge dislocations in 2-8 monolayer thick pentacene films grown on modified silicon surfaces, while Kanan et al. used Friction Force Microscopy (a variant of AFM) to image line dislocations in 2-3 monolayer thick pentacene films grown on SiO_2.[30,79]

Pentacene thin films have very weak inter-layer interaction and strong intra-layer lateral interaction. This particular anisotropy in the interaction favors distortion along the surface normal. Consequently most of the defects are screw dislocations with Burger's vector along the long axis of the pentacene molecules. Screw dislocations are surrounded by the prismatic loops which are formed by the ends of the edge dislocations.

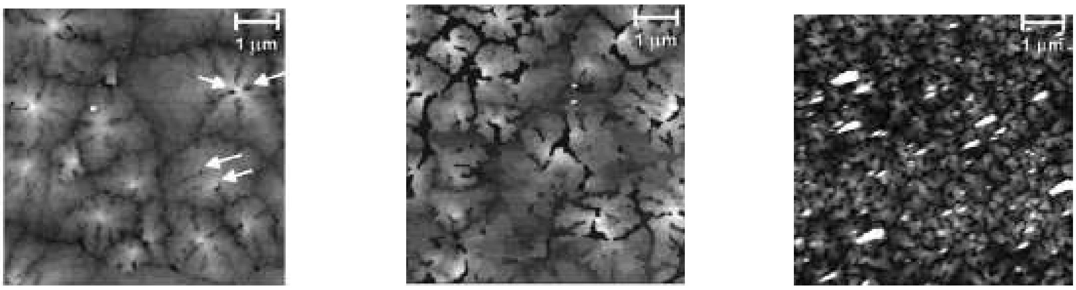

(a) (b) (c)

Figure 2.29 Tapping mode AFM images of 8 monolayer thick pentacene films on (a) H terminated Si (b) re-oxidized Si and (c) OTS treated Si[79] Reprinted figure with permission from B. Nickel et al., *Physical Review B,* 70, 125401, 2004. Copyright 2004 by the American Physical Society. http://link.aps.org/abstract/PRB/v70/p125401

Nickel et al. used Bragg's diffraction to show that the number of straight dislocations per unit area (n) in pentacene thin films is different for different substrates. The value of n is 2.1 x 10^{11}cm^{-2} for a H terminated Si, 0.9 x 10^{11}cm^{-2} for a re-oxidized Si and 0.5 x 10^{11}cm^{-2} for an OTS treated Si. As seen from the AFM images shown in Fig. 2.29, the apparent grain size is largest on H terminated substrate while it is smallest on an OTS treated substrate. Some black holes can be seen in the first two AFM images at the top centers of the dendritic grains which are proposed to be screw dislocation cores. The dislocation core density is low on re-oxidized Si compared to H terminated Si and is absent on OTS treated Si. This direct correlation between the diffraction studies and the AFM results prove that the dislocation density is lower in case of an OTS treated substrates and this can be a potential reason behind the higher mobilities obtained in OTFTs based on OTS treated substrates.[79]

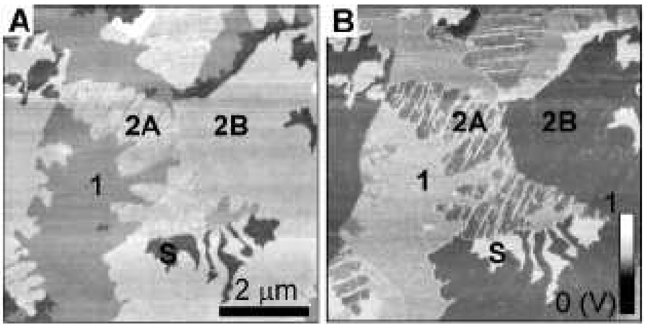

Figure 2.30 Chemically etched surface showing parallel line dislocations in 2 monolayer thick pentacene film. AFM (a) topography and (b) friction image[30] K. Puntambekar, J. Dong, G. Haugstad, C. D. Frisbie, *Adv. Funct. Mater.*, 2006, 16, 879. Copyright Wiley-VCH Verlag GmbH & Co. KGaA. Reproduced with permission.

Kanan et al. did chemical etching and subsequent AFM studies on two monolayer thick pentacene thin films on SiO_2. They observed parallel line dislocations in high friction regions of second monolayer (Fig. 2.30). Oriental mismatch or absence of epitaxy between the first monolayer and the second monolayer is suggested to be the main reason behind the existence of parallel line dislocations in the second monolayer. The regions with dislocations have more structural disorder which results in high friction contrast and this justifies the observation of parallel line dislocations in high friction regions of second monolayer of pentacene on SiO_2.[30]

Chapter 3

FRICTION

3.1 General Introduction

Friction is a force that opposes relative motion or tendency towards such a motion between two surfaces in contact. It is defined such that it always acts in a direction opposite to the direction of relative motion and thereby opposes the relative motion. Friction is not a fundamental force; its origin is the electromagnetic interaction between the atoms.[80] Magnitude of the frictional force is given by the classical Amonton’s law:

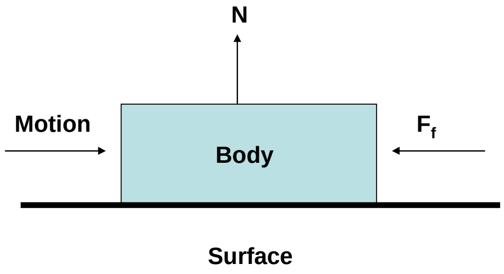

$$F_f = \mu N$$

Figure 3.1 Free body diagram showing frictional force

Where F_f = frictional force or the maximum possible magnitude of this force

μ = coefficient of friction

N = normal force between the surfaces in contact

Friction is usually classified as being either a static friction (the frictional force opposing a body at rest to move) or a kinetic friction (the frictional force tending to slow down a body in motion). In static friction, two bodies are not in relative motion and the frictional force only balances the resultant force which could have moved the body. The magnitude of static frictional force can be anywhere between 0 and F_f and acts in a direction opposite to the direction of motion that the body would have undergone without friction. In kinetic friction, two bodies are in relative motion and the friction at each surface acts in a direction opposite to its relative motion with respect to the other surface.[80]

The coefficient of friction is a scalar constant, which is given by the ratio of the friction force acting between the two bodies (F_f) and the force (both extrinsic and intrinsic) pushing the two bodies together (N). The static friction and the kinetic friction have different coefficients of friction given by μ_s and μ_k, respectively. Generally, coefficient of static friction (μ_s) is higher than the kinetic coefficient of friction (μ_k), as shown in Table. 3.1.

Material 1	Material 2	μ_s	μ_k
Cast Iron	Cast Iron	1.1	0.15
Cast Iron	Copper	1.05	0.29
Glass	Glass	0.9-1.0	0.4

Table 3.1 Coefficients of static and kinetic friction for different systems [81]
www.engineershandbook.com/Tables/frictioncoefficients.htm

3.2 Friction: Measurement Techniques

The Surface Force Apparatus (SFA) and Friction Force Microscopy (FFM) are the two techniques which can explore and elucidate the physical mechanisms occurring at the molecular level caused due to the relative sliding of the two bodies. Both the techniques are capable of measuring nano- and microscopic tribology. In FFM, a nanometer-radius tip is in relative motion with respect to a sample surface. In SFA, two bodies which are in relative motion are two extended atomically smooth surfaces that confine between them a lubricant film of known thickness and contact area.

3.2.1 Surface Force Apparatus (SFA)

The SFA consists of two crossed cylinders that can be pressed together to form a circular contact under pressure. A pair of atomically smooth mica surfaces are mounted on both the cylinders. Both the mica surfaces can be treated to attach the molecules of interest. Actuators are attached to both the surfaces to apply the load or the shear force and to control the distance between the two surfaces. Optical or capacitive methods are used to measure the contact area and the relative separation of the two surfaces. Sensors are also attached to the two surfaces to measure load and friction forces. The whole apparatus can be either completely immersed in a liquid or maintained in a controlled environment. The apparatus provides a model contact where contact geometry is known, materials between surfaces can be varied and interaction forces can be measured and controlled. The main drawbacks of the SFA are relatively low lateral resolution (~ few microns), substrate restriction to mica (requirement of molecular smoothness) and difficulty in operating at ultra high vacuum.[82, 83]

3.2.2 Friction Force Microscopy (FFM)

Atomic force microscopy (AFM), also referred to as Scanning Probe Microscopy (SPM), is a high-resolution surface characterization technique that can resolve features as small as an atomic lattice in the real space. The working mechanism of AFM is described in Fig. 3.2. In an AFM experiment, a very sharp tip (radius of few tens of nanometers) is attached to one end of a compliant cantilever. The sharp tip comes in close proximity with the sample surface and the resulting interaction between the tip and the sample surface deflects the cantilever.

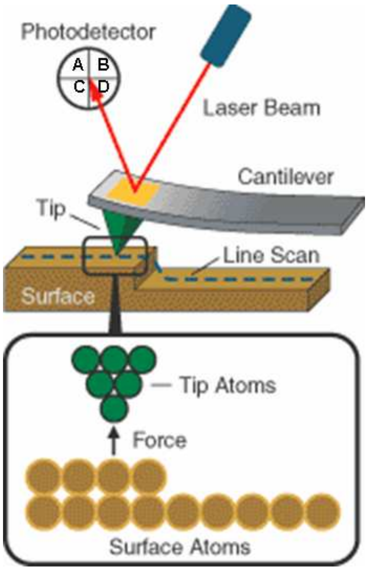

Figure 3.2 Atomic Force Microscope[84]
http://www.molec.com/what_is_afm.html

The cantilever bends vertically in response to the normal forces acting on the tip and twist laterally in response to the lateral forces acting on the tip. Deflection of the cantilever from its equilibrium position is directly proportional to the interaction force. Magnitude of the normal force and the lateral force can be calculated using the normal spring constant and the torsional spring constant of the cantilever, respectively. The vertical deflection and lateral twist of the cantilever can be measured independently and simultaneously using a quadrant photodetector in an optical beam deflection scheme.[85] The laser beam falls on the back of the cantilever and gets reflected into the quadrant photodetector, as shown in Fig. 3.2. The photodetector contains four individual photodiodes in a square array. The current difference between the upper and the lower photodiodes ((A+B)-(C+D)) is proportional to the vertical deflection of the cantilever, while the current difference between the right and the left diodes ((A+C)-(B+D)) is proportional to the lateral twist of the cantilever. The optical scheme measures the angle of inclination by which the cantilever is deflected by the vertical force (both applied and due to tip-sample interaction), which for small angles can be considered to vary linearly with the tip deflection. Contact mode AFM works on a constant deflection mode, *i.e.*, the vertical deflection of the cantilever is kept constant by the vertical movement of the piezo scanner on which the sample is mounted.

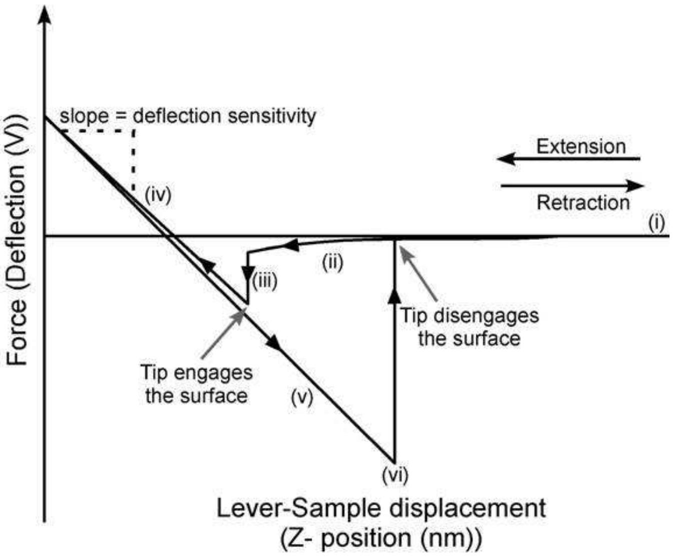

Figure 3.3 Force Curve[86] Reproduced from K. Puntambekar, PhD thesis, University of Minnesota, 2006.

Figure 3.3 is a plot of the deflection of the cantilever versus the tip-sample displacement, which shows the cantilever response when it approaches the sample surface. Arrows in the diagram show the direction of movement of the cantilever with respect to the sample surface. Different regions have been defined for various tip-sample displacements highlighting dominating interaction forces between the tip and the sample surface.

Region (i) = No forces act between the tip and the sample as they are very far apart.

Region (ii) = Attractive forces start pulling the cantilever downwards towards the surface as the cantilever approaches the sample surface. The negative slope of the curve shows the attractive nature of the interaction force.

Region (iii) = The tip snaps into contact with the sample due to the capillary force that pulls the tip down.

Region (iv) = The tip is in contact with the sample surface and the front end of the lever is pushed upward due to the externally applied load. The positive slope of the curve shows the repulsive nature of the interaction force.

Region (v) = The motion is reversed. Adhesion between the tip and the sample surface maintains the contact, although there is a negative tensile load.

Region (vi) = Finally the tip snaps out of contact with the sample as the negative tensile load exceeds the adhesion force.

Force curves can be used to apply desired normal load on the sample surface. It also gives information about the deflection sensitivity of the cantilever (given by the stiffness of the cantilever which is determined by calculating the slope of the curve when the cantilever is deflecting in the repulsive regime on a rigid sample). Pull-on force and pull-off forces which are measures of the tip-sample adhesion correspond to the magnitude of negative deflection of force in region (iii) and region (vi), respectively.

FFM, an auxiliary measurement in contact mode AFM, measures the lateral frictional forces which act on a tip, when a tip moves on the sample surface. This contact mode technique can probe nanoscale local variations in the sliding friction between the tip and the sample in conjunction with topography, enabling a direct correlation between the two.[87] The normal deflection of the cantilever (along the z axis) is caused by the normal forces acting between the tip and the sample surface, while in the friction regime the cantilever undergoes a torsional twist about its long axis (in the x-y plane) due to the lateral friction force, as shown in Fig. 3.4. To the first approximation both the motions are orthogonal to each other and therefore simultaneous and yet independent acquisition of topographic and friction images are possible.

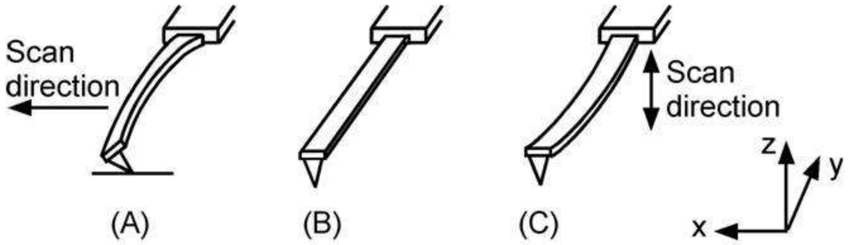

Figure 3.4 Cantilever response to the frictional and the normal forces[83]

In FFM, the fast scanning direction is perpendicular to the long axis of the cantilever such that the lateral friction force which opposes the motion of the tip on the sample exerts a torque about the cantilever's axis and causes twisting of the cantilever.

The sense of twisting changes when the scan direction of the tip changes, *i.e.*, when the relative motion of a tip with respect to a sample is from right to left, the frictional force will twist the cantilever towards left and when the relative motion of a tip with respect to a sample is from left to right, the frictional force will twist the cantilever towards right. The twisting dependence on the scan direction gives rise to a friction loop as shown in Fig. 3.5. The height (*i.e.*, magnitude) of the friction loop is a measure of magnitude of the sliding frictional force. Height of the loop is directly proportional to the dissipative energy which indicates the magnitude of sliding lateral frictional force. The height of the loop is halved to quantify the torsional signal during a single pass in one direction.

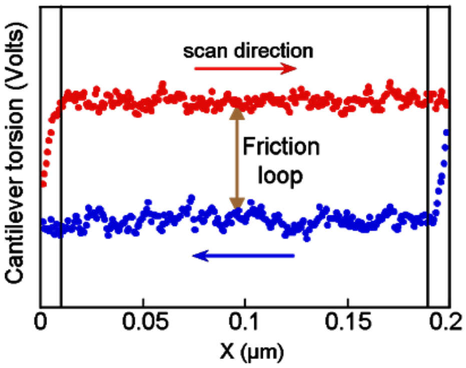

Figure 3.5 Friction loop (~ courtesy Dr. G. Haugstad, University of Minnesota)

While scanning molecular rough surfaces there is a contribution to the lateral forces from not only the friction, which resists tangential motion, but also from the local surface slope perpendicular to the tangential motion.[88] In most of the cases the topographic contribution can be quantified and removed to a first approximation by subtracting the trace and the retrace scans, provided the X-hysteresis is compensated. The remaining data reflects the energy dissipative part (true friction), which by definition resists motion.[89] The lateral friction forces depend on the interaction between the tip surface and the sample surface, so even the regions with the same topography can show friction contrast.[90] Any variation in the chemical[91], structural[92] or molecular orientation[93] on the sample surface can significantly change the frictional contrast in the FFM (discussed below).

3.3 Friction: An Atomic View

Friction, on an atomic level, originates from the interaction between the atoms. Atomically it can be viewed of as a force that opposes shearing of weak bonds between the atoms. A well defined continuous interface between two materials is an ideal concept. In most of the macroscopic cases, the interface is discontinuous and leads to a multiple asperity contact between the materials in contact. Macroscopic friction can be viewed as a collective action of small multiple asperities, which in turn depends on the normal forces acting between the two bodies. The following subsections review friction results obtained from FFM in order to understand the friction at the fundamental level. The first subsection discusses the atomic-scale stick-slip behavior which is commonly found in most crystalline films on solid substrates. The chemical and structural sensitivity of the friction is discussed in brief in the second and third subsection respectively, and the final subsection describes the anisotropic behavior of the friction.

3.3.1 Atomic-Scale Stick-Slip Behavior

Mate et al. first observed that the lateral forces experienced by a tungsten tip on graphite exhibit atomic-scale stick-slip behavior reflecting the periodicity of the lattice.[94] The underlying principle behind this behavior is the friction dependence on relative tip-sample velocity. Specifically, the friction during sliding is lower than the friction while not sliding. If a parallel force is applied to an interface, then sliding does not occur until the applied stress exceeds the static friction. Once the applied stress exceeds the static friction, the body starts sliding and the friction goes down. This leads to an increasingly faster relaxation of the applied stress until it is no longer large enough to maintain sliding. At this point the system gets stuck again and this cycle repeats itself. This phenomenon is termed as atomic-scale stick-slip behavior and occurs as a result of stick-slip behavior of the lateral forces experienced by the tip on the sample surface. A lot of factors decide atomic-scale stick-slip behavior, such as the viscoelastic properties of two materials in contact, tip-sample interaction, interface roughness and any strengthening mechanism that results during sliding.

Several theoretical efforts have been made in the past to explain the atomic-scale stick-slip behavior in context of FFM.[95,96,97] Most of the theories are semi-classical in nature and describes the mechanics of stick-slip behavior. A lot of them use the Tomlinson model as a starting point, which considers the tip to be a single asperity contact without internal degrees of freedom and considers a periodic interaction potential between the tip and the sample.[98] Further, these theories also assume that as scanning velocities are much less than the sound velocities in the materials the system can be considered under equilibrium at each step of simulation.

The initial position of the tip is defined as a position of potential minimum determined by the tip-sample interaction. Static friction develops due to the tip-sample interaction that inhibits sliding of the tip. This leads to elastic energy build up in the cantilever and elastic deformation of the tip and the surface in contact. The total build up energy consists of interaction energy and elastic energy stored in the lever and the contacting materials. After reaching a critical point, relative slip starts between the tip and the sample, and the tip leaves the position of minimum potential. The lever and the contact quickly relax, releasing energy, and the motion is brought to a stop as the tip finds a new potential minimum, one unit cell over. Phonons, created in the tip and the sample, are responsible for carrying the energy away from the interaction region and thus act as a mode of energy dissipation.[85] Some of the basic results of the semiclassical theories describing atomic-scale stick-slip behavior are summarized as follows:

- Strong tip-sample interactions along with weak cantilever springs and compliant contacts are needed to observe atomic scale stick-slip behavior.[99,100]
- The atomic stick-slip periodicity reflects the periodicity of the lattice.
- The energy produced during the stick-slip behavior is distributed between the tip, the cantilever and the substrate, with the more compliant ones dissipating more energy.[101]

- The atomic stick-slip instability can be interpreted as a system, comprising of the tip, the cantilever and the substrate, looking for minimum energy configuration.[92]

Figure 3.6 shows the lateral force image of KF (001) cleaved and imaged in ultra high vacuum with a silicon nitride tip. The periodic nature of the lateral force image exhibits stick-slip periodicity which is same as the periodicity of the KF unit cell. The right image shows the "friction loop" from a single horizontal line of the lateral force image.[92] The arrows in the friction loop image indicate scan direction for each half of the friction loop and the shape of the friction loop indicates the atomic stick-slip periodicity. Hysteresis in the friction loop signifies energy dissipation due to tip-sample interaction.

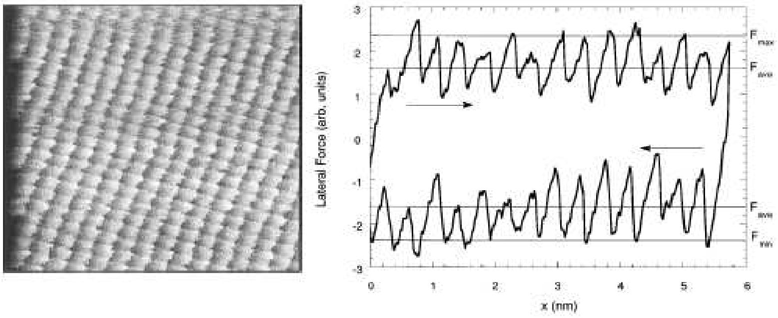

Figure 3.6 Left image shows the friction force image of KF (001) cleaved and imaged in UHV and right image shows the friction loop from a single line of the image shown in left[92] With kind permission from Springer Science + Business Media: Tribology Letters, Friction force microscopy investigations of potassium halide surfaces in ultrahigh vacuum: structure, friction and surface modification, 5, 1998, 91, R. W. Carpick, Q. Dai, D. F. Ogletree, M. Salmeron.

Riedo et al.[102] showed that the friction force on a nanometer-sized tip sliding on a surface is related to the thermally activated hopping of contact atoms on an effective atomic interaction potential. They found that the height of the potential is proportional to the normal load and the hopping attempt frequency is the lateral resonance frequency of the probing tip in contact with the surface. Filippov et al. proposed that the macroscopic frictional forces stem from the microscopic continuous formation and rupture dynamics of bonds at the interface.[103] Recent studies on force[104] and velocity[105] dependence of the atomic friction underlines the concept of stress-modified energy landscape that enhances the thermal activation of dissipative processes. Based on the above concepts and experimental results, FFM work has been looked upon as a topic of condensed matter physics or physical chemistry, instead of an old engineering concept of colliding micro-asperities.

3.3.2. Chemical Effects

The visible material contrast, as opposed to slope variations, in the friction force image comes from the difference in the cantilever twisting (*i.e.*, difference in lateral forces), when imaging a heterogeneous sample. The tip experiences different twists in different materials depending on the tip-surface interaction, thereby making lateral force microscopy chemically sensitive.

Marti et al. showed the friction force dependence on chemical nature of the sample surface. They measured the frictional forces between the silicon nitride tip and SiO_2 immersed in solution. They observed that the friction force changes when the pH of the solution changes. The extent of protonation of -OH groups on the surface of the tip and the sample depends on the pH of the solution. Consequently, different pH will result in different surface charge and different tip-sample interaction. This difference in the tip-sample interaction reflects in the friction contrast in the friction force images.[106]

Overney et al. used friction force microscopy to image hydrocarbon islands on top of fluorocarbon film. In Fig. 3.7, topography image shows bright monolayer islands of hydrocarbon on top of dark fluorocarbon film. The friction force image shows a clear contrast between the islands (hydrocarbon) and the sea (fluorocarbon film). Hydrocarbon islands exhibit lower friction (dark contrast) while the fluorocarbon film exhibits higher friction (bright contrast).[107] This chemical sensitivity of the lateral force microscopy can be exploited to distinguish different phases present on the surface of the films.

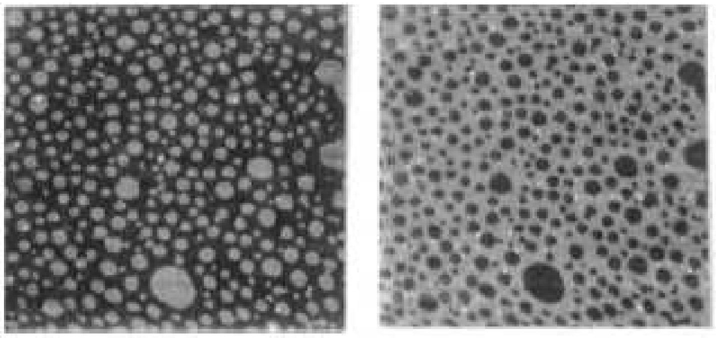

(a) (b)

Figure 3.7 Island like hydrocarbon monolayer islands on top of sea like fluorocarbon film. (a) Topography and (b) Friction force image[107] Reprinted with permission from R. M. Overney, E. Meyer, J. Frommer and H. J. Guntherodt, *Langmuir*, 10, 1281 (1994). Copyright 1994 American Chemical Society.

Chemical Force Microscopy is a technique that combines the AFM with the chemical discrimination by chemical derivatization of the scanning probe tips. Frisbie et al.[91] first used this technique to measure adhesion and friction forces between molecularly modified probe tips and organic monolayers, to map out the spatial distribution of hydrophilic and hydrophobic surface molecules. In another interesting study by McKendry et al.[108], the chemical sensitivity of chemical force microscopy was used to distinguish the surface molecules with different chiralities. Different stereoisomers interact differently with the probe tip and this gets reflected in the friction images.

3.3.3 Structural Disorder Effects

Structural disorder can also affect the frictional response of the tip when the tip scans over them. Commonly, higher disorder at the structural defect site provides a large number of modes of energy dissipation resulting in higher friction.

Xiao et al.[109] showed that the frictional properties of alkyl-silane monolayers self-assembled on mica in contact with the silicon nitride AFM tips depend strongly on the length of the alkyl chains. They observed that the friction is high for the short chains compared to the longer ones. In organic molecules, van der Waals interactions between the molecules play a very important role in stabilizing the close packing and self-organization of the molecules. The stabilizing energy increases with the length of the chains. Higher friction in case of short chain molecules is thus attributed to the presence of a large number of dissipative modes due to higher disorder in short chain molecules.[109] This study indicates that the chemical nature of the exposed end groups is not sufficient to determine the frictional properties of the monolayer films.

Haugstad et al. observed a difference in the frictional response of the tip, when the tip scans over crystalline and amorphous regions of water soluble polyvinyl alcohol (PVOH).[110] The amorphous region show higher friction than the crystalline region. They suggested that the interfacial dissipation contribution to the friction due to the continuous breaking and making of bonds at the interface is of lesser importance. The dominant energy dissipation mechanism in many polymers is the shear stress induced thermal transitions between different rotational isomers that is especially enhanced in amorphous regions, and if solvent plasticized at high relative humidity. They also observed that the total energy dissipation is approximately a factor of five times greater than the viscoelastic dissipation throughout a volume traced by the tip suggesting that the strain field does not disappear abruptly at a particular distance. Friction force sensitivity to the structural defects can also be used to detect defects,[92] such as dislocations.

3.3.4 Friction Anisotropy

Tip-sample interaction depends on the molecular/atomic orientation and structure of the interface, giving rise to friction anisotropy. There can be some crystallographic directions where the slip is easier than the other crystallographic directions. This gives rise to directionality dependence of friction. Many reports have been published describing the anisotropic behavior of friction in different materials.[111,112,113]

Falvo et al. manipulated carbon nanotubes on graphite using a friction force microscopy tip. They observed a dramatic increase of the lateral force when the directions correspond to commensurate contact.[114] These observations raise the issue of commensurability. If the sliding materials possess no preferred relative orientation, there should be no resistance to relative sliding. Hirano et al. showed that the friction between two mica sheets is maximum when the orientation of both the sheets matched, while the relative misorientation decreased the friction by a factor of four.[115]

Liley et al. observed flower-shaped islands of a lipid monolayer on mica, which consists of domains with different molecular orientation, as shown in Fig. 3.8.[93] They performed FFM in the wearless regime and observed friction anisotropy as well as friction asymmetry. By friction asymmetry, the author meant that the difference in the magnitude of friction of the same region in forward and reverse scan. The angular dependence of the friction reflects the tilt direction of the alkyl chains of the monolayer on mica. They observed that even a tilt of 15 ^{o} is enough to give a good contrast in the friction image.

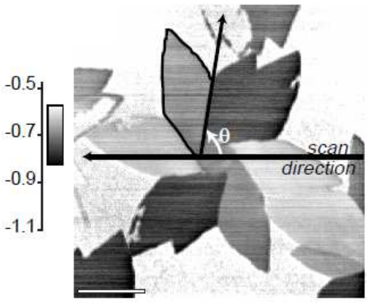

Figure 3.8 Friction image of a thiolipid monolayer on mica surface[93] From M. Liley, D. Gourdon, D. Stamou, U. Meseth, T. M. Fischer, C. Lautz, H. Stahlberg, H. Vogel, N. A. Burnham, and C. Duschl, *Science*, 280, 273 (1998). Reprinted with permission from AAAS.

Park et al. observed strong friction anisotropy when the twofold-symmetry surface of an atomically clean aluminum-nickel-cobalt quasicrystal slide against a thiol-passivated titanium-nitride tip. The frictional force dropped by a factor of eight, when the tip scanning direction changes from a periodic direction to an aperiodic direction. They proposed that the two factors which account for friction anisotropy are dissipation of energy by electronic and phononic contributions, where the energy is dissipated via excitation and propagation of electron hole pairs and phonons, respectively.[116] They also measured the lateral twisting of the cantilever on an amorphous SiO_2 as a function of angle between the scanning direction and the cantilever long axis. They found out that when the scanning direction is same as the direction of cantilever long axis i.e. at $\theta = 90^o$ or -90^o, there is no lateral twisting of the cantilever.

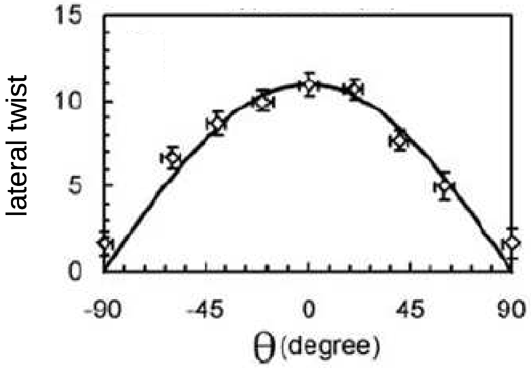

Figure 3.9 Lateral twisting of the tip as a function of the angle between the scanning direction and the long axis of the cantilever[116] From J. Y. Park, D. F. Ogletree, M. Salmeron, R. A. Rebeiro, P. C. Canfield, C. J. Jenks and P. A. Thiel, *Science*, 309 1354 (2005). Reprinted with permission from AAAS.

Figure 3.9 shows that the lateral response of the cantilever on an amorphous SiO_2 is maximum when the scanning direction is perpendicular to the long axis of the cantilever (i.e. at $\theta = 0^0$) and is zero when the scanning direction is parallel to the long axis of the cantilever (i.e. at $\theta = 90$ or -90^0). Zero lateral response when scanning parallel to the cantilever long axis suggests that no net force acts on the cantilever in a direction perpendicular to the direction of motion. At an atomic level, the forces from both sides of the tip balance each other (acting perpendicular to the long axis of the cantilever), due to the amorphous nature of the SiO_2. But if we take a crystalline sample, will the response be still zero while scanning parallel to the cantilever long axis? The answer to this question is addressed below.

3.4 Transverse Shear

Last et al. first reported a variation in the lateral force images when the cantilever orientation is changed with respect to the scanning direction. They imaged a completely coalesced monolayer with a structure mimicking (001) layer of β-$(ET)_2I_3$. Figure 3.10 shows that when the principal cantilever axis is perpendicular to the scanning direction there is a frictional contrast due to the grain boundaries but the frictional contrast between different grains is negligible. When the principal cantilever axis is parallel to the scanning direction the contrast between different grains is accentuated. They proposed that lateral force imaging can be employed to visualize domains in two different modes: the 90^0 scanning mode for visualizing domain boundaries and the 0^0 scanning mode for visualizing friction differences among different domain surfaces.[117]

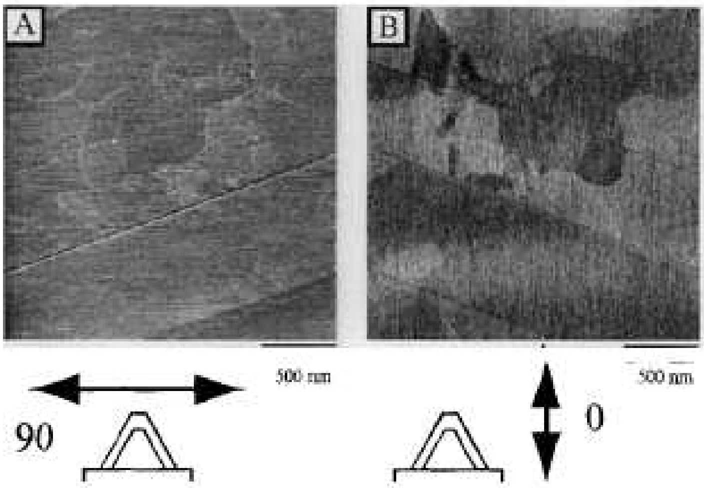

Figure 3.10 Lateral force images of a completely formed monolayer with a structure mimicking the hexagonal (001) layer of β-(ET)$_2$I$_3$. (a) Cantilever oriented perpendicular to the scan direction and (b) cantilever oriented parallel to the scan direction[117] J. A. Last and M. D. Ward, *Advanced Materials*, 8 730 (1996). Copyright Wiley-VCH Verlag GmbH & Co. KGaA. Reproduced with permission.

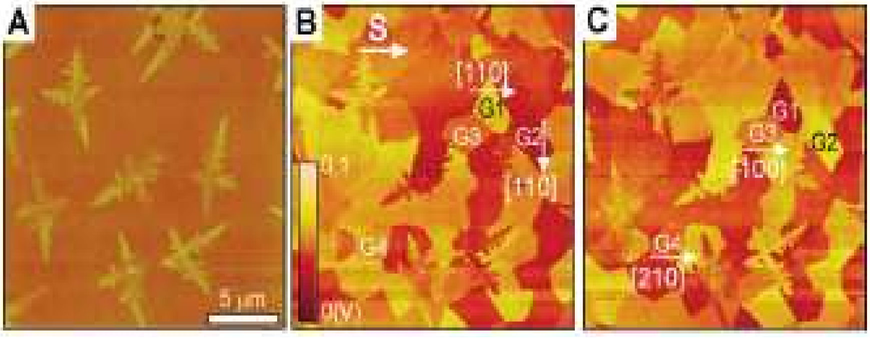

Figure 3.11 Second monolayer dendritic islands of pentacene on completely coalesced first monolayer. (a) Topography, (b) Transverse shear trace image and (c) Transverse shear retrace image[30] K. Puntambekar, J. Dong, G. Haugstad, C. D. Frisbie, *Adv. Funct. Mater.*, 2006, 16, 879. Copyright Wiley-VCH Verlag GmbH & Co. KGaA. Reproduced with permission.

Puntambekar et al. also observed a striking contrast in cantilever twist between different grains in a polycrystalline pentacene monolayer film on SiO_2, while scanning in a direction parallel to the long axis of the cantilever. They named this variant of lateral force microscopy as the transverse shear microscopy (TSM) because they proposed that the visible contrast between different grains is not due to different friction regions but is due to different orientation of the molecules at the surface with respect to the scanning direction. Different orientation of molecules around the tip shears the tip in a different way and twists the cantilever by a different amount in regions of different molecular orientations (*i.e.*, different grains). Figure 3.11 shows the topography and transverse shear trace and retrace images. The topography image shows no contrast in the first monolayer while the transverse shear images show a contrast within the first monolayer indicating different faceted grains in a polycrystalline first monolayer of pentacene on SiO_2.[30]

This novel technique, which can sense grain specificity of ultra thin layers of organic semiconductors on insulating substrates, is considered to result from different transverse shear fields around the tip in different crystallographic directions. Transverse shear microscopy produces images of remarkable contrast of crystalline organic monolayer films and can be used to study the growth kinetics of organic semiconductor films on insulating substrates. The TSM technique and its applications are discussed in detail in the following chapters.

Chapter 4

Transverse Shear Microscopy: An Introduction

(Contributing Authors: Vivek Kalihari, Greg Haugstad, C. Daniel Frisbie)
(Reprinted with permission from “Distinguishing Elastic Shear Deformation from Friction on the Surfaces of Molecular Crystals”, *Physical Review Letters* 104 (2010))

Elastic deformation on the surfaces of molecular crystals can be measured and imaged using a special variant of lateral force microscopy in which the tip is scanned parallel to the cantilever axis. The shear force sensed transverse to the scanning direction has a distinctly different physical origin than the conventional friction force signal. In particular, the tip velocity and the temperature dependence of the cantilever twist reveal that the transverse shear response in un-activated, while the friction response in activated. Furthermore, a linear elastic deformation model for the tip-sample interaction quantitatively predicts the crystallographic anisotropy of the transverse shear contrast, establishing its connection with elastic deformation. These results impact fundamental understanding of tip-sample shear interactions and also indicate that the relative magnitude of the in-plane elastic tensor components can be measured systematically on crystalline soft materials using lateral force microscopy in the transverse shear mode.

4.1 Introduction

Over the past two decades conventional lateral force microscopy (LFM), also known as friction force microscopy (FFM), has become the primary tribological technique for examining the atomic and molecular basis of friction at surfaces because it detects frictional forces on a nanometer length scale, allowing precise correlation with structure.[85,113,118,119] On the surfaces of molecular materials such as Langmuir-Blodgett films and polymers, FFM has been employed to relate sliding friction to molecular structure and dynamics, for example, low frequency vibrational motions of molecules,[120] crystallographic anisotropy,[93] and polymer side-group rotations.[121,122] Because of the continuing importance of LFM as a primary tribological method, understanding the origin of shear forces at the tip-sample interface remains an important area of investigation.

In this chapter, we demonstrate that an unconventional mode of LFM can distinguish between sliding friction and elastic shear deformation at the surfaces of molecular single crystals. Specifically, when the LFM scan vector is perpendicular to the cantilever axis, as in case of FFM, the cantilever twists due to torque on the tip resulting from friction forces at the tip-sample interface. However, aligning the scan vector *parallel* with the cantilever axis while still monitoring cantilever twist, a mode we term the transverse shear microscopy (TSM),[30,31,32,33] affords improved sensitivity to elastic shear deformation at the crystal surface. Scanning along particular crystallographic directions in the transverse shear mode generates a cantilever torque that can be related quantitatively to the elastic modulus tensor of the crystal. The velocity and temperature dependencies of both the transverse shear and friction signals confirm that the transverse shear response has a fundamentally different physical origin than friction.

The general usefulness of LFM to sense transverse shear, and thereby to discern the elastic modulus tensor, has been either unrecognized or unexploited. We expect it to be general across broad classes of crystalline, soft materials. The quantitative interpretation of transverse shear contrast that we provide here offers an approach for examining elastic anisotropy and corresponding bonding anisotropy at the surfaces of molecular materials. For many samples, especially thin films, determining elastic anisotropy by TSM may be far simpler than bulk shear modulation or tensile testing methods. In addition, it is likely that an understanding of elastic anisotropy in crystalline organic materials will also impact understanding of the interrelationships between intermolecular bonding and other properties such as optical (refractive index) anisotropy, and thermal or electrical conduction anisotropy.

4. 2 Results and Discussion

Our investigations focus on single crystals of a benchmark crystalline organic semiconductor, pentacene ($C_{22}H_{14}$), that has application as the charge transporting layer in organic field effect transistors.[123,124] Figure 4.1A shows an optical image of a pentacene single crystal along with its crystal structure and the unit cell in the **a**-**b** plane. It also demonstrates the herringbone packing of pentacene molecules with a molecular tilt along the $[\bar{1}\bar{1}0]$ diagonal. Charge carrier mobility is an important figure of merit in semiconductors and a significant anisotropy in field effect mobility has been reported for various organic semiconductors including pentacene.[125,126] This anisotropy reflects anisotropy in intermolecular interactions in organic semiconductors which should also be reflected in the elastic properties.

Figure 4.1B shows the schematic of TSM, where the scanning direction of a probe tip is parallel to the cantilever and the signal corresponds to the orthogonal twist of the

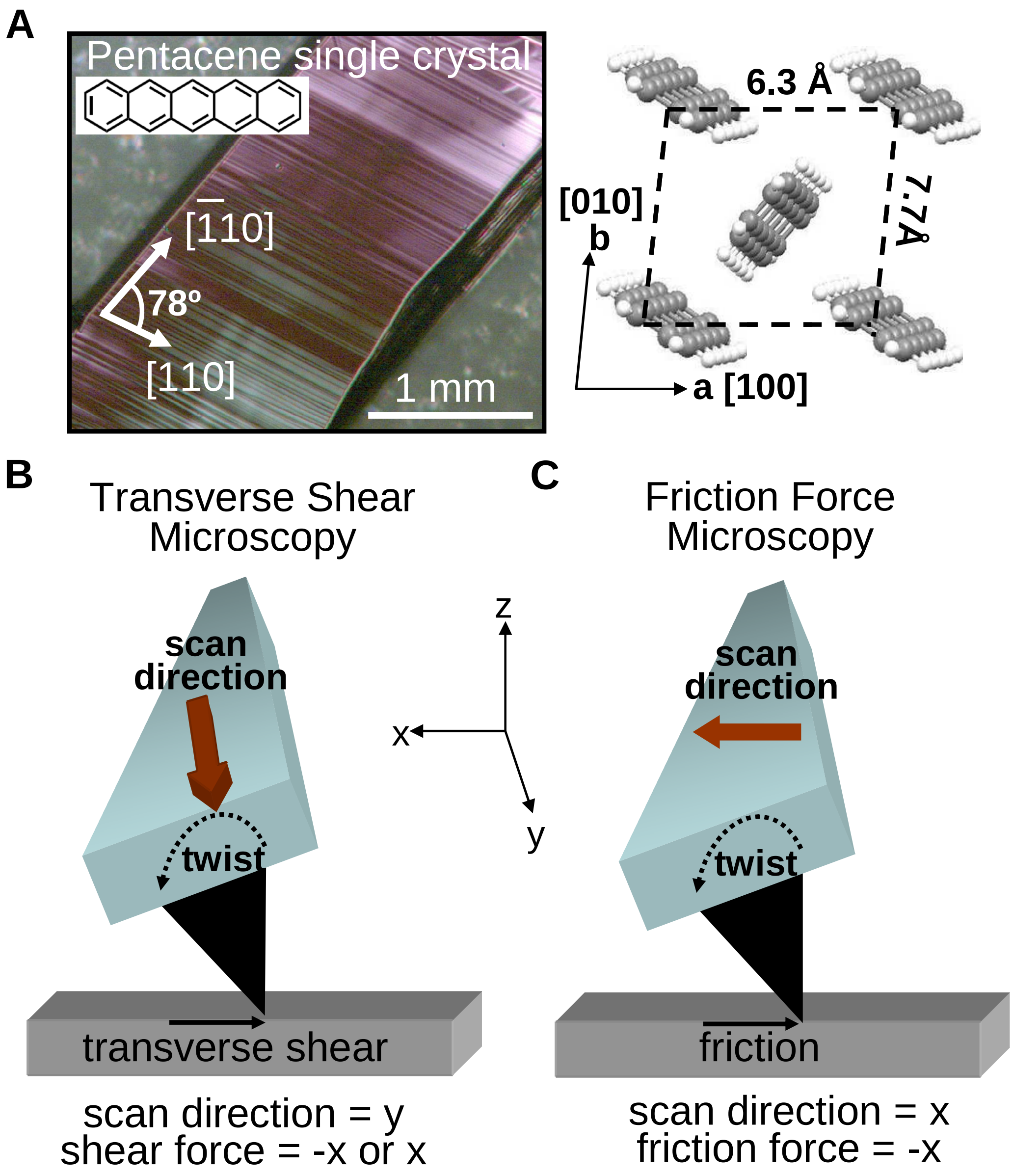

Figure 4.1 TSM and FFM (A) An optical micrograph of pentacene along with its molecular structure and the unit cell in **a-b** plane. It also demonstrates the herringbone packing of pentacene molecules with a molecular tilt along the $[\bar{1}\bar{1}0]$ diagonal. (B) Schematic showing the working mechanism of the TSM, where the scan direction is parallel to the cantilever axis. (C) Schematic showing the working mechanism of the conventional FFM, where the cantilever axis and the scan direction are orthogonal.

compliant cantilever. The only operational difference between TSM and conventional FFM is the scanning direction, *i.e.* in FFM the scanning direction is perpendicular to the cantilever axis (Fig. 4.1C). The alignment of the scan vector along the cantilever axis in TSM means that any twist of the cantilever results from the net shear forces acting in a direction transverse to the scanning direction.

4.2.1 Friction and TSM Loops

Figure 4.2 shows a typical friction loop with positive trace and negative retrace signals. The dashed black line in the center corresponds to the zero twist line. Similar trace-retrace loops are observed in TSM as well (Fig. 4.3) and are used to measure the TSM signal. In FFM, the frictional force is proportional to the width of trace-retrace "friction loops". The FFM trace scan always induces a clockwise twist of the cantilever (a positive signal from the photodetector that monitors the cantilever-reflected laser spot displacement) and the retrace scan always induces a counter-clockwise twist (negative signal). Therefore, the measured frictional force (proportional to trace minus retrace scan) is always positive. In TSM, the trace scan can result in either clockwise or counter-clock twist and the retrace scan results in the opposite twist, as shown in Figs. 4.3A and 4.3B. Hence, a TSM signal (proportional to trace minus retrace scan) can be either positive or negative. Depending on the relative orientation between the scan vector and the surface crystallographic direction, the trace and retrace signals can also overlap along the zero twist line, as shown in Fig. 4.3C. While scanning molecular rough surfaces, the twist of the cantilever has some contribution from the local surface slope as well. In most of the

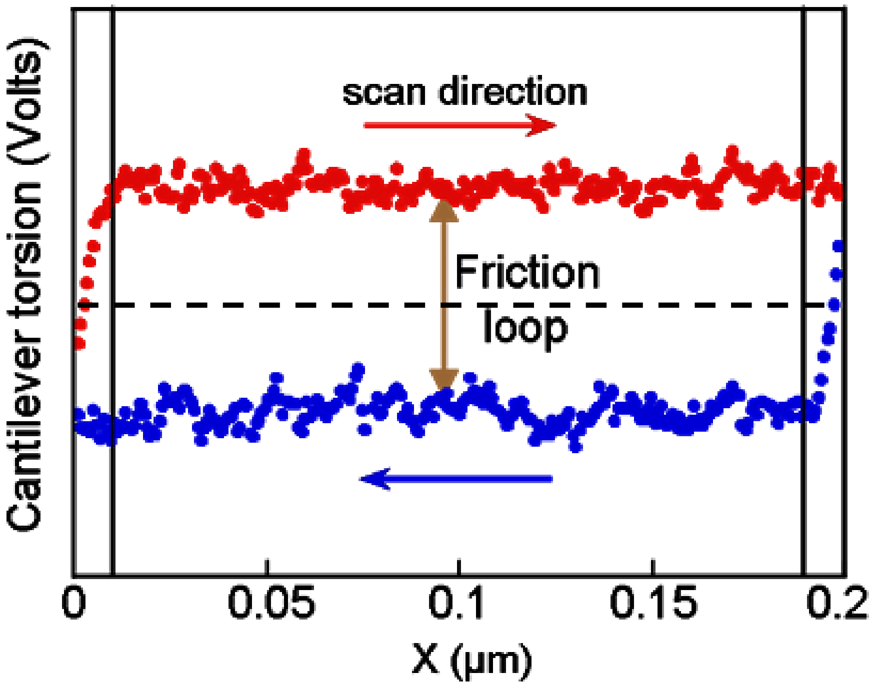

Figure 4.2 Friction Loop In FFM, the fast scanning direction is perpendicular to the long axis of the cantilever such that the friction force acting at the tip-sample interface exerts a torque about the cantilever axis and twists the cantilever. The sense of twisting changes when the scan direction of the tip changes, i.e., the twist is always clockwise (positive signal) during trace scan and counter clockwise (negative signal) during retrace scan. This twisting dependence on the scan direction gives rise to a friction loop as shown above. Width of the loop is directly proportional to the dissipative energy which indicates the magnitude of sliding frictional force.

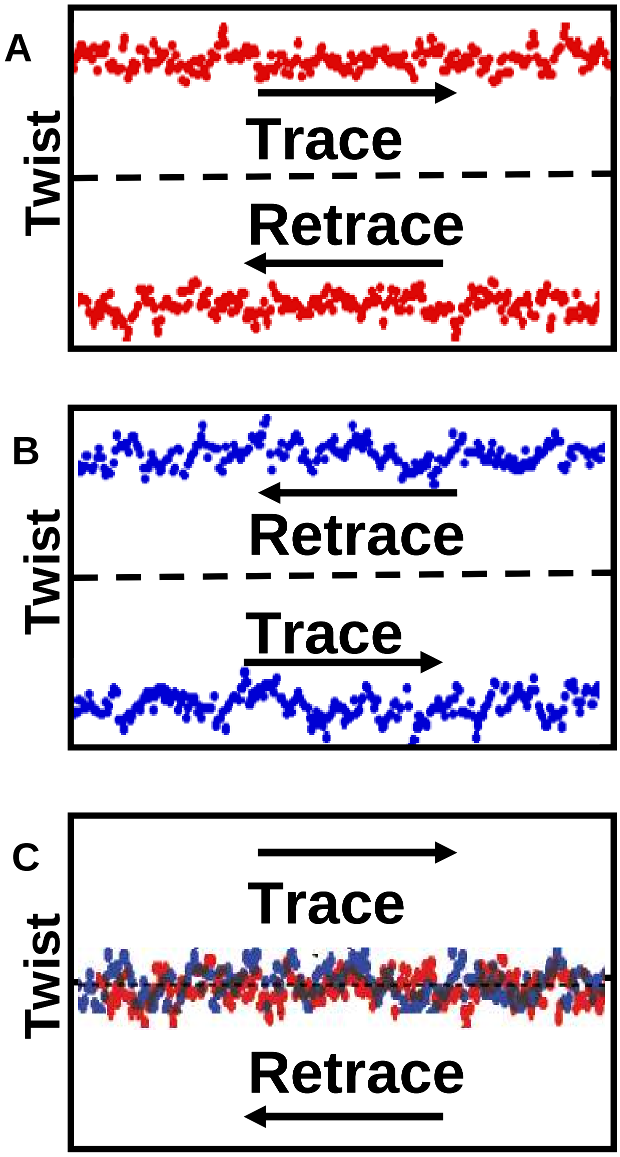

Figure 4.3 TSM Loops In TSM, the trace scan result in either (A) clockwise or (B) counter clockwise twist and the retrace scan results in the opposite twist. Hence, a TSM signal (proportional to trace minus retrace scan) can be either positive or negative. This is different from FFM, as the friction signal is always positive. Depending on the relative orientation between the scan vector and the surface crystallographic direction, the trace and retrace signals can also overlap along the zero twist line, as shown in (C).

cases, the topographic contribution can be quantified and removed to a first approximation by subtracting the trace and retrace scans.

The conventional approach to analyze friction is to study the friction as a function of tip-velocity, sample temperature, and applied normal load.[102,121,122,127,128] In order to understand the fundamental difference between TSM and FFM, we followed the same approach and measured the TSM and FFM signals as a function of velocity and sample temperature on an indexed pentacene single crystal.

4.2.2 TSM and Friction as a function of Tip-Velocity

Figure 4.4A plots the friction as a function of logarithmic velocity along different crystallographic directions at room temperature. The plot clearly indicates that the friction is initially velocity dependent and anisotropic. The magnitude of the friction is highest along the diagonal [110] and lowest along the other diagonal $[\bar{1}10]$. Along the **a** axis [100] and the **b** axis [010] there is no significant difference in friction (both the directions are represented by a single curve) and the friction magnitude lies between those along the two diagonals. There is a logarithmic increase of friction with velocity in the lower velocity regime (0.1 - 1.0 µm/s) and constant friction in the higher velocity regime (greater than 1.0 µm/s). This trend is observed for all the crystallographic directions as shown in the Fig. 4.4A. Similar friction dependence on tip-velocity has been experimentally observed and rationalized by a modified Tomlinson model,[102,129] where at lower velocities the atomic friction increases logarithmically with velocity due to the

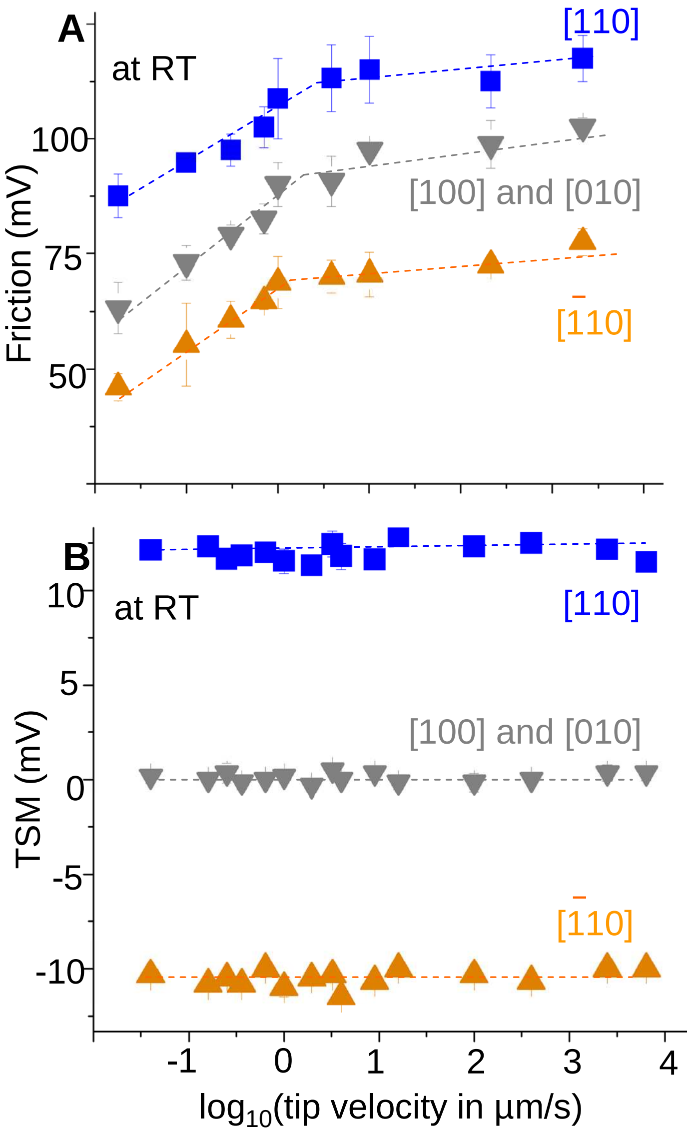

Figure 4.4 Friction and TSM signal as a function of Tip-Velocity (A) Semi-logarithmic plot of friction versus tip-velocity at room temperature along different crystallographic directions on an indexed pentacene crystal. At lower velocity regime (less than 1µm/s), the friction increases with tip-velocity but saturates at higher velocities (greater than 1µm/s). (B) Semi-logarithmic plot of TSM versus tip-velocity at room temperature. The TSM signal shows anisotropic behavior, but remains constant as a function of tip-velocity over five orders of magnitude.

thermally activated hopping of the contact atoms, but at higher velocities friction is constant as thermal activation ceases to be relevant. On the other hand, the TSM response, Fig. 4.4B, is completely independent of velocity over five orders of magnitude at room temperature. Like friction, TSM is anisotropic, *i.e.*, the TSM signal is positive along [110], *negative* along $[\bar{1}10]$, and zero for both the **a** [100] and **b** [010] axis. Importantly, the absence of velocity dependence for the TSM signal indicates that the physical origin of the transverse shear force is fundamentally different from friction. Specifically, the friction response is activated while transverse shear response in not activated.

4.2.3 TSM and Friction as a function of Temperature

In order to gain more insight into the difference between the FFM and TSM signals, we measured their dependence on crystal temperature. Figures 4.5A and 4.5B show friction and TSM loops at different crystal temperatures, respectively. It is evident from the plot that the friction loops collapse (the signal gets smaller), whereas the TSM loops remain constant with an increase in crystal temperature. The loops presented in Figs. 4.5A and 4.5B were taken along [110], but the other crystallographic directions also showed similar behavior. This observation is consistent with expectations that friction is thermally activated, while transverse shear is not. Further, we probed the origin of friction by performing the conventional time-temperature superposition analysis and calculated the activation energy for friction.

4.2.4 Activation Energy for Friction

Figure 4.6A shows the friction versus crystal temperature plot for [110] and $[\bar{1}10]$, where the friction acting between the probe tip and the crystal surface decreases sharply at higher temperatures (beyond ~ 60ºC). On the other hand, the TSM signal is found to be independent of the crystal temperature in the temperature range 25ºC -75ºC along different crystallographic directions (plot not shown). At crystal temperatures above 85ºC the height images of pentacene crystals show some wear at the surface, thus the highest temperature was limited to 75 ºC in both the FFM and the TSM experiments.

In order to further investigate the nature of friction and its activation energy, we employed the method of rate-temperature superposition.[121,122] Figure 4.6B shows isothermal friction versus tip-velocity along [110] for 7 nN applied normal load. The plotted temperature (62 ºC to 75 ºC) and velocity (less than 1 µm/s) regimes were chosen because the friction showed activated behavior in these regimes. Figure 4.6C shows the superimposed data onto a master curve from a single horizontal shift factor (a_T) for each temperature. The Arrhenius dependence of the a_T shown in Fig. 4.6D clearly identifies friction as an activated process and the slope of the plot can be used to calculate the activation energy.

Figure 4.6D also demonstrates that the activation energy increases with an increase in normal load: 4 nN = 6 kcal/mol, 7 nN = 20 kcal/mol, 14 nN = 42 kcal/mol, and 22 nN = 52 kcal/mol. In order to explain this phenomenon, we need to consider the shear and the compressive stresses acting at a tip-sample interface. In both traditional rheology and friction force microscopy,[130,131,132] elevated shear stress on polymers can

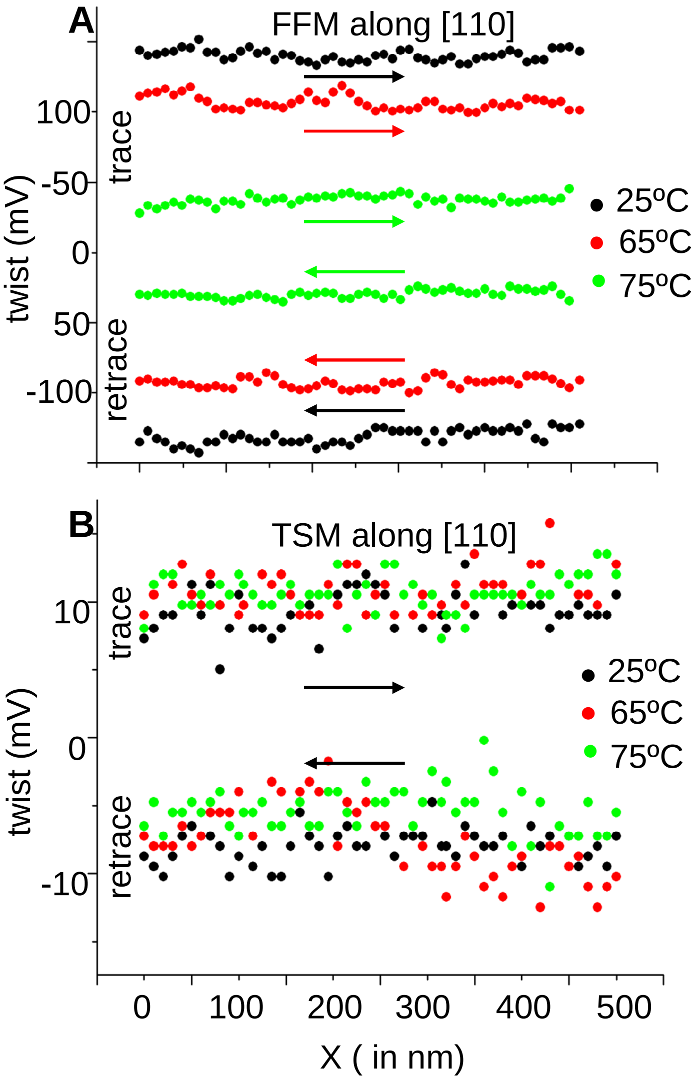

Figure 4.5 Friction and TSM Loops as a function of Substrate Temperature (A) Friction loops (trace and retrace scans) as a function of pentacene crystal temperature. The width of the friction loops decreases with an increase in temperature, i.e., the friction signal decreases with an increase in sample temperature. (B) TSM loops as a function of pentacene crystal temperature. The width of the TSM loops remains constant with an increase in temperature, i.e., the TSM signal is independent of pentacene crystal temperature.

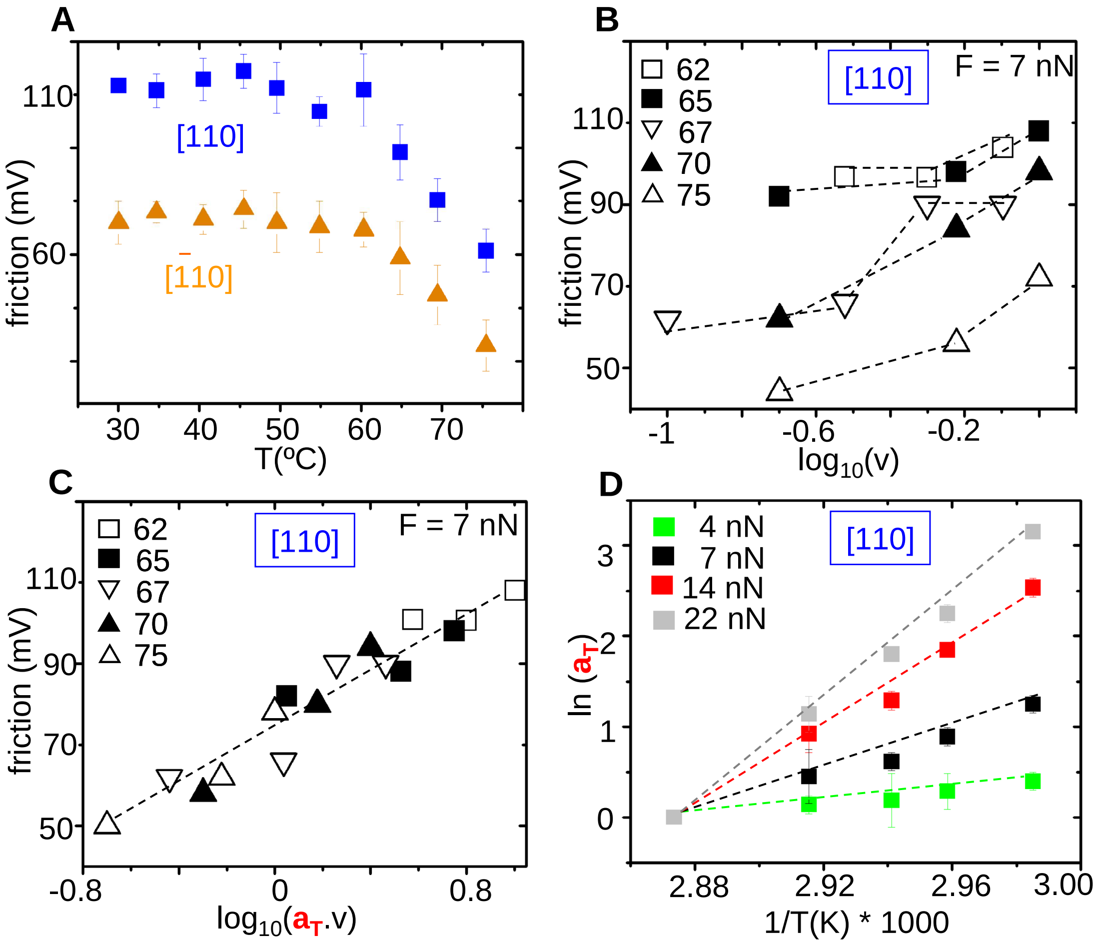

Figure 4.6 Time-Temperature Superposition for Friction (A) Friction versus crystal temperature plot along [110] and $[\bar{1}10]$ directions. (B) Isothermal friction versus tip-velocity plot along [110] for 7 nN applied normal load. (C) Master curve obtained from the superposition of different curves in panel B using a fitting parameter (a_T) for each temperature. (D) The Arrhenius dependence of a_T at different applied normal loads. The slope of the plot is used to calculate the activation energy of friction.

aid the activation of dissipative molecular motions (non linear response), even if experimentally actuated by an elevated loading force (*i.e.*, via the friction-load relationship); whereas on simple inorganic crystalline systems, elevated loading force has been found to hinder activation, suggesting the dominance of compressive stress.[102] In the present case, an observed increase in activation energy with increasing normal load can be rationalized by the presence of dominant compressive stresses at the pentacene crystal-tip interface. Another important observation is that the activation energy shows no anisotropy within a standard deviation of ± 2 kcal/mol. This is an interesting observation because the friction magnitude is anisotropic, but the related activation energy is isotropic. This observation suggests that the origin of friction is a single activated mode and the cantilever dissipates different “chunks” of the dissipated energy while scanning along different crystallographic directions. This intriguing behavior is the subject of ongoing investigation.

4.2.5 Mathematical Equation for TSM

The different velocity and temperature dependence of friction and transverse shear clearly indicates that their physical origins are different. Specifically, the absence of velocity and temperature dependence for the TSM signal suggests that it is related to elastic deformation at the tip-sample interface. To probe this hypothesis, we developed a mathematical model using the theory of linear elasticity[133] describing elastic deformation acting at a tip-sample interface. This model is a substantial improvement of our previous model which proved only that the TSM signal will be zero for an isotropic material independent of the scanning direction (see Appendix A). The improved model is general and can be used to calculate the elastic deformation and hence, the TSM signal in terms of the components of the elastic tensor for any material (see Appendix B). The general equation describing the TSM signal in an image plane containing principal directions (1 and 2) is given by:

$$
\begin{aligned}
TSM = G[&E_{1111}(-\cos^3\theta\sin\theta) + E_{2222}(\cos\theta\sin^3\theta) + 2E_{1212}(2\cos^3\theta\sin\theta - 2\cos\theta\sin^3\theta) + \\
&E_{1122}(\cos^3\theta\sin\theta - \cos\theta\sin^3\theta) + 2E_{1112}(-3\cos^2\theta\sin^2\theta + \cos^4\theta) + \\
&2E_{2212}(3\cos^2\theta\sin^2\theta - \sin^4\theta)]
\end{aligned}
$$

where G is a lumped constant with units of V/Pa describing the cantilever-tip geometry, the sample strain, the tip-sample contact area, and the instrument sensitivity, θ is the angle between the scanning direction and the principal direction 1, and E_{ijkl} are components of the fourth order elastic modulus tensor with units of Pa.

The above equation for the TSM signal describes the cantilever twist based on the components of the in-plane elastic modulus tensor and it goes to zero for an isotropic material. Figure 4.7A shows the experimental TSM data (filled triangles) obtained on a pentacene single crystal and the corresponding fit (solid line) based on the TSM equation. For the TSM calculations, we took the (1-2) plane as the (**a**-**b**) plane because the crystal plane under analysis is the **a**[100]-**b**[010] plane of pentacene. The fit can be used to calculate the relative **a-b** plane elastic constants for pentacene single crystals which are: $E_{1111} \sim 1.8\ E_{2222}$, $E_{1212} \sim 0.2\ E_{2222}$, $E_{1122} \sim 0.6\ E_{2222}$, $E_{1112} \ll E_{2222}$, and $E_{2212} \ll E_{2222}$. In order to verify the accuracy of the calculations and the fit, we compared the obtained relative magnitudes of elastic constants of pentacene with that of anthracene single crystal.[134] The similar molecular structure and herringbone packing of anthracene and

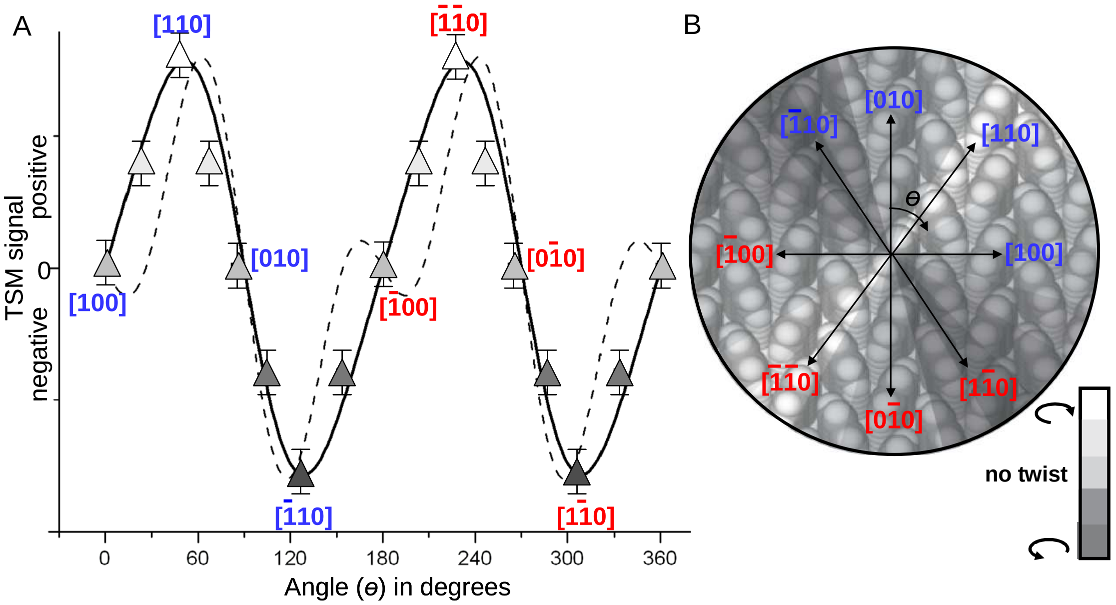

Figure 4.7 TSM: Experiments versus Mathematical Modeling (A) Plot of TSM signal versus scanning direction (θ). An excellent agreement between the experimental TSM measurements (filled triangles) and the modeled TSM signal (solid line) indicates that the origin of TSM is elastic anisotropy at the sample surface. The figure can be used to calculate the relative **a-b** plane elastic constants for pentacene single crystal which are: E_{1111} ~ 1.8 E_{2222}, E_{1212} ~ 0.2 E_{2222}, E_{1122} ~ 0.6 E_{2222}, E_{1112} « E_{2222}, and E_{2212} « E_{2222}. The dashed line represents the modified TSM plot when the value of E_{1212} is increased by ~ 60 %.(B) Schematic showing the angular dependence of TSM signal overlaid on a pentacene single crystal structure.

pentacene molecules makes anthracene's elastic constants an excellent choice, as the relative magnitudes of different elastic constants should be similar in the two organic crystals. In fact, a good agreement between the relative magnitudes of elastic constants in the two crystals indicates that the origin of TSM is elastic anisotropy at the sample surface, and that the elasticity model can predict the TSM signal.

Figure 4.7B is a scheme depicting the angular dependence of the TSM signal (or image contrast) on a pentacene single crystal structure. The color variation in the diagram demonstrates that the TSM signal is zero for scan directions along the **a** [100] and **b** [010] axes. The maximum clockwise (positive) twist is obtained when scanning along the [110] diagonal, whereas maximum counter-clockwise (negative) twist is obtained when scanning along the $[\bar{1}10]$ diagonal.

The detection of elastic shear deformation by TSM of course implies that such deformation also occurs in conventional FFM, as expected. However, comparison of the TSM and friction signals in Figs. 4.2 and 4.3 reveals that the TSM signal is at least a factor of 10 smaller, meaning that in FFM the effects of elastic deformation on sliding friction are masked by the much larger contributions of activated, stick-slip behavior to the total friction signal. The reason TSM is sensitive to elastic deformation is that when the scan vector is parallel to the cantilever, the activated, stick-slip phenomena are much less likely to generate a torque about the cantilever axis.

4.3 Conclusion

In conclusion, we have demonstrated that elastic shear deformation forces on molecular surfaces can be cleanly detected using a variant of lateral force microscopy, termed transverse shear microscopy. Tip velocity and temperature-dependent measurements demonstrate that both conventional FFM and TSM reveal anisotropy on crystalline organic surfaces, but that FFM is activated while TSM is non-activated. A linear elasticity model accurately captures the TSM response in terms of the components of the in-plane elastic modulus tensor of the material, which in turn indicates that the relative magnitude of the in-plane tensor components can be determined from the crystallographic dependence of the TSM contrast. In addition, the ability to image elastic anisotropy at high resolution is useful for microstructural characterization of soft materials, and for relating other physical properties (*e.g.*, optical, thermal or electrical anisotropy) to bonding anisotropy in such systems.

4.4 Experimental

Single crystals of pentacene were grown from a high purity source (99.8 %) through horizontal physical vapor transport and they were indexed using a Bruker diffractometer fitted with an area detector. The TSM and FFM experiments were conducted on a Molecular Imaging PicoPlus SPM (now Agilent model 5500): this is an environmentally controlled, tip-scanned system with a sample heating stage. Humidity was kept constant at ~20 % throughout the experiments. The probes used for AFM experiments were uncoated silicon “diving board” cantilevers with integrated contact mode tips fabricated by MikroMasch, USA (model NSC36 and force constant ~ 0.95 Nm^{-1}). Each probe was used for both TSM and FFM measurements to remove the tip dependence of the measured signal. Pentacene single crystals were manually rotated under the force microscope in order to measure the TSM and FFM signals along different crystallographic directions. A constant normal load (~ 2 nN) was applied during the variable temperature and velocity experiments. During the variable temperature experiment, the cantilever deflection set-point was adjusted after every temperature step using force curve analysis in order to compensate for thermal drift.

4.5 Acknowledgement

We would like to thank Y. Xia and W. Xie for providing single crystals for the experiments. This work was partially supported by the MRSEC Program of the National Science Foundation under Award Numbers DMR-0212302 and DMR-0819885. Partial support was provided by NSF through DMR-0706011. Parts of this work were carried out in the Institute of Technology Characterization Facility, University of Minnesota, which received partial support from NSF through the NNIN and MRSEC programs.

Chapter 5

Microstructural Characterization of Polycrystalline Organic Semiconductor Monolayers

(Contributing Authors: Vivek Kalihari, E. B. Tadmor, Greg Haugstad, C. Daniel Frisbie)
(Reprinted with permission from “Grain Orientation Mapping of Polycrystalline Organic Semiconductor Films by Transverse Shear Microscopy”, *Advanced Materials* 20 (2008))

The microstructure of ultrathin organic semiconductor films on gate dielectrics plays a pivotal role in the electrical transport performance of these films in organic field effect transistors (OFETs). Unfortunately, conventional materials characterization techniques such as scanning electron microscopy and tunneling electron microscopy cannot be used to probe these ultrathin films because of the issues related to beam damage, requirement of conductive substrates, and rigorous sample treatment. Here we demonstrate that a novel scanning probe microscopy method, which we term Transverse Shear Microscopy (TSM), produces striking, high contrast images of grain size, shape, and *orientation* in films of polycrystalline organic materials. Specifically, the grain orientation mapping by TSM can be employed to quantify grain morphology, grain boundary density and the relative proportion of high-angle grain boundaries in ultra-thin organic semiconductor monolayers grown on common dielectrics.

5.1 Introduction

Polycrystalline organic semiconductor films play a central role in organic electronics because their inherent order, relative to amorphous films, facilitates more efficient charge transport. Carrier mobilities in crystalline organic semiconductors are generally at least a factor of one hundred greater than in their amorphous counterparts, which is attractive for certain device applications, such as OFETs, where higher charge mobilities result in better performance.[135,136,137,138,139]

In analogy with conventional semiconductors (*e.g.*, poly-Si), the electrical performance of polycrystalline organic semiconductor layers is sensitive to grain morphology and alignment, as well as to defects.[10,123,140,141,142,143] Indeed, recognition of the importance of microstructure has lead to extensive structural characterization of organic semiconductor films by X-ray diffraction[144,145] and optical,[146] electron,[22,23,24,147] and scanning probe microscopy.[30,31] Yet there are still many aspects of organic semiconductor microstructure that are not well understood and detailed correlations with transport are rare. One surprising bottleneck to understanding microstructure-property relationships has been the difficulty of producing clear images of grains in extremely thin, coalesced layers of organic semiconductors on technologically relevant substrates, such as gate dielectrics, which are critical components of OFETs.

Here we demonstrate that a novel scanning probe microscopy method, which we term TSM, produces striking, high contrast images of grain size, shape, and *orientation* in films of polycrystalline organic materials. The ability to image grain orientation is a key feature of TSM and the resulting Grain Orientation Maps substantially enhance the possibilities for quantitative analysis of microstructure. For the ultrathin (1-2 nm) organic films we describe here, the grain orientation and shape recorded in the TSM images are difficult to visualize by any other microscopy method. Furthermore, by combining shear deformation experiments with theoretical analysis, we show that the mechanism of TSM orientation contrast originates from the intrinsic elastic anisotropy within individual grains. Thus, TSM has intriguing potential as a broadly applicable method for quantitative microstructure analysis, not only for organic semiconductors, but for any suitably soft, crystalline material with a tensor modulus in the image plane. Our results substantially expand on an earlier report of TSM imaging[30] in which we demonstrated orientation dependent contrast but did not analyze the film microstructure nor identify the imaging mechanism.

5.2 Results and Discussion

5.2.1 TSM: Working Mechanism

In TSM, depicted in Figure 5.1, the scanning direction of a force microscope probe tip is *parallel* to the cantilever axis, and the lateral deflection or twist of the cantilever is recorded with the help of a laser-position sensitive photodetector set-up. This mode of operation differs from the better-known friction force microscopy (FFM) technique in one respect only, namely that in FFM the scanning direction is *perpendicular* to the axis of the cantilever. In FFM, the cantilever twist is governed by the net friction force acting at the tip-sample interface. Whereas, the alignment of the scan vector parallel to the cantilever axis in TSM means that any observed twisting of the cantilever results from net shear forces on the probe tip that are transverse to the scanning direction. Relative to FFM, TSM has enhanced sensitivity to the elastic deformation properties of crystals and thus can reveal crystallographic orientation in situations where

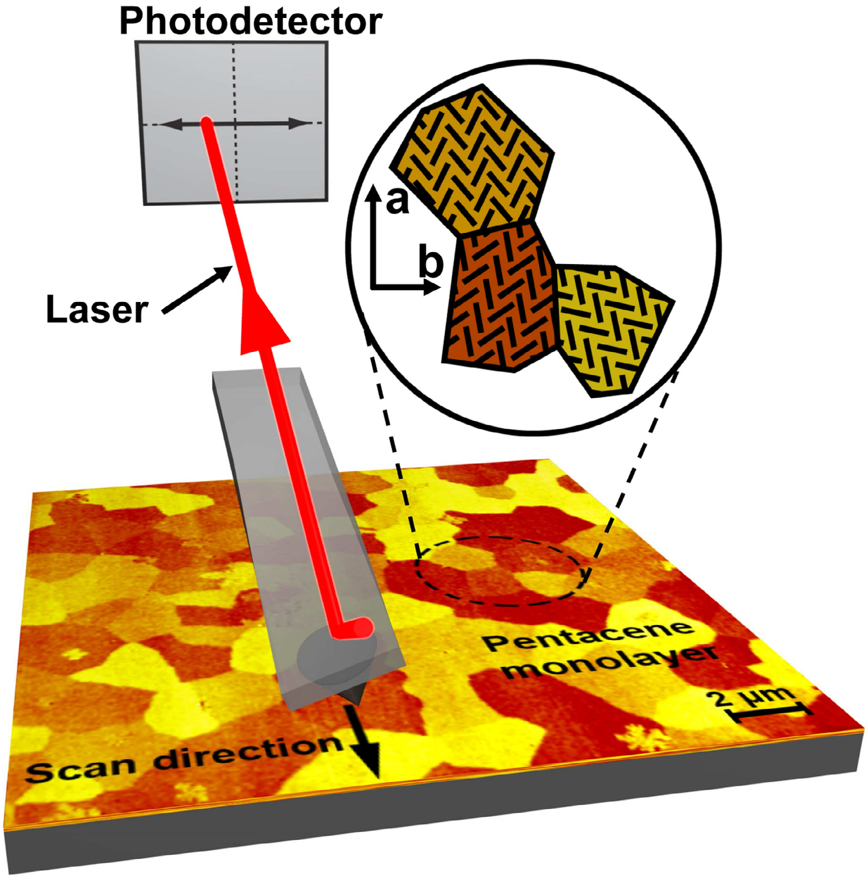

Figure 5.1 Transverse Shear Microscopy (TSM). Scheme illustrating the working mechanism of TSM. The twisting of the cantilever is detected by a deflected laser beam which hits a position sensitive photo-detector. When scanning in a direction parallel to the cantilever long axis, the cantilever twist depends on the crystallographic orientation of the grain under the tip. The exploded view depicts the herringbone packing motif of pentacene molecules within the a-b plane of each grain and the relative grain orientation.

FFM cannot. It is important to note that LFM has been used previously to determine chain orientation in crystals of polymers.[148,149,150] However, the sensitivity of TSM to elastic properties distinguishes it from FFM in which dissipative (frictional) forces dominate, a point that is born out by direct comparison of FFM and TSM images.

5.2.2 Pentacene Monolayer Films

Our investigations focus on ultrathin films of the benchmark organic semiconductor pentacene that have application as the active layers in OFETs. Pentacene ($C_{22}H_{14}$) is a polycyclic aromatic hydrocarbon molecule consisting of five linearly-fused, six carbon rings, and it packs in a triclinic unit cell. Figure 5.2 shows the molecular structure of pentacene along with the face to edge packing motif (herringbone packing) for pentacene molecules on SiO_2 substrates (where all the molecules are standing upright on the substrate). The exceptional performance of pentacene films in OFETs is ascribed to the favorable crystal packing and the textured, polycrystalline film morphology (all grains are oriented with the [001] direction approximately perpendicular to the substrate) which result in a high degree of intermolecular π-orbital overlap in the plane of the film.[9,67 ,151,152] Because the gate-induced charge in an OTFT is electrostatically confined to an ultra-thin portion of the organic semiconductor nearest the gate dielectric, it is the crystalline packing and microstructure of the first few molecular monolayers of pentacene immediately adjacent to the dielectric surface that are critical for transistor performance.[124,153]

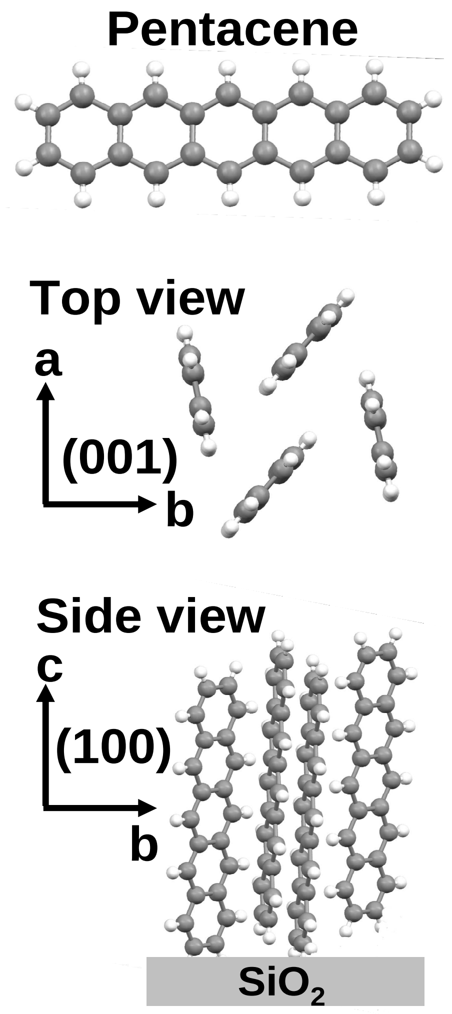

Figure 5.2 Pentacene: Molecular Structure and Packing Top view and side view of the layered, crystalline packing of pentacene molecules in the a-b plane. On SiO_2 substrates, grains are oriented with the a-b plane parallel to the substrate (as the (001) plane has the minimum energy) and the molecules are standing upright on the substrate.

X-ray diffraction experiments have established the polycrystallinity and unit cell structure of pentacene monolayers and multilayers on typical dielectrics, such as SiO_2.[18,72] However, direct imaging of the microstructure of ultra-thin (1-2 nm), coalesced layers of pentacene, or similar small molecule crystalline organic semiconductors on dielectric substrates, has not been reported by conventional electron or scanning probe microscopy. Tromp and colleagues successfully used photoemission electron microscopy (PEEM) to image the growth of pentacene mono- and multilayers on silicon.[22] They observed significant contrast between isolated pentacene crystallites and the underlying silicon, but the shape of discrete grains in coalesced monolayers was not clearly evident.

5.2.3 TSM of Organic Semiconductor Monolayer Films

Figures 5.3A, B, and C present the topographic, conventional FFM, and TSM images of the same region of a pentacene monolayer film grown on SiO_2 by vapor deposition. The topographic image reveals a nearly featureless coalesced pentacene monolayer, with islands corresponding to the start of second layer growth. In the FFM image (Figure 5.3B), there is substantial contrast between the first and second layers of pentacene, but there is almost no contrast within the first pentacene layer. On the other hand, the TSM image (Figure 5.3C) displays remarkable contrast in the first pentacene layer highlighting the shapes of individual faceted grains. These results are general: we have observed the grain structure in coalesced monolayers of other organic semiconductors with dissimilar packing arrangements on a variety of different substrates

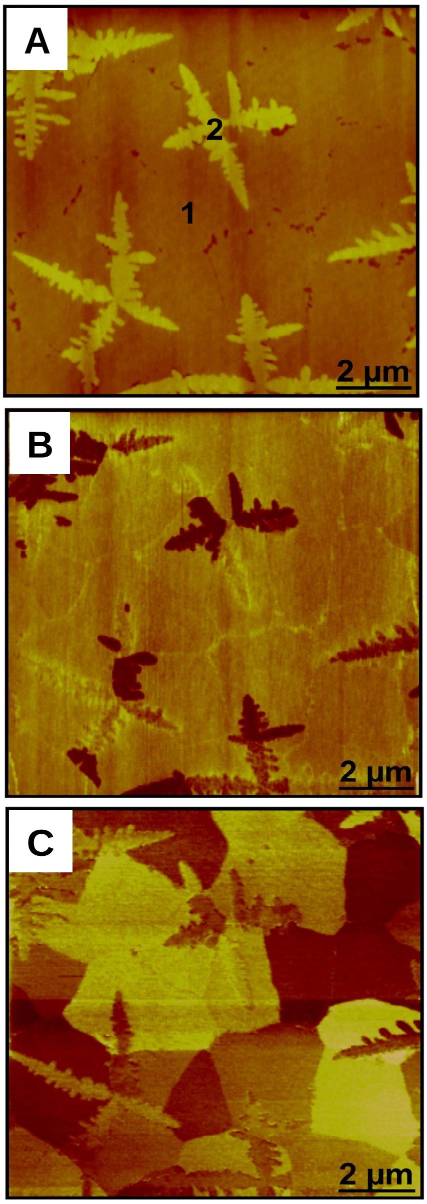

Figure 5.3 TSM versus Friction Images A, B, and C are 10 µm X 10 µm contact mode AFM images of the microstructure of a fully coalesced first monolayer of pentacene grown on SiO_2. A) Conventional topography (height) image showing a few dendritic second monolayer islands on a fully coalesced first monolayer. B) FFM image revealing friction contrast between the first monolayer and the second monolayer, but no contrast within the first monolayer. C) TSM image showing well-defined, faceted grains in the first monolayer. In this image the contrast corresponds to grain orientation.

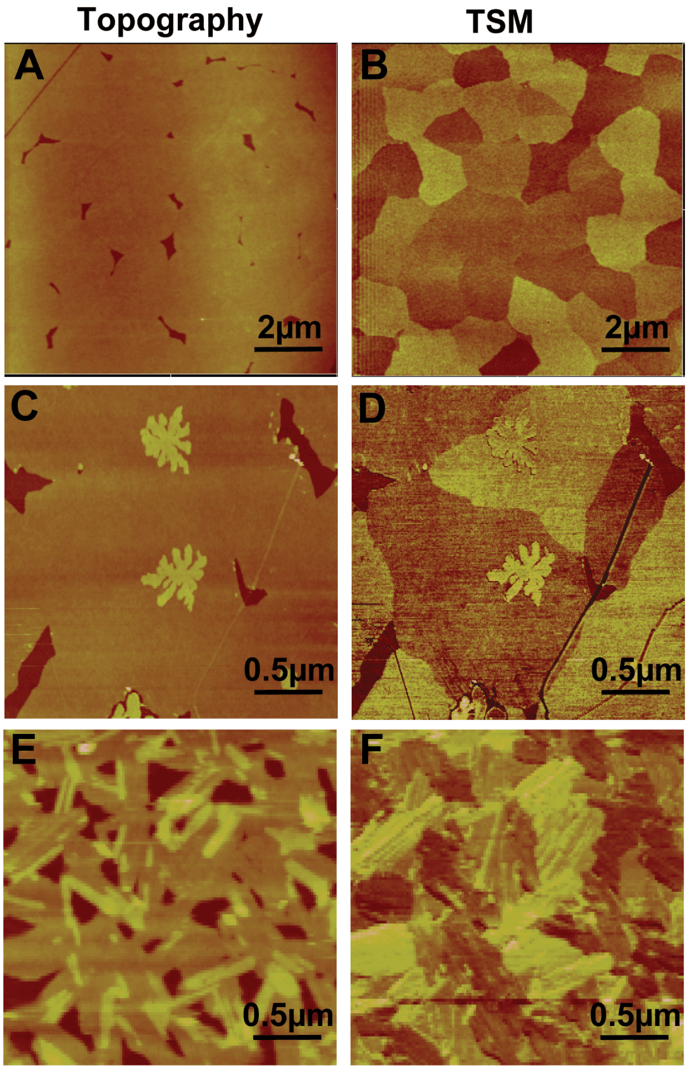

Figure 5.4 Generality of TSM Topography and TSM images of monolayer films of various organic semiconductors on multiple dielectrics. The TSM images reveal grain size and shape, and reflect the generality of this unique technique for imaging different organic semiconductors with dissimilar packing arrangements on a variety of substrates. (A and B) correspond to a monolayer of pentacene (p-type organic semiconductor with a herringbone packing motif) on strontium titanate $SrTiO_3$; (C and D) correspond to a monolayer film of napthalene-2thiophene-napthalene (p-type organic semiconductor with a herringbone packing motif) on SiO_2; (E and F) correspond to perylene tetracarboxylic di-imide derivative PTCDI-C_8 (n-type organic semiconductor with a π-stacking geometry) monolayer on SiO_2.

using TSM. Figure 5.4 shows height and corresponding TSM images of ultrathin films of pentacene on strontium titanate, napthalene-2thiophene-napthalene (p-type organic semiconductor with a herringbone packing motif) on SiO_2, and perylene tetracarboxylic di-imide derivative PTCDI-C_8 (n-type organic semiconductor with π-stacking geometry) monolayer on SiO_2. In all instances, the contrast in FFM and topography images was weak or non existent and did not provide any microstructural information, while in TSM the grain shapes were obvious. The generality of TSM is supported by much earlier work by by Ward[117] who demonstrated that crystalline domains in electrochemically grown molecular monolayers on graphite could be visualized conveniently by TSM, though they did not elucidate the mechanism of contrast, nor the generality of the method.

5.2.4 TSM on Pentacene Single Crystals

The contrast in TSM is clearly not of topographic origin, but is related to the crystallographic orientation of grains with respect to the scanning direction. Several inter-related questions naturally arise, namely, the precise interpretation of TSM contrast, the origin of transverse shear stresses in a scanning probe experiment, and the difference between the shear stresses detected in conventional FFM versus TSM modes. To address these issues, we have carried out TSM analysis on the (001) face of single crystals of pentacene; the crystal structure of bulk pentacene is known and the packing of molecules on this face is analogous to the known packing in a pentacene monolayer on SiO_2.[18,68]

Figure 5.5A displays an optical micrograph of the (001) face of a macroscopic pentacene crystal grown by vapor phase transport. The crystal was indexed by X-ray diffraction. The long axis of the rectangular shaped crystal lies along $[\bar{1}10]$ as shown.

Figure 5.5B depicts the herringbone packing of pentacene molecules in the (001) or a-b plane and several key crystallographic directions. Figures 5.5C, D, and E show the transverse shear signal (*i.e.*, the twisting of the cantilever, as measured by the position sensitive photodetector, versus distance) for different scan vectors on the (001) crystal face. For each scan vector, the crystal was repositioned in the force microscope so that the cantilever axis was parallel with the forward scan vector direction. When the scan vector pointed along $[110]$ (forward scan), Figure 5.5C, the twist signal was positive (+20 mV); for the reverse scan, corresponding to a scan vector in the antiparallel $[\bar{1}\bar{1}0]$ direction, the twist signal was negative and approximately equal in magnitude (-20 mV). We can view the twist signal for the forward and reverse traces in Figure 5.5C as a "clockwise" hysteresis loop. The difference in the TSM signal between the forward and reverse scans in the loop is 40 ± 3 mV, which is the total TSM signal.

Figure 5.5D demonstrates that when the scan vector pointed along $[\bar{1}10]$ and $[1\bar{1}0]$ (forward and reverse scans, respectively) the sign of the twist signal was exactly opposite to that in Figure 5.5C, *i.e.*, we observed a "counter-clockwise" hysteresis loop. The total TSM signal in this case was -34 ± 3 mV, Figure 5.2C. When the scan vector was aligned along $[010]$ or $[100]$, the hysteresis loops collapsed, Figure 5.5E; there was no TSM signal within the ±3 mV noise limit for either forward or reverse scan directions.

The data in panels 5.5A-E demonstrate unambiguously that the *sign and magnitude* of the TSM signal depends on the precise relationship between the scan vector and crystallographic orientation. Importantly, this precise dependence makes it possible to use TSM to index directions on the (001) face of an arbitrary pentacene crystal by

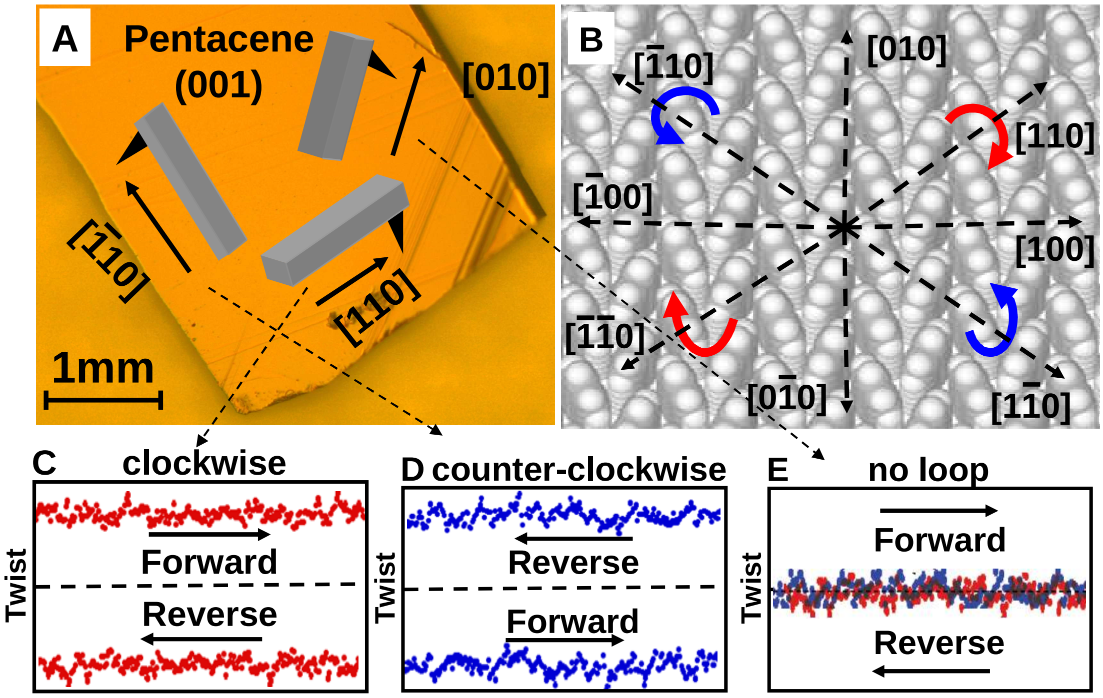

Figure 5.5 TSM signal (*i.e.*, the sign and magnitude of cantilever twisting) on Pentacene Single Crystal A) Optical image of an indexed pentacene crystal which was repositioned in the force microscope three times to measure the TSM response along distinct crystallographic directions. B) Molecular packing in the a-b plane of a pentacene single crystal, which is analogous to the known packing in a pentacene monolayer on SiO$_2$. The curved arrows show the clockwise or counter-clockwise sense of the cantilever twisting when scanning along different crystallographic directions. C) A clockwise hysteresis loop (twist signal versus tip position) is obtained when the forward scan direction is along [110]. D) A counter-clockwise hysteresis loop is obtained when the forward scan direction is along $[1\bar{1}0]$. E) No hysteresis loop is obtained when the tip scans along either [100] or [010].

recording TSM hysteresis loops along different directions. Along $[110]$ or $[\bar{1}\bar{1}0]$ directions (they are antiparallel and equivalent), the hysteresis loops will be clockwise and maximized. Along $[\bar{1}10]$ or $[1\bar{1}0]$ (also equivalent), the hysteresis loops will also be maximized but they will be counter-clockwise. Once these two directions are established, determination of the other directions is straightforward either by additional TSM measurements to locate the "zero signal" directions ($[100]$ and $[010]$) where the hysteresis loops collapse, or by prior knowledge of the crystal structure. This biased twisting of the cantilever can be used to assign the $[110]$ direction in each grain of a polycrystalline pentacene film, a fact that we exploited to produce Grain Orientation Maps of these polycrystalline films.

5.2.5 Elastic Anisotropy

The question of the physical origin of the TSM signal remains. We hypothesized that transverse shear arises from anisotropy in the elastic properties of the crystal. Indeed, tensile testing on anthracene crystals has already established that the elastic modulus is a tensor quantity in oligoacenes,[154] and elastic anisotropy within the (001) plane of pentacene is expected based on the inherent anisotropy in intermolecular bonding.[36] Anisotropy in the measured carrier mobility, for example, is an accepted manifestation of anisotropy in pentacene intermolecular bonding.[155,156] Anisotropic molecular responses in organic crystals by nanoindenting and nanoscratching have also been reported.[157]

A simple mechanical model demonstrates that any elastically anisotropic medium will generate non-zero shear stress on a probe tip transverse to its scanning direction, provided the scanning direction is not along a symmetrical axis (see Appendix B). This model does not take into account the stick-slip behavior associated with real sliding contacts, nor any dissipative (frictional) processes; it only accounts for stresses associated with elastic deformation. Nevertheless, it supports our conclusion that any elastically anisotropic surface can generate a transverse shear force.

To test these ideas experimentally, we carried out pinned-contact shear modulation measurements[158,159,160,161] on monolayer films. In these experiments, the lateral position of the cantilever is dynamically modulated by an amount that is below the onset of measurable tip sliding, as determined from Fourier analysis of the response. The cantilever, at a controlled normal load, is wiggled in a direction *perpendicular* to the cantilever axis with a sinusoidal input to the appropriate transducer, and the lateral deflection response is recorded. In the purely static regime, that is when there is no slipping of the probe tip, the lateral deflection provides a measure of the shear stiffness of the sample. Our goal was to determine whether we could detect stiffness anisotropy by shear modulation in different grains of a polycrystalline monolayer film. As different grains are oriented with respect to each other, wiggling the cantilever in a given direction would measure the stiffness along different crystallographic directions in separate grains. Indeed, different lateral deflection amplitudes for shear modulation in two different grains in a monolayer film confirmed the presence of significant elastic anisotropy. Figure 6 clearly shows that the average lateral cantilever response in a bright grain is different from that of a darker grain.

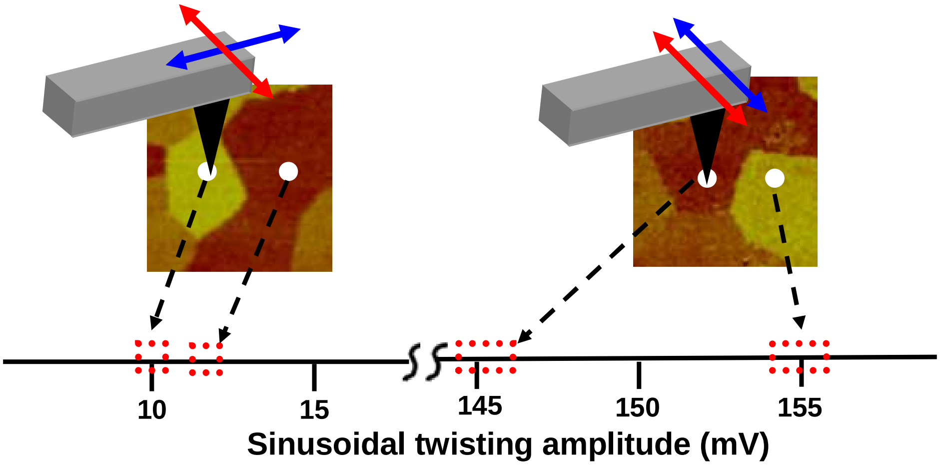

Figure 5.6 Pinned Contact Shear Modulation Experiment In a shear modulation experiment the lateral position of the cantilever is dynamically modulated by an amount that is below the onset of measurable sliding, and the resultant cantilever twist is measured. In all the figures the blue double-head arrows represent the input sinusoidal motion and the red double-head arrows shows the sinusoidal twisting response of the cantilever. The amplitude of cantilever lateral twist varies from one grain to another on a pentacene monolayer, when the wiggling direction is parallel to the axis of the cantilever or perpendicular to the axis of the cantilever. However, the magnitude of the lateral response is ~ 10 times smaller when the cantilever is wiggled along the axis of cantilever.

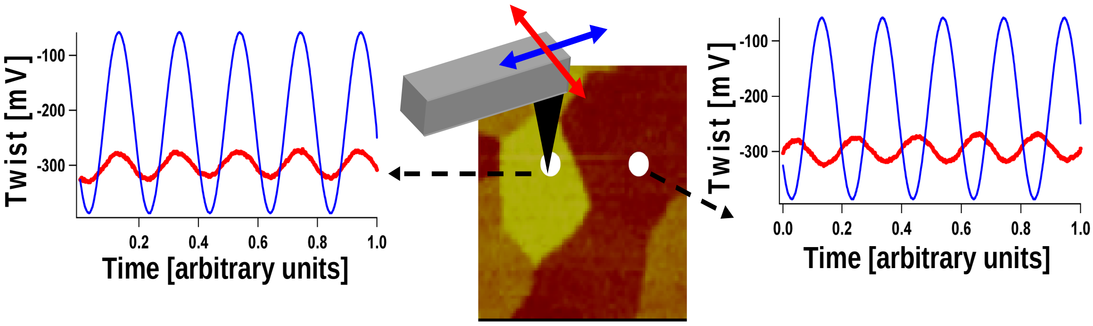

Figure 5.7 Pinned Contact TSM Modulation Experiment. A “wiggling” or point contact shear modulation experiment confirms the sensitivity of TSM to both grain orientation and anisotropic elastic response. With the tip fixed at a point on a bright pentacene grain (*i.e.*, a grain showing large TSM signal in an image), wiggling the cantilever/tip assembly in a direction parallel to the cantilever axis (blue arrow) results in an in-phase (clockwise) cantilever twisting response. On a dark grain, the same wiggling experiment gives an out-of-phase (counter-clockwise) twisting response.

To probe the origin of the transverse shear response, we changed the shear modulation direction to be *parallel* with the cantilever axis and repeated the pinned-contact shear modulation experiment on two high contrast grains in a monolayer film. The amplitude of cantilever lateral twist varies from one grain to another on a pentacene monolayer, even when the wiggling direction is parallel to the axis of the cantilever (as shown in Fig. 5.7). However, the magnitude of the lateral response is ~ 10 times smaller when the cantilever is wiggled along the axis of cantilever, as compared to wiggling perpendicular to the cantilever axis. Along with measuring the sinusoidal cantilever lateral response, we also recorded the phase lag between the input sinusoidal motion and the lateral twisting response, depicted in Fig. 5.7. Shear modulation on the bright grain produced a TSM signal in-phase with the modulation input signal, whereas on the adjacent dark grain the same experiment produced a TSM response exactly out of phase with the input motion. The TSM response on both grains in a pinned-contact experiment is strong evidence that the origin of transverse shear is related to elastic anisotropy of the grains. In addition, the phase difference between the input sinusoidal motion and the resultant transverse shear signal for the dark grain is expected, *i.e.*, an in-phase TSM signal corresponds to a clockwise twisting and an out-of-phase signal corresponds to counter-clockwise twisting.

In conjunction with our mechanical model (see Appendix B), these results support the conclusion that elastic anisotropy is a principal contribution to contrast in TSM images and thus the technique is generally applicable to elastically anisotropic solids. The data in Figure 5.5 suggest why the TSM method has not been broadly recognized. On pentacene crystals, the TSM signal is nearly a factor of 10 smaller than the conventional FFM signal. Because the TSM signal is likely to be small for many materials, any inherent surface topography that produces cantilever torsion will obscure the contribution to transverse shear arising from elastic deformation processes. Additionally, it is notable that low modulus, compliant materials are more likely to yield measurable TSM signals than stiff materials. This is because the torque on the cantilever is proportional to the shear strain induced under the tip (Appendix A); materials with small tip-induced strain will generally have smaller torque, especially if the elastic anisotropy is not very large. For these reasons, the very flat and relatively soft organic semiconductor films that we describe here are ideal samples for TSM.

5.2.6 Grain Orientation Maps

With an understanding of TSM contrast in hand, we have used the technique to analyze the microstructure of pentacene monolayer films in detail. Figure 5.8A shows a TSM image of a coalesced pentacene monolayer in which the $[110]$ direction has been labeled on each individual grain, producing a Grain Orientation Map. Grain orientation mapping is possible based on the contrast mechanism. For example, the darkest grains in Figure 5.8A yield counter-clockwise hysteresis loops on forward and reverse scans, meaning the scan vector is aligned along $[1\bar{1}0]$. The bright grains correspond to clockwise loops with the scan vector along $[110]$. Grains that have intermediate contrast correspond to alignment of the scan vector between $[1\bar{1}0]$ and $[110]$. We used simple linear interpolation of the color scale to estimate the $[110]$ direction, Figure 5.8A.

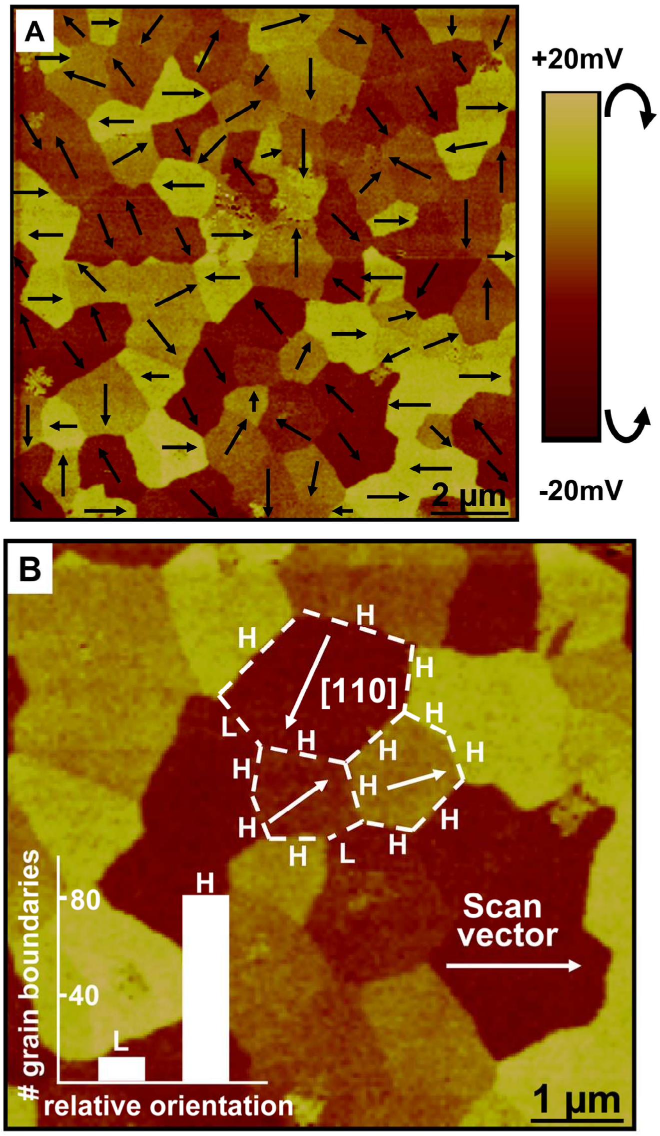

Figure 5.8 Grain Orientation Map and Grain Boundary Analysis. A) A TSM-generated Grain Orientation Map, where the arrows indicate the [110] direction in each grain. The bright contrast corresponds to clockwise cantilever twisting, while the dark contrast corresponds to counter-clockwise cantilever twisting. B) TSM image showing high (H) and low (L) angle grain boundaries. The histogram indicates that ~ 90% of the grain boundaries present in the polycrystalline first monolayer of pentacene on SiO_2 are high angle.

An important benefit of Grain Orientation Maps is that they allow determination of the relative population of high and low angle grain boundaries (GBs), Figure 5.8B. Several groups have reported evidence that GBs are responsible for charge trapping and lower charge mobilities in OTFTs.[162,163] The ability to quantify the density and orientation of grain-grain contacts therefore opens up interesting possibilities for probing the connection between transport and microstructure in detail. Conventionally, a GB is low angle if the relative orientation between adjacent grains is less than 15°, otherwise it is referred to as high angle.[164] Figure 5.8B shows a magnified TSM image in which high angle (H) and low angle (L) GBs have been identified by calculating the angle between [110] directions in adjacent grains. Analysis of 15 grains (~ 90 GBs) picked at random indicates that approximately 90% of GBs visible in the TSM images are high angle, as indicted by the inset to Figure 5.8B.

5.2.7 Grain Shape and Size

Grain Orientation Maps also clearly reveal the shape and size of pentacene grains, Figure 5.9. Analysis of several hundred grains reveals that a large majority (~ 80%) have six faces, Figure 5.9A. This hexagonal shape can be rationalized by a Wulff construction, Figure 5.9B, which predicts grain shape based on surface energy anisotropy.[165] To make the Wulff analysis, we utilized the face-specific surface energies (γ) for pentacene calculated by Verlaak *et al.*[166] ($\gamma(100)$= 76.8 mJ/m^2, $\gamma(010)$= 100.8 mJ/m^2, $\gamma(110)$= 83.2 mJ/m^2 and $\gamma(\bar{1}10)$ = 80 mJ/m^2) and the known thin film phase lattice parameters.[18] The construction suggests two types of angles between different faces of a single grain, four

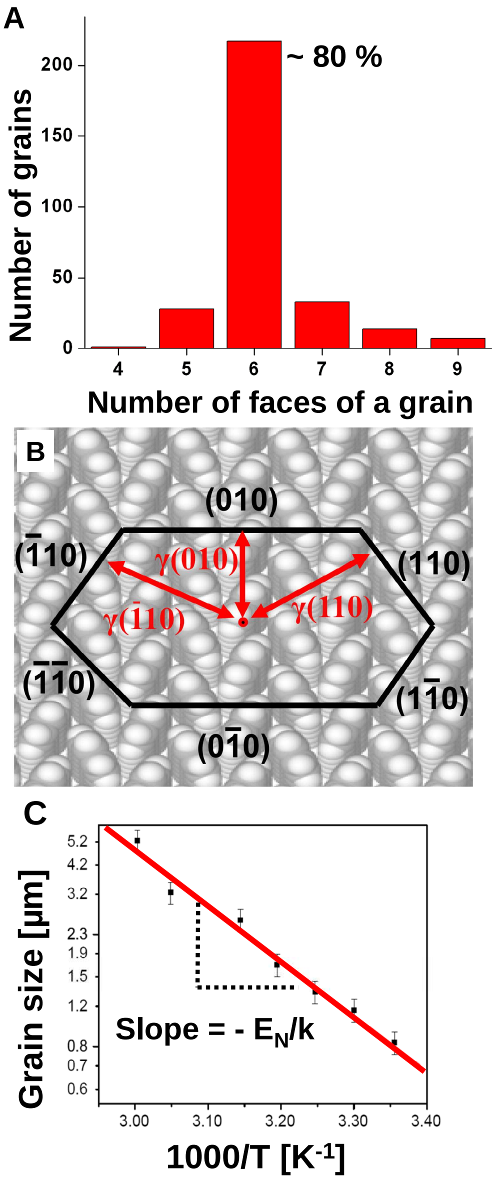

Figure 5.9 Grain Shape and Size A) Histogram indicating that about 80% of the grains visible in TSM images of a pentacene monolayer are six-sided. B) A Wulff construction for a pentacene monolayer confirming that faceted, six-sided grains are expected based on surface energy anisotropy. C) Semi-logarithmic plot of TSM-determined grain size (an effective radius) versus substrate temperature for pentacene monolayers grown on SiO_2. The straight line shows the Arrhenius variation of grain size with substrate temperature. The slope of the line corresponds to $-E_N/2k$, where E_N is the activation energy of nucleation and k is the Boltzmann constant.

of approximately 128° and two of approximately 105°. The measured angles from the TSM images of forty of such six-sided grains confirm two sets of angles between different faces of a grain: (137°± 3°, 133° ± 5°, 127° ± 5°, and 121° ± 5°) and (106° ± 7° and 98° ± 7°). We conclude that under the growth conditions we employed, the pentacene grains in the first monolayer have adopted largely equilibrium grain shapes with faceting dictated by surface energies.

To determine the kinetics of grain growth, pentacene monolayers were grown on SiO_2 at different substrate temperatures at a constant deposition rate of ~ 0.01 Å/sec. Figure 9C is an Arrhenius plot of the grain size (an effective radius) versus the substrate temperature (T). It is evident that the grain growth is thermally activated and the straight line fit provides the activation energy of nucleation (E_N ~ 800 meV) for pentacene crystallites on SiO_2. This nucleation energy in turn can be used in conjunction with conventional diffusion-limited growth models to estimate the activation energy for diffusion.[48] We calculate the activation energy of diffusion (E_D) of pentacene on SiO_2 to be ~ 1 eV (see Appendix C), which to our knowledge has not been determined previously.

5.3 Conclusion

We have demonstrated that TSM, with its sensitivity to grain orientation, is a powerful approach to probe the microstructure of ultra-thin crystalline organic films. The mechanism of TSM contrast relies on mechanical properties of the material, specifically the in-plane elastic anisotropy, and thus TSM will be useful for visualizing microstructure in any suitably smooth, elastically compliant, and anisotropic crystalline film. We have demonstrated specifically that grain orientation mapping by TSM can be employed to quantify grain morphology, grain boundary density and the relative proportion of high-angle grain boundaries in ultra-thin organic semiconductor monolayers grown on common dielectrics. Collectively, these findings establish TSM as a promising new method for quantitative characterization of microstructure in crystalline soft materials.

5.4 Experimental

Thin film and single crystal growth

Monolayers of pentacene and other organic semiconductors were grown by thermal evaporation of the corresponding source material onto insulating substrates under vacuum pressure of ~ 6×10^{-7} Torr and deposition rates of ~ 0.01 Å/sec. The majority of the monolayers were grown on p-doped silicon wafers, with thermally grown 300 nm thick amorphous silicon dioxide overlayer. High purity pentacene source material (~ 99.8%) was purified by repeated sublimations before it was used to grow films. All the TSM images and analysis were based on freshly grown pentacene monolayers and single crystals.

Transverse Shear Microscopy

All TSM images were taken on a Veeco Nanoscope IIIA multimode atomic force microscope under ambient conditions. The probes used for AFM measurements were silicon nitride V-shaped cantilevers with integrated contact mode tips fabricated by Veeco Metrology, USA (Model DNP and force constant ~ 0.58 N/m). The TSM signal is very sensitive to the tip contamination, so the tips were cleaned with DI water, ethyl alcohol and acetone before imaging. The images were obtained at a nominal load of ~ 3 nN. The scan rate used for a (10µm X 10µm) image size was 1.5 Hertz. All the TSM images were taken at low relative humidity (~ 20%), and it was observed that at higher humidity levels the TSM contrast was less prominent.

Pinned Contact Shear Modulation

The pinned contact shear modulation experiments were performed on a Molecular Imaging PicoPlus SPM (now Agilent 5500) with a PicoScan 3000 controller, and environment control. This is a tip scanned system. Humidity was kept below 10%. A Hewlett Packard 33220A Function/Arbitrary waveform generator and a BNC breakout box were used to input and measure the sinusoidal motion given to the cantilever. An extra imaging channel was used to collect these data in synchronization with the response signals to quantify the phase shift and the data were collected at low driving frequencies such that extraneous phase shifts, *e.g.*, capacitive, are negligible. The amplitude and frequency of the input sinusoidal motion were ~ 1 nm and 30 Hz, respectively. Amplitudes above ~ 3 nm produced detectable sliding as determined by the presence of odd harmonics in Fourier analysis,[167] but to find the exact amplitude (between 1 nm and 3 nm) where the stick-slip transition takes place is part of ongoing research. The integral and proportional gains during the wiggling experiments were intentionally kept very low (~ 1 in the Molecular Imaging software) to reduce z motion of the tip.

For all the modulation experiments a 1D scan was taken by zeroing the scan size along the fast scan axis (*i.e.*, the scan axis perpendicular to the principal axis of the cantilever in case of conventional shear modulation and parallel to the principal axis of the cantilever in case of TSM modulation), to separate the imposed sinusoidal motion from monotonic scan motion. During the modulation experiments on monolayers, first a 2D TSM image was taken with no modulation and then a 1D modulated scan was taken along the center of the image, in order to correlate the average lateral amplitude to the grain contrast. Immediately after the 1D scan, a 2D TSM image was again taken without modulation to confirm the absence of plastic deformation of the film. Shear modulation data were analyzed by taking the 0D scans (point scans) of a 1D image (*i.e.*, a plot of lateral amplitude vs. time) to compare the relative lateral responses along different contrast grains in monolayer pentacene films. The software package IGOR (Wavemetrics, Inc.) was used to calculate the amplitude and the phase of a lateral response. Fast Fourier Transform plots were also analyzed for the point scans to verify the no-slip condition.

X-Ray Diffraction

A Bruker SMART 1000 CCD diffractometer was used to map crystallographic directions and planes in a pentacene single crystal.

Photodetector Non-Orthogonality

Photodetector non-orthogonality (coupling between lateral and vertical cantilever deflection) can be a critical factor in TSM because of the relatively small magnitude of the twist signal. Figure 5.5E (main text) shows that the TSM loops collapse when the tip scans along [100] or [010] directions and thus indirectly addresses this question of non-orthogonality. To further probe this issue, TSM was performed on amorphous SiO_2

samples and zero signal was observed independent of the scanning direction. This result indicates negligible optical crosstalk (*i.e.*, the laser spot displacements for lateral vs. normal forces are indeed parallel to the intended photodetector axes) and that the tip/cantilever assembly is not defective (*i.e.*, the tip is centered on the end of the cantilever).[88,168] This finding also backs our conclusion that elastic anisotropy is the origin of TSM signal as we obtain zero TSM signal on amorphous and isotropic materials.

Grain size

Figure 5.10 shows the TSM images of pentacene monolayer films on SiO_2 at different substrate temperatures but at same deposition rate (.01Å/sec). An expected increase in the grain size with increasing the substrate temperature is observed. The TSM image corresponding to the pentacene monolayer film grown at 65^0C shows no surface coverage of SiO_2 by pentacene molecules. This indicates considerable desorption of pentacene molecules from the substrate at 65^0C. Increasing the substrate temperature decreases the nucleation density and thus the average grain size increases. Grain size measurement is done with the help of the grid method as explained below.

After marking the grain boundaries in a TSM image, a transparent square grid is placed on top of the image, as shown in Fig. 5.11. Then the grain size is calculated by counting the number of squares each grain occupies. For each temperature around 50 grains are measured and the mean and standard deviation of grain size are obtained. Calculated mean area is then equated to the area of the circle to get the grain size (d_{eff}), using equation:

$$Mean.Area = \frac{\pi}{4} \times \left(d_{eff}\right)^2$$

The calculated grain size (d_{eff}) is plotted against the inverse substrate temperature in a semilog axis (Fig. 5.9C). All the points fit well in the linear curve showing activated Arrhenius dependence of grain size. Slope of the plot represents activation energy for nucleation (E_{Nucl}) and is ~ 421 meV.

Wulff Construction

Wulff's construction predicts grain shapes based on the surfaces energies. The surface energies of liquids and gases are isotropic, so the lowest energy form is the spherical shape which corresponds to minimum surface area. However in crystals, the surface free energies are anisotropic and consequently the equilibrium shape is not spherical. The equilibrium crystal shape can be determined by Gibbs-Wulff theorem. The theorem says that all the faces of the crystal in equilibrium should follow the rule:

$$\gamma_1 / h_1 = \text{constant}$$

where γ_1 = surface energy of the face (= γ (hkl))

and h_1 = the perpendicular distance from the centre of the crystal to this surface

The Wulff construction involves drawing vectors from a reference point corresponding to different crystallographic directions. For each vector, an intersecting plane (with same Miller indices as the vector) is drawn such that the angle between the vector and the intersecting plane represents the true angle between them (*e.g.*, it will be always 90° in case of cubic packing). The distance between the reference point and the point of intersection represents the magnitude of the surface energy associated with intersecting plane. After all the planes are drawn on different vectors, the equilibrium shape is given by the innermost envelope of the intersecting planes.[165] The following reported surface energy values were used to construct the Wulff diagram for pentacene monolayer grain:

Crystallographic plane	Surface energy (meV/ (Å)^2)
σ_{100}	4.8
σ_{010}	6.3
σ_{001}	3.2
σ_{110}	5.2
σ_{1-10}	5.0

Table 5.1 Anisotropic Surface Energies for Pentacene

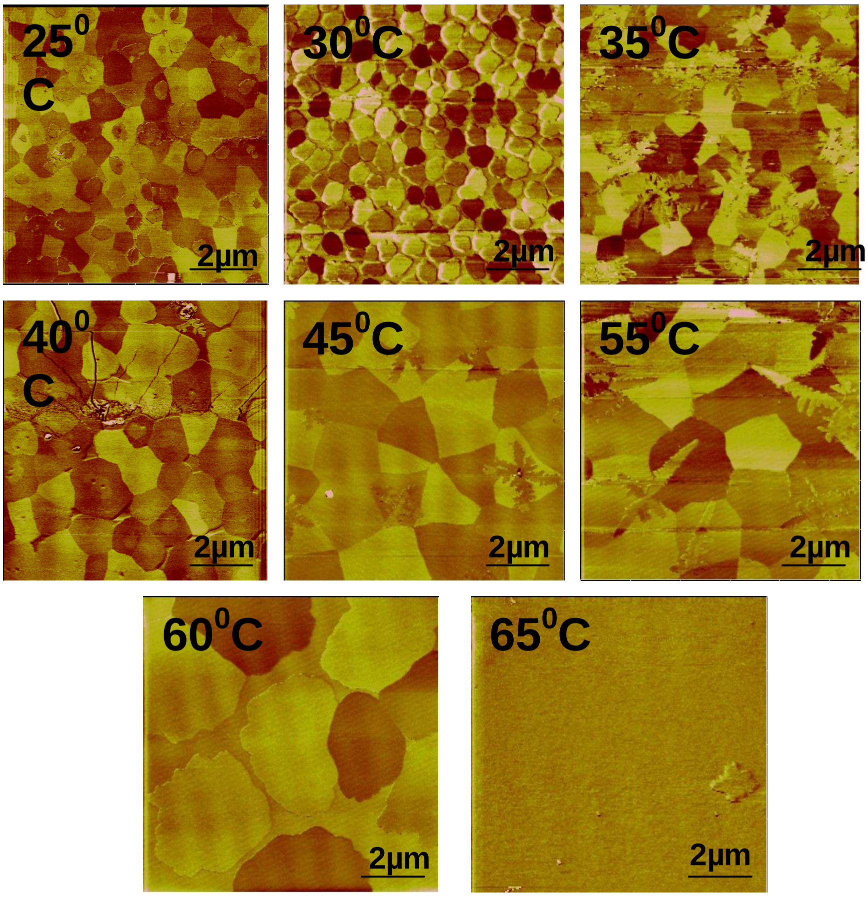

Figure 5.10 Pentacene Monolayer Grain Size as a Function of Substrate Temperature

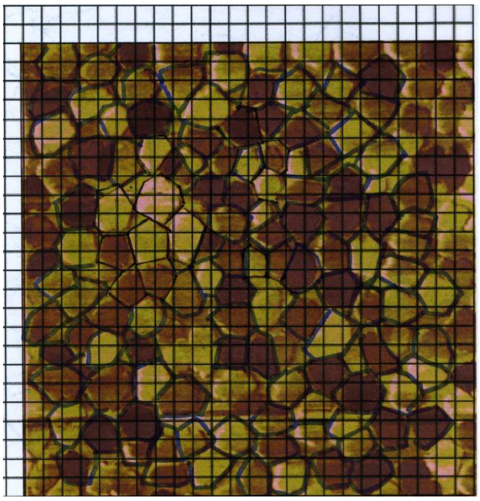

Figure 5.11 Grid Method to Calculate Grain Size

5.5 Acknowledgements

The authors thank Y. Liang and Y. Xia for useful discussion and some technical support. The authors would also like to thank Victor Young for help in the XRD measurements. This work was supported primarily by the University of Minnesota Materials Research Science and Engineering Center, funded by the NSF (DMR-0212302), and also partly through DMR-0706011. Parts of this work were carried out in the Institute of Technology Characterization Facility, University of Minnesota, which receives partial support from NSF through the NNIN program.

Chapter 6

Homo-epitaxial Studies of Ultrathin Pentacene Films and Correlation with Surface Electrostatic Potential

(Contributing Authors: Vivek Kalihari, D. J. Ellison, Greg Haugstad, C. Daniel Frisbie)
(Reprinted with permission from “Observation of Unusual Homoepitaxy in Ultrathin
Pentacene Thin Films and Correlation with Surface Electrostatic Potential”,
Advanced Materials 21 (2009))

Identifying specific microstructure-property relationships in polycrystalline organic semiconductor films is a key goal for the field of organic electronics. Using transverse shear microscopy, we have established for the first time the presence of both epitaxial and non-epitaxial domains in ultrathin polycrystalline layers of pentacene grown on SiO_2. The microstructure of pentacene films is particularly important, as pentacene is a benchmark semiconductor for organic field effect transistors (OFETs). Epitaxial domains in the second pentacene molecular layer exhibit unusual type-II coincidence with respect to the first pentacene monolayer, while the third and subsequent layers show commensurism with their respective underlayers. In addition, Kelvin probe force microscopy reveals that the epitaxial domains have significantly more positive surface potential than the non-epitaxial domains. Collectively, these findings establish a previously unrecognized link between epitaxial order in organic semiconductor films and a well-defined electrical property, the surface potential, which is known to influence charge carrier transport parallel to the pentacene/SiO_2 interface in OFETs.

6.1 Introduction

Recent developments in the field of organic electronics have generated widespread interest in identifying structure-property relationships for molecular films that form the active layers in devices such as OFETs,[9,10,11,12,13] organic light emitting diodes,[17] organic memories,[169] and organic solar cells.[16] It is generally appreciated that film microstructure is critically important to the performance of organic semiconductors in devices and there are good examples in the literature in which clear structure-property correlations have been made.[6,7,170,171,172,173] However, for all classes of organic semiconductors there remain significant open questions concerning the precise influences of microstructure on electrical performance. In the case of polycrystalline films, for example, the basic role of grain size on field effect mobility is still not conclusively established, with some reports describing a significant decrease in carrier mobility with smaller grain sizes,[151,174] and others reporting no significant dependence.[28,175,176] Much of the confusion in the literature likely results from differences in the specifics of experiments done in separate laboratories (e.g., substrate pretreatments). Still, the essential point is that fundamental understanding of microstructure-property relationships for organic semiconductors is only just emerging, and much better comprehension is highly desirable for the continued improvement of organic devices.

In this chapter, we describe a detailed scanning probe microscopy investigation of microstructure and properties for the first few crystalline molecular layers of the benchmark organic semiconductor pentacene ($C_{22}H_{14}$, Figure 6.1A) vapor deposited onto amorphous SiO_2 substrates. The pentacene/SiO_2 system is a model crystalline organic semiconductor/insulator interface that is widely studied[177,178,179,180] and used in OFETs,[123,124,153,181] and thus insights into the structure and properties of this interface have the potential to impact understanding of OFET operation. Furthermore, we believe that findings on this model interface can generally be taken as a qualitative guide for the types of issues that are at play in other crystalline organic semiconductor/insulator systems.

We describe two major findings in this chapter. First, we have observed a type of thin film homo-epitaxial growth in pentacene layers that has not been reported previously for pentacene or for any other molecular system. Using transverse shear microscopy (TSM),[32] we show that crystalline, vapor deposited films of pentacene on SiO_2 substrates have a specific orientation between the pentacene layers. The second pentacene layer exhibits an unusual coincidence-II type epitaxy on the first layer, while the third and subsequent layers show commensurism with their underlayers. We propose a 4 X 4 supercell structure for the pentacene second layer on the first layer, as deduced from the elements of the transformation matrix that defines the orientation between overlayer and underlayer. Our second finding is that a given pentacene overlayer has both epitaxial and non-epitaxial domains that manifest themselves in surface electrostatic potential differences. The one-to-one correspondence between epitaxy and surface electrostatic potential illustrates that strong coupling between microstructure and electrical properties is inherent to molecular thin films, and it provides a critical, but so far unrecognized, link between structure and electrical transport behavior at pentacene/SiO_2 interface.

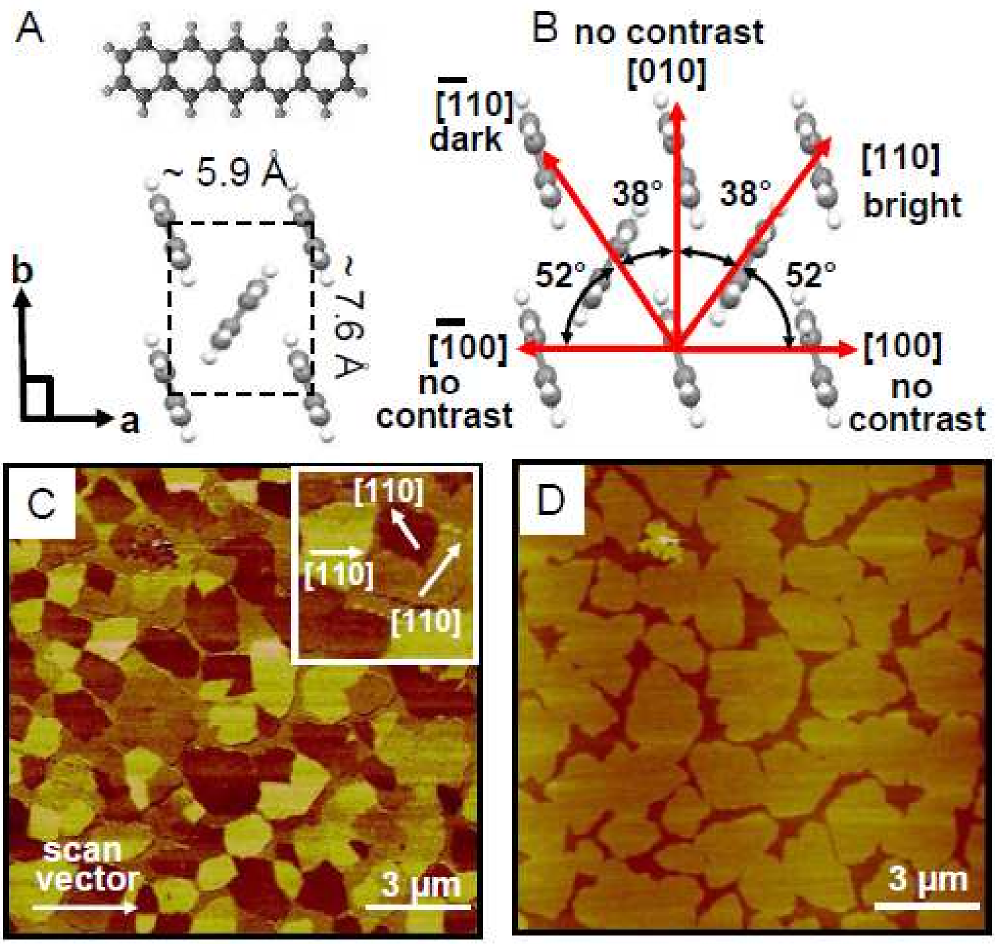

Figure 6.1 TSM Signal Dependence on Pentacene Crystallographic Orientation A) Pentacene molecular structure and monolayer unit cell in the (001) plane[18]: a = 5.9 Å, b = 7.6 Å, and γ = 90°. B) Pentacene herringbone molecular arrangement (along with important angles between the principal axes and the two diagonals) and the TSM signal as a function of different crystallographic directions in the **a**-**b** plane.[32] C) TSM image reveals striking contrast in the first pentacene monolayer highlighting different grains. Inset shows grain orientations based on the TSM signal.D) Corresponding topography (height) image shows a partly coalesced first pentacene monolayer, but does not reveal crystallographic orientation.

6.2 Results and Discussion

In our previous reports,[30,32] we have demonstrated that TSM produces striking images of grain size, shape, and crystallographic orientation in single monolayers of pentacene on SiO_2. The TSM signal depends on the relative orientation between a pentacene crystallite and the cantilever scan vector in the (001) plane of a pentacene film, as shown in Fig. 6.1B. The angular dependence of the TSM signal produces high contrast images of grain shapes (Fig. 6.1C) that are not evident in simultaneously acquired topography images (Fig. 6.1D). TSM images are quantitatively interpreted as grain orientation maps; the inset to Fig. 6.1C shows the assignment of different crystallographic directions to individual grains based on their TSM signals. The TSM generated grain orientation map in Fig. 6.1C is remarkable in the degree of microstructural information it provides; analysis of such images is key to our current work.

6.2.1 TSM of Pentacene Second Layer

Figures 6.2A and 6.2B display topography and TSM images of the same region of a two layer (~ 3 nm) thick pentacene film on SiO_2. The topography image reveals a nearly featureless coalesced first monolayer with a few cross-shaped second layer islands (bright). The TSM image indicates different signal levels for each of the cross-shaped islands I-III, reflecting their different crystallographic orientations with respect to the cantilever scan vector. These cross-shaped islands have a general shape composed of two principal axes: a long axis and a perpendicular short axis, reflecting anisotropic growth.

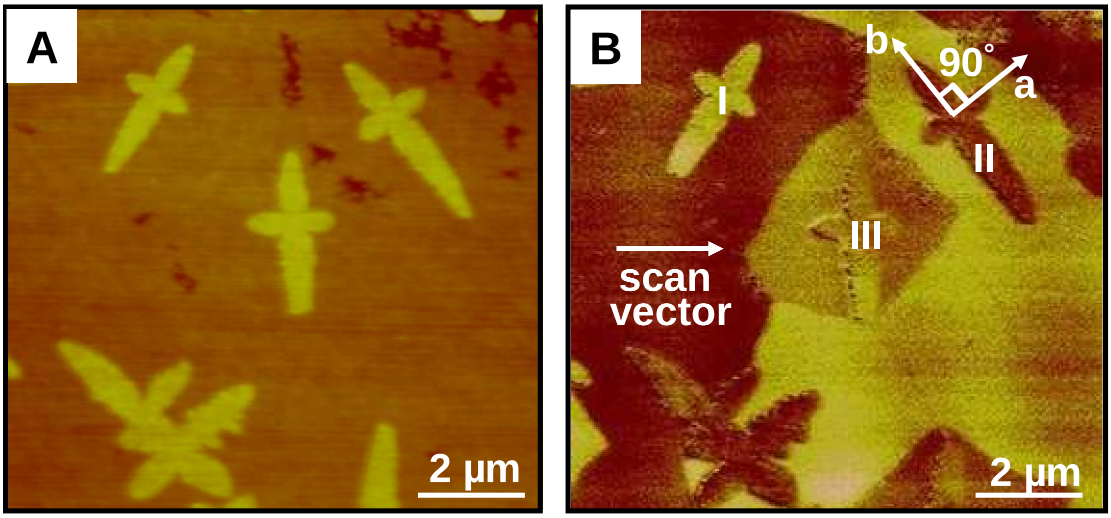

Figure 6.2 TSM of Pentacene Second Layer A) Topography image shows a fully coalesced first monolayer and a few cross-shape second layer islands. B) TSM image reveals different signals for each of the second layer islands, indicating their different crystallographic orientations with respect to the cantilever scan vector. The TSM signal of the cross-shape second layer crystallites establishes that the long arm is aligned with the **b** [010] axis and the perpendicular short arm corresponds to the **a** [100] axis. It is observed that a bright second layer I grows on top of dark first layer and a dark second layer II grows on top of bright first layer, indicating absence of commensurism. However, second layer III crystallite appears to be commensurate with the underlayer.

The TSM signal of second layer crystallites establishes that the long arm of the island is aligned with the **b** direction [010] of the crystal and the short axis corresponds to the **a** direction [100]. Analysis of hundreds of second layer islands revealed the same characteristic cross-shape, verifying that these shapes are typical. Similar anisotropic growth of pentacene thin films on crystalline Si has also been reported, measured by low-energy electron diffraction (LEED) and low-energy electron microscopy (LEEM) techniques.[24]

Importantly, the TSM image in Fig. 6.2B reveals that there is strong contrast between the second layer crystallites I and II and the underlying first monolayer, indicating the absence of commensurate epitaxy. If there had been a commensurate epitaxial relationship, the TSM signal from the overlayer and the underlayer would be identical. However, in Fig. 6.2B it can be seen that the bright second layer island I grew on a dark grain underneath; likewise, the dark second layer island II grew on a bright grain underneath. This TSM contrast rules out the possibility of commensurate epitaxy for islands I and II. The situation for island III appears to be different as this island has the same TSM signal as the underlayer. Specifically, it appears that the island III is commensurate with the underlayer. These are general and reproducible observations; we have observed both the presence and absence of commensurism for the pentacene second layer islands on the first layer.

To quantitatively analyze the contrast between the second and the first layer, we have assigned the **b** axes [010] associated with the first ($\mathbf{b_1}$) and second layer ($\mathbf{b_2}$), based on their respective TSM signals; examples are shown in Figs. 6.3A and 6.3B. The angle

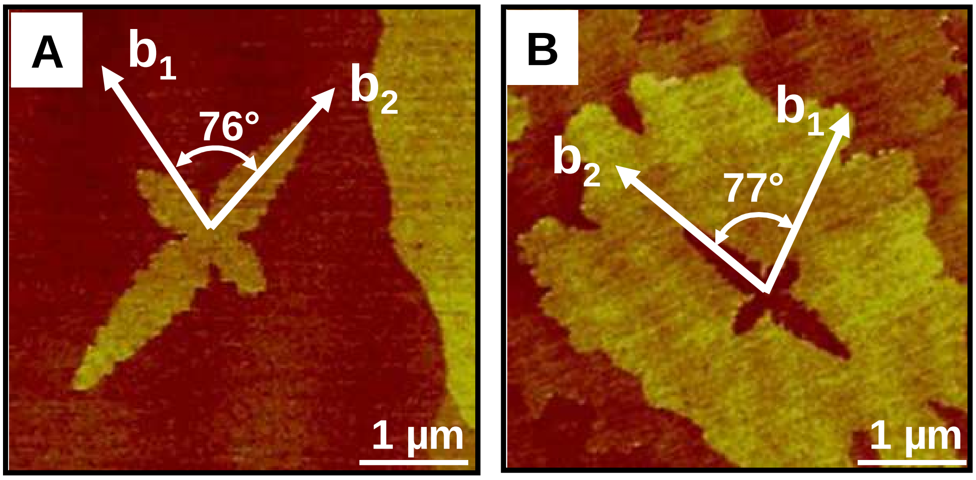

Figure 6.3 In-Plane Orientation between the Pentacene First and Second Layer A) Assignment of **b** axes [010] associated with the pentacene first ($\mathbf{b}_1$) and second layer ($\mathbf{b}_2$), based on their respective TSM signals. The angle between $\mathbf{b}_2$ and $\mathbf{b}_1$ defines the orientation between the second and the first layer. TSM image of a bright second layer crystallite on dark first layer indicating an orientation of 76° ± 5° between them. B) TSM image of a dark second layer crystallite on bright first layer indicating an orientation of 77° ± 5° between them.

between $\mathbf{b}_2$ and $\mathbf{b}_1$ defines the orientation between the second layer and the first layer. Figure 6.3A reveals an orientation of 76° ± 5° between the bright second layer and the dark first layer, while Fig. 6.3B shows an orientation of 77° ± 5° between the dark second layer and the bright first layer (an uncertainty of ± 5° denotes the 90% confidence limits in assigning crystallographic directions based on the TSM grey scale). The similar orientation between the layers suggests a defined non-commensurate homo-epitaxial relationship for the pentacene second layer on the first layer.

Indeed, a statistical analysis of the orientation between the second and the first layers taken from ~ 50 TSM images reveals a well-defined and preferred orientation, Fig. 6.4A. A large sharp peak in the Fig. 4A histogram at 77° verifies a non-commensurate organic homo-epitaxy. The small peak at 0° corresponds to second layer islands exhibiting commensurism with the first layer, but this peak constitutes less than 10 % of the total number of second layer islands examined. Films grown at different substrate temperatures reveal different relative proportions of commensurism. We have found that the percentage of commensurism decreases with increasing substrate temperature during the film growth. For example, the percentage of commensurism decreases from 10 % to 3 % when the substrate temperature increases from 35 °C to 50 °C. Similar behavior has been reported for Ag deposition on crystalline Si substrates, where different kinds of epitaxies exist, and their relative proportions are found to be strongly dependent on the substrate temperature.[182]

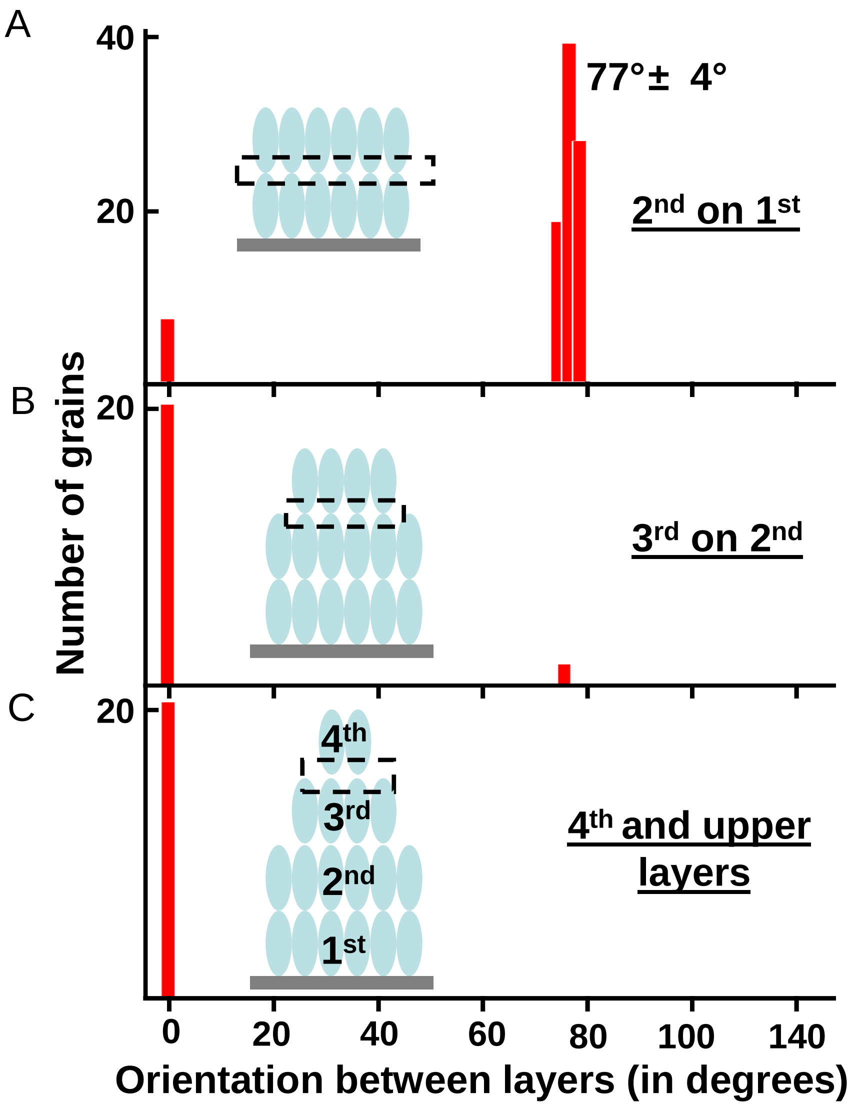

Figure 6.4 Orientation between different layers in pentacene films. Histograms showing orientations of A) Second layer crystallites on first layer: a large sharp peak at 77° indicates a non-commensurate, preferred homo-epitaxial order. A small peak at 0° corresponds to commensurate epitaxy. B) Third layer crystallites on second layer: a sharp large peak at 0° shows that the majority of the third layer exhibits commensurism with the second layer, with only a small proportion demonstrating a 76° orientation. C) Fourth and subsequent layer crystallites on their respective underlayers: a single peak at 0° reveals that all the layers grow commensurately on their underlayers.

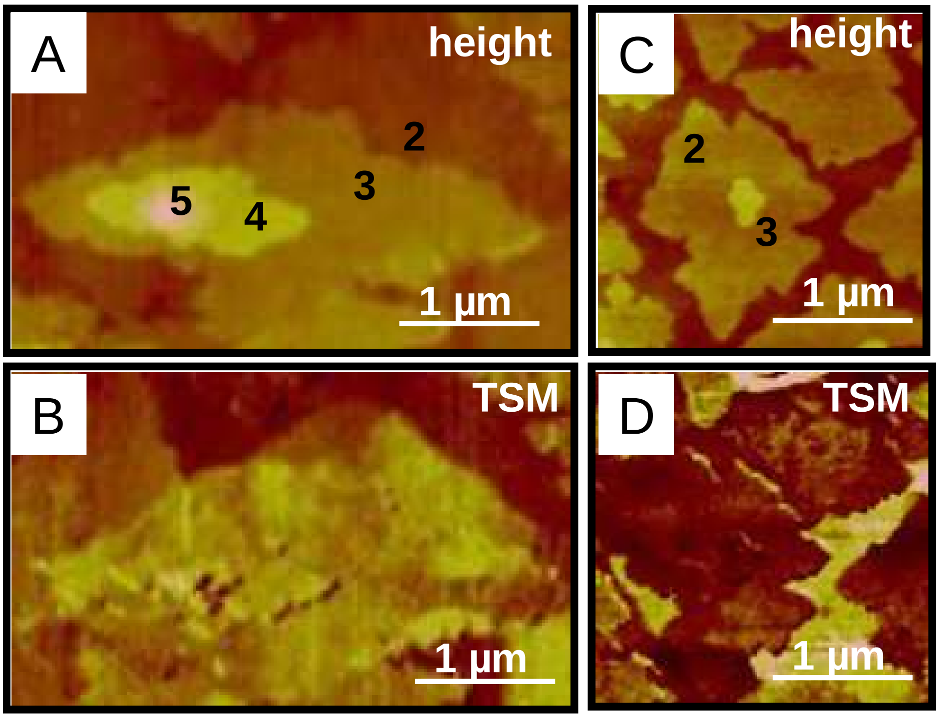

Figure 6.5 Commensurism between Second and Subsequent Layers A) Topography image shows islands of third, fourth, and fifth pentacene layer crystallites on top of fully coalesced second layer. B) TSM image reveals same signal (bright) for all the layers, indicating commensurism for the third and subsequent overlayers. C) Topography image shows a third layer on second layer. D) TSM image demonstrates similar TSM signal (dark) for both the layers indicating commensurism between them.

6.2.2 TSM of Third and Subsequent Layers

In order to investigate epitaxial relationships in subsequent layers, we grew thicker films of pentacene on SiO_2. The TSM studies of the thicker films show that the majority of the third layer islands grow with commensurate epitaxy with only a few exhibiting a preferred orientation of ~ 76° between the third and the second layer, as visible in Fig. 6.4B. The fourth and subsequent layers always display commensurism with their respective underlayers, as indicated by a single sharp peak at 0° in Fig. 6.4C (corresponding TSM images are shown in Fig. 6.5).

The change in the mode of epitaxy on transitioning from the second layer to the subsequent layers can perhaps be attributed to a large interfacial strain between the second and first layers.[183] For example, the first monolayer of pentacene on SiO_2 has a different structure than subsequent layers (molecules in the first layer are nearly perpendicular to the substrate while in thicker films the molecules tilt with respect to the substrate normal[18]) which is a result of differences in interlayer interactions, e.g. pentacene-SiO_2 versus pentacene-pentacene interactions. To accommodate the different first monolayer structure, the second layer grows with a preferred twist instead of the usual commensurism exhibited by the third and subsequent layers. This preferred twist can also be viewed as a stacking fault, as it disrupts the usual packing of (001) pentacene planes. Stacking faults are planar defects found commonly in bulk organic single crystals,[184,185,186,187] but as the preferred twist in this case takes place very near the pentacene/SiO_2 interface it may be more appropriately described as an interfacial reconstruction. Figure 6.6A shows a scheme of the pentacene growth in which the second

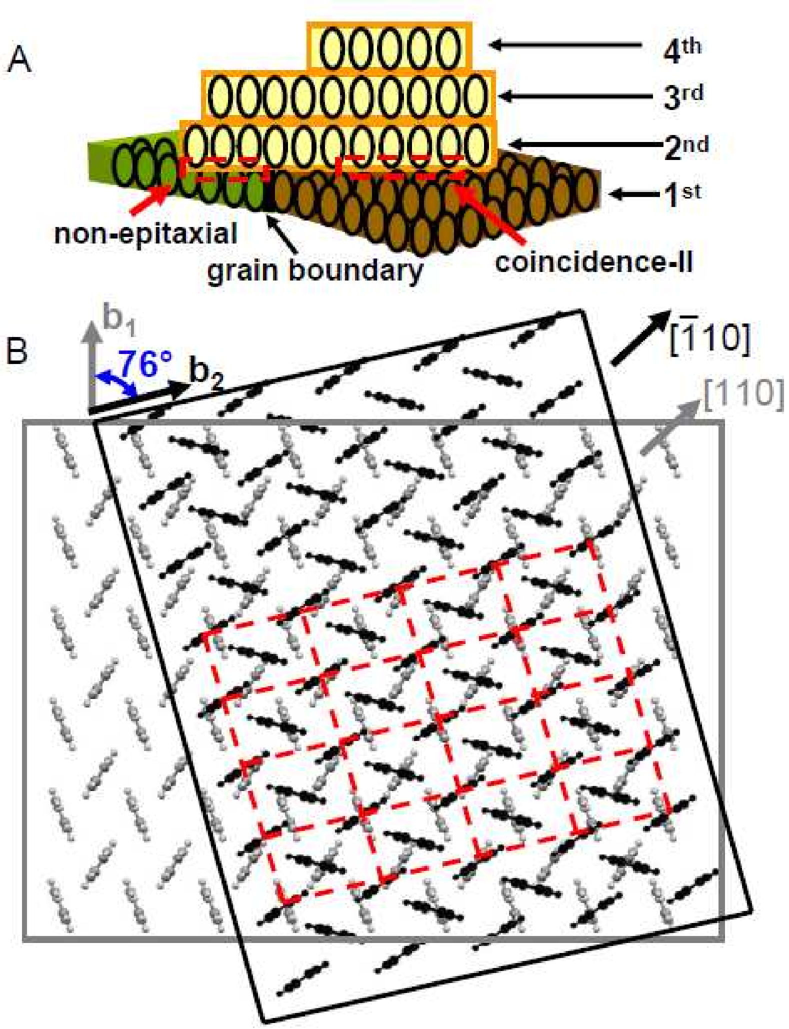

Figure 6.6 Pentacene Thin Film Growth and Coincidence-II Epitaxy A) Schematic showing that the pentacene second layer grows with a twist on the first layer, while the third and subsequent layers grow commensurately on their respective underlayers. B) Geometrical construction based on rotation of 76° of the pentacene second layer on the first layer in the **a-b** plane. The grey molecules correspond to the pentacene first monolayer, while the black molecules represent the second layer. The 76° orientation of the second layer results in coincidence-II epitaxy and a 4 X 4 supercell (as shown by dashed red lines). The figure also shows the alignment of two different unit cell diagonals, [110] and [$\bar{1}$10], in the two layers. This kind of epitaxy is also termed "geometrical coincidence".

layer is twisted with respect to the first and the subsequent layers are commensurate.

6.2.3 Coincidence-II Epitaxy

Understanding the cause of the second layer twist in detail will require further study, however the structural implications are easier to determine. The only crystallogra--phic angle close to the preferred orientation is the angle between the two unit cell diagonals, [110] and $[\bar{1}10]$, which is 76°. At the molecular level, the 76° orientation between the second and the first layer corresponds to the alignment of two diagonals, [110] and $[\bar{1}10]$. Thus, we propose that the pentacene second layer grows on the first layer such that the $[\bar{1}10]$ direction in the overlayer aligns with the [110] direction in the underlayer, and vice versa. Importantly, this hypothesis also supports the observed TSM contrast between the second and the first layer (bright on dark and dark on bright), as TSM produces opposite signals when scanning along the two different unit cell diagonals.[32]

These observations can be formalized in terms of the grammar of epitaxy.[188] The overlayer and the underlayer lattice vectors are related through a transformation matrix [C], where the matrix coefficients define the mode of epitaxy. Based on the 76° orientation between the second and the first layer, the published underlayer lattice parameters[18] (a_1 = 5.9 Å, b_1 = 7.6 Å, and α = 90°), and taking the overlayer parameters (a_2, b_2, and β) to be to first approximation the same as the underlayer lattice parameters,[189] the calculated transformation matrix is:

$$[C] = \begin{bmatrix} 0.25 & -0.75 \\ 1.25 & 0.25 \end{bmatrix}$$

All the matrix elements are rational and no column consists of integers, which indicates coincidence-II type epitaxy[188] between the second and the first layers of pentacene on SiO_2. To visualize the coincidence-II epitaxy, we geometrically rotated a model of the second layer of pentacene on the first, Fig. 6.6B. In this schematic, the grey pentacene molecules represent the first monolayer and the black pentacene molecules represent the second layer. The figure shows the alignment of two diagonals in the two layers ($[\bar{1}10]$ in the second layer aligns with [110] in the first layer) and a rotation of 76° between the layers. The coincidence-II construction in Fig. 6.6B also shows the formation of a 4 X 4 supercell (shown by dashed red lines) for the pentacene second layer on the first layer. It can be seen that there is precise registry of the second and first layer molecules at the corners of this supercell, as is characteristic of coincidence-II epitaxy. Final confirmation of the 4 X 4 supercell requires molecular resolution imaging. However, it is clear from the TSM data (Figs. 6.3 and 6.4) that coincidence epitaxy predominates for second layer growth on the first and that this mode changes to commensurism for subsequent layers.

The literature on thin film organic homo-epitaxy is remarkably sparse, perhaps because of the common belief that homo-systems (overlayer and underlayer consisting of the same molecules) always exhibit commensurism based on minimum energy arguments. Our finding of coincidence-II epitaxy between the pentacene second and first layers contradicts this general notion. The next challenge is to determine the implications of these structural features for the electrical properties of pentacene films.

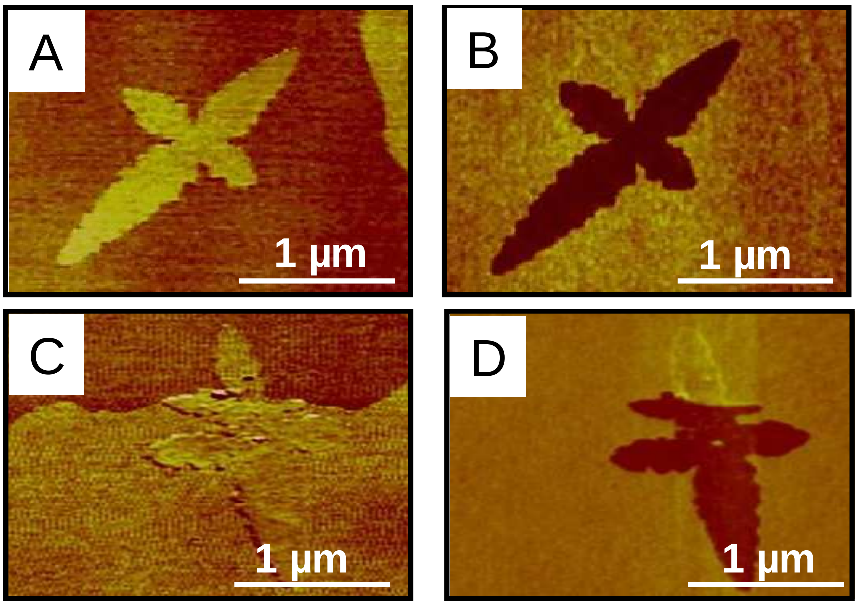

Figure 6.7 Friction Dependence on Epitaxy A) TSM image shows coincidence-II epitaxy for a second layer island, i.e., a bright second layer on top of dark first layer. B) FFM image reveals low friction for the epitaxial second layer. C) TSM image of a second layer island which interacts both epitaxially (intermediate signal second layer on intermediate signal first layer) and non-epitaxially (intermediate signal second layer on dark first layer) with the underlayer. D) FFM image displays lower (darker) friction for the epitaxial region and higher (bright) friction for the non-epitaxial region, suggesting more energy dissipation in non-epitaxially ordered regions.

6.2.4 Friction Dependence on Epitaxy

To further analyze these multi-layers, we carried out quantitative friction force microscopy (FFM) and Kelvin probe force microscopy (KFM) measurements, in conjunction with TSM. Figures 6.7A and 6.7B display the TSM and FFM images of a second layer crystallite of pentacene exhibiting coincidence-II epitaxy. Figure 6.7B clearly indicates that the second layer crystallite exhibits lower friction (dark) compared to the first layer. In contrast, Figs. 6.7C and 6.7D show the TSM and LFM images of a second layer crystallite that has grown across an underlying grain boundary in the first layer. The uniform TSM signal throughout the second layer island indicates that it is a single crystal and thus, this crystallite cannot be epitaxially ordered with both grains in the underlayer.

The intermediate TSM signal of the second layer grain and the first layer grain in the lower half of the Fig. 6.7C indicates epitaxial order in the lower domain. The FFM measurement of the same region (Fig. 6.7D) reveals the friction contrast within the second layer island. Importantly, the region of non-epitaxial order displays higher friction than the epitaxial region. The origin of higher friction in the non-epitaxial domains will require further investigation, but must be related to the interlayer coupling and also possibly to the presence of line dislocations that we have observed previously.[30] The important practical result is that the sharp contrast visible in the friction image is a map of epitaxial interactions. Low friction domains are epitaxial; high friction domains are not.

6.2.5 Electrostatic Surface Potential Dependence on Epitaxy

Figures 6.8A and 6.8B present the topographic and FFM images of the same region of a pentacene film. The topographic image reveals a completely coalesced first layer, large second layer islands (second layer islands lose their cross-shape at higher coverages), and a few small third layer islands. The friction image is a map of epitaxial interactions, specifically revealing the presence of epitaxial and non-epitaxial domains in the pentacene second layer.

To investigate the correlation between the thin film microstructure and the surface electrostatic potential distribution, we performed KFM on this sample layer. Figure 6.8C is the KFM image of the same area as in the FFM image, demonstrating that the first layer has the lowest surface potential and that the second layer has a higher surface potential with different sub-domains. The intriguing finding is that the surface potential domains in the second layer correspond directly to the friction domains in the FFM image (Figs. 6.8B and 6.8C). Comparison of the two figures demonstrates that the regions of lower friction (epitaxially ordered) exhibit higher (more positive) surface potential and the regions of higher friction (non-epitaxially ordered) exhibit lower (more negative) surface potential. Thus, there is a definite correlation between epitaxial order and the resulting electrostatic character of these films.

Figures 6.8D, 6.8E, and 6.8F display the pixel histogram analysis of the topographic, FFM, and KFM images, respectively. Figure 6.8D depicts the average height of the second layer on the first layer and the third layer on the second layer, while Fig. 6.8E reveals that the friction difference between the epitaxial and the non-epitaxial

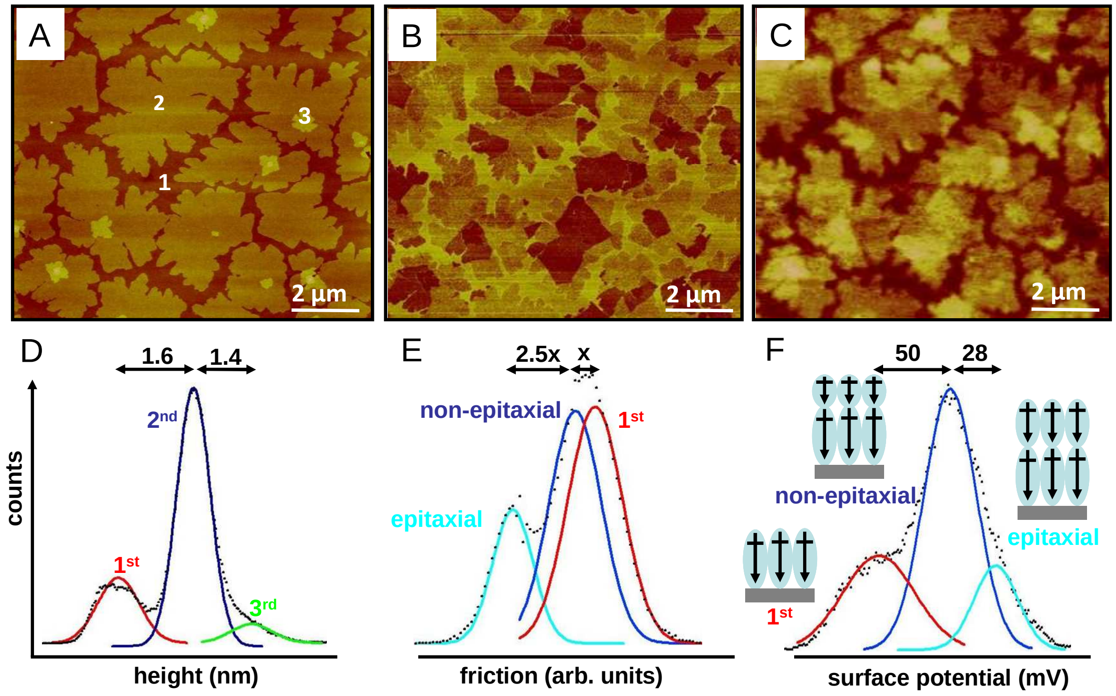

Figure 6.8 Electrostatic Surface Potential Dependence on Epitaxy A) Topography image displays a fully coalesced first monolayer, large second layer islands and a few third layer islands. B) FFM image demonstrates highest friction for the first layer and friction variation within the second layer. FFM images serve as maps of epitaxial interactions. C) KFM image shows that the first layer has the lowest surface potential and the second layer has a higher potential with different sub-domains. A one-to-one correlation exists between the friction domains and the surface potential domains. In the second layer, the areas of lower friction (epitaxially ordered) show higher (more positive) surface potential and the areas of higher friction (non-epitaxially ordered) show lower (more negative) surface potential. D) Histogram analysis of the topographic image demonstrates that the average heights of the second layer on the first layer and the third layer on the second layer correspond to 1.6 nm and 1.4 nm, respectively. E) Histogram analysis of the FFM image reveals that the friction difference between the epitaxial and the non-epitaxial second layer is ~ 2.5 times the friction difference between the first layer and the non-epitaxial second layer. F) Histogram analysis of the KFM image shows that the difference in the surface potential between the first layer and the non-epitaxial second layer is ~ 50 mV, and the difference between the epitaxial and the non-epitaxial domains in the second layer is ~ 28 mV.

domains in the second layer is more than two times the friction difference between the first layer and the non-epitaxial second layer. The friction maps can also be utilized to determine the degree of epitaxy, by quantifying the area under the epitaxial curve compared to the area under the non-epitaxial curve in the histogram. For example, the histogram analysis (Fig. 6.8E) of the friction image in Fig. 6.8B indicates that approximately 35 % of the second layer has grown epitaxially on the first layer. Figure 6.8F shows that the surface electrostatic potential difference between the first layer and the non-epitaxial second layer is ~ 50 mV and the difference between the non-epitaxial and epitaxial domains within the second layer is ~ 28 mV.

The correlation of the surface potential with epitaxial domains can have two possible explanations. One is the reported dipole formation of pentacene layers on SiO_2.[190] We hypothesize that in regions of epitaxial growth there is stronger electrostatic coupling (induced dipole-induced dipole interaction) between the layers, resulting in a higher observed surface potential. In contrast, for regions of non-epitaxial growth the registry mismatch leads to reduced electrostatic coupling and results in relatively lower surface potential as the summation of dipoles is smaller in magnitude. Fig. 6.8F provides a schematic illustration of this possible effect. The other likely explanation relates to the surface potential dependence on local deformations in pentacene. Specifically, it has been reported that the plastic deformation in metals (in the form of dislocations, vacancies, or pits) results in lower surface potential.[191,192,193] The non-epitaxially ordered second layer can undergo local plastic deformation (dislocation formation) due to the registry mismatch with the first layer, which may result in lower surface potential. Both explanations seem equally probable and our findings call for a more detailed theoretical model explaining the surface potential dependence on the presence and absence of epitaxial order.

The majority of charge transport in OFETs is confined within the first few layers of the organic semiconductor/insulator interface. Therefore, any surface potential variation within these layers will affect the charge carrier motion, as has been demonstrated for conventional inorganic semiconductors.[194,195,196] Consequently, we expect that the surface potential domains, resulting from domains of epitaxial and non-epitaxial order, can serve as trapping/scattering sites for carriers during transport, especially at low temperatures where thermal energy becomes comparable to the surface potential variations. In this respect, it is particularly noteworthy that the surface potential differences we have measured correspond well with the activation energy reported for the hole mobility in pentacene OFETs.[197,198]

6.3 Conclusion

In conclusion, we have demonstrated an unusual organic homo-epitaxy for films of the benchmark organic semiconductor pentacene. The most striking discovery is that the observed homo-epitaxy is not commensurate for the second pentacene layer grown on the first. Using TSM analysis, we demonstrated that the pentacene second layer grows with coincidence-II epitaxy on the first layer, while the third and subsequent layers grow commensurately on their respective underlayers. Further, we utilized FFM and KFM to probe the friction and the surface electrostatic potential dependence on the presence and absence of epitaxial order. The domains of epitaxial order exhibit lower friction and more positive surface potential than the non-epitaxial domains. Thus, there is a clear correlation between epitaxial order and electrical properties of these polycrystalline films. Collectively, these findings open up exciting new possibilities for understanding the growth of crystalline organic semiconductor films and for correlating microstructure with electrical performance in devices.

6.4 Experimental

Pentacene thin film growth

Ultrathin films of pentacene were grown by thermal evaporation of the source material onto insulating substrate under vacuum pressure of ~ 6×10^{-7} Torr and with deposition rates of ~ 0.01 Å/sec. All the films were grown on p-doped silicon wafers, with a thermally grown 300 nm thick amorphous silicon dioxide overlayer. High purity pentacene source material (~ 99.8%) was purified by repeated sublimations before it was used to grow films. All the scanning probe images and analysis are based on freshly grown pentacene films.

Transverse Shear Microscopy

TSM is a contact mode scanning probe microscopy technique in which the lateral twisting of the cantilever is recorded in conjunction with topography, enabling a direct correlation between the two. The fast scan direction (scan vector) is kept along the long axis of the cantilever and thus the observed twisting is not due to friction, but is a result of the anisotropic shear field in the image plane. The origin of transverse shear field is related to the crystallographic orientation of film at the surface. All TSM images were taken on a Veeco Nanoscope IIIA multimode atomic force microscope under ambient conditions. The probes used for AFM measurements were silicon nitride V-shaped cantilevers with integrated contact mode tips fabricated by Veeco Metrology, USA (Model DNP and force constant ~ 0.58 N/m). The images were obtained at a nominal load of ~ 3 nN and relative humidity of ~ 20 %. The scan rate for a (10 µm X 10 µm) image size is 1.5 Hz.

Friction Force Microscopy

FFM is a contact mode technique where the local variations in the sliding friction between the tip and the sample are mapped along with topography. The fast scan direction of the tip is kept perpendicular to the long axis of the cantilever such that friction forces on the tip twist the cantilever. The set up and tips used in FFM experiments were same as that used in TSM. All the FFM and TSM images shown in the figures are the forward trace scans.

Kelvin Probe Force Microscopy

KFM is a noncontact technique that measures the local surface potential along with topography, allowing a direct correlation between the two.[199,200] It operates in a two pass mode, where in the first pass the topography is measured and in the second pass the AFM tip is lifted a few nanometers from the sample surface at a constant distance relative to the topography and the surface potential is measured. In KFM, the surface potential is measured using a nulling technique with feedback control and it directly gives the surface potential in units of volts,[199,201] unlike electric force microscopy (EFM) which indirectly measures the surface potential through phase or frequency shifts.[202,203] Measurements were conducted in air with probe tips fabricated by Mikromasch USA (NSC35-B tips, Ti/Pt coated, resonant frequency 240–405 kHz, and lift height 10 nm). The measurements were repeated inside a glove box with O_2 level ~ 2 ppm and no difference was observed.

6.5 Acknowledgements

The authors thank Michael D. Ward (New York University) for useful discussion and a critical reading of the manuscript. This work was partially supported by the MRSEC Program of the National Science Foundation under Award Numbers DMR-0212302 and DMR-0819885. Partial support was also provided by NSF through DMR-0706011. Parts of this work were carried out in the Institute of Technology Characterization Facility, University of Minnesota, which receives partial support from NSF through the NNIN program.

Chapter 7

Strain Induced Homo-Epitaxial Transitions and the Growth Mode of Organic Semiconductor Thin Films

(Contributing Authors: Vivek Kalihari, Mun Ee Woo, Greg Haugstad, C. Daniel Frisbie)
(work submitted to *Advanced Functional Materials*)

We describe a correlated strain and growth model for ultrathin polycrystalline pentacene films deposited from the vapor phase on a variety of insulating substrates. For a monolayer thick pentacene film in which the long axes of the molecules are perpendicular to the substrate, the estimated compressive and tensile strain energies are on the order of 15 - 70 meV/molecule. We propose that strain is the cause of the observed in-plane crystallographic twist of the second layer with respect to the first, resulting in coincidence-II homoepitaxy. The driving force for the epitaxial mode is the alignment of the principal axes of tension and compression in the two crystalline layers, which attenuates the overall strain, and allows the third and the subsequent pentacene layers to grow commensurately. Partial strain release also causes the thin film growth mode to switch from two dimensional to three dimensional growth (a hallmark of the Stranski-Krastanov mode), which is rationalized through the thickness variation of the thin film chemical potential. We find similar results for a variety of other organic semiconductor ultrathin films, suggesting that strain release by the in-plane crystallographic twist of the organic layers near the substrate is a general interfacial reconstruction.

7.1 Introduction

Organic semiconductor thin films play an important role in many technological applications including organic thin film transistors (OTFTs),[9,10,11,12,13] organic solar cells,[16,204] and organic light emitting diodes.[17,205] Such films, like any other films, tend to develop mechanical stresses as they are deposited. These stresses can result from both intrinsic factors such as the lattice mismatch and the surface energy difference between the substrate and the organic film, or extrinsic factors such as the thin film deposition parameters (substrate temperature and deposition flux) and post growth treatments (annealing, quenching etc.).[43] The mechanical stresses, when large enough, can introduce structural defects and/or a change in thin film growth mode at the micro-scale and can also cause film delamination or buckling at the macro-scale.[206] As organic thin film interfaces are critical in different device structures, the mechanical stresses and the resulting strains associated with the early stages of organic semiconductor thin film growth can impact the performance and the reliability of organic devices.

In inorganic semiconductor thin film technology, the genesis of strains present at thin film interfaces and their affect on film structure and properties is generally well understood.[207] For example, strain provides control over electronic band offsets and can increase the electron mobility in silicon.[208] Unfortunately, similar work has been missing in the field of organic semiconductor thin films and there are only a handful of studies that relate strain and film morphology in organic systems.[209,210] Organic thin films, unlike inorganic films, are held together via weak forces (such as dispersion and multipolar forces; elastic moduli ~ 10 GPa)[211] and therefore, stresses present in the film can result in exceptionally large strains with profound implications for thin film growth modes, microstructure development, and electrical properties.

Among small conjugated organic semiconducting molecules, pentacene stands out because of its ability to form well-ordered crystalline films on a variety of substrates and the resulting high hole mobilities in OTFTs.[123,124,153,181] In an OTFT, the current modulation is restricted to the accumulation layer, which corresponds to a few monolayers of organic semiconductor on top of the gate dielectric.[14,15] Therefore, the strain and the resulting microstructure of the first few molecular layers directly adjacent to the gate dielectric are critical in determining transistor performance. In the past, organic semiconductor thin films have been analyzed using various characterization techniques such as atomic force microscopy,[25,26,27,28,29] electron microscopy,[22,23,24] x-ray diffraction techniques,[18,19,20,21] and scanning tunneling microscopy.[212,213] But to the best of our knowledge, the methodical investigation of strain development and its affect on growth morphology in organic semiconductor thin films has not been reported.

Here, we present a model for strain in ultrathin polycrystalline films of the benchmark organic semiconductor pentacene deposited by physical vapor deposition on a variety of substrates. We show that the strain in the first wetting layer next to the dielectric surface induces an unusual in-plane “twist” of the second layer on top of the first layer. This twisting is more formally defined as coincidence-II epitaxy, as previously reported by us for pentacene thin films on amorphous silicon dioxide (SiO_2) substrates.[188,33] Coincidence-II epitaxy minimizes the strain energy in the first two pentacene layers, as shown by in-plane strain calculations based on the unit cell parameters. In turn, the relaxation of strain allows the third and the subsequent layers to grow commensurately on top of their respective underlayers. The partial strain release also induces a growth mode switch from layer-by-layer or two dimensional (2-D) growth to three dimensional (3-D) growth, a hallmark of the Stranski-Krastanov (S-K) thin film growth mode.[214] Similar results are found for a variety of other organic semiconductor ultrathin films, indicating that both strain in the wetting layer and its relief by in-plane "twisting" of the second layer, are a general phenomenon in organic semiconductor thin films grown on amorphous substrates.

7.2 Results and Discussion

7.2.1 Epitaxial Relationships

Previously, using a novel transverse shear microscopy (TSM) technique,[30,31,32,33,34] we established the epitaxial relationships between successive pentacene layers grown on an amorphous SiO_2 dielectric.[33] However, SiO_2 is not the dielectric of choice for most organic electronics applications as it is brittle. Here, we examine epitaxial relations in vacuum deposited ultrathin pentacene films on a variety of polymeric substrates (poly[methyl methacrylate] (PMMA), polystyrene (PS), and poly[α-methyl styrene] (PAMS)) that are often used as dielectrics in OTFTs.[28]

Figure 7.1 shows height (left column) and corresponding TSM (right column) images of ultrathin (1-2 nm) pentacene films on polymeric substrates along with SiO_2 for comparison. All the height images demonstrate that the growth of the first layer is 2-D, *i.e.*, only after substantial coverage of the first layer, the second layer nucleates. The TSM

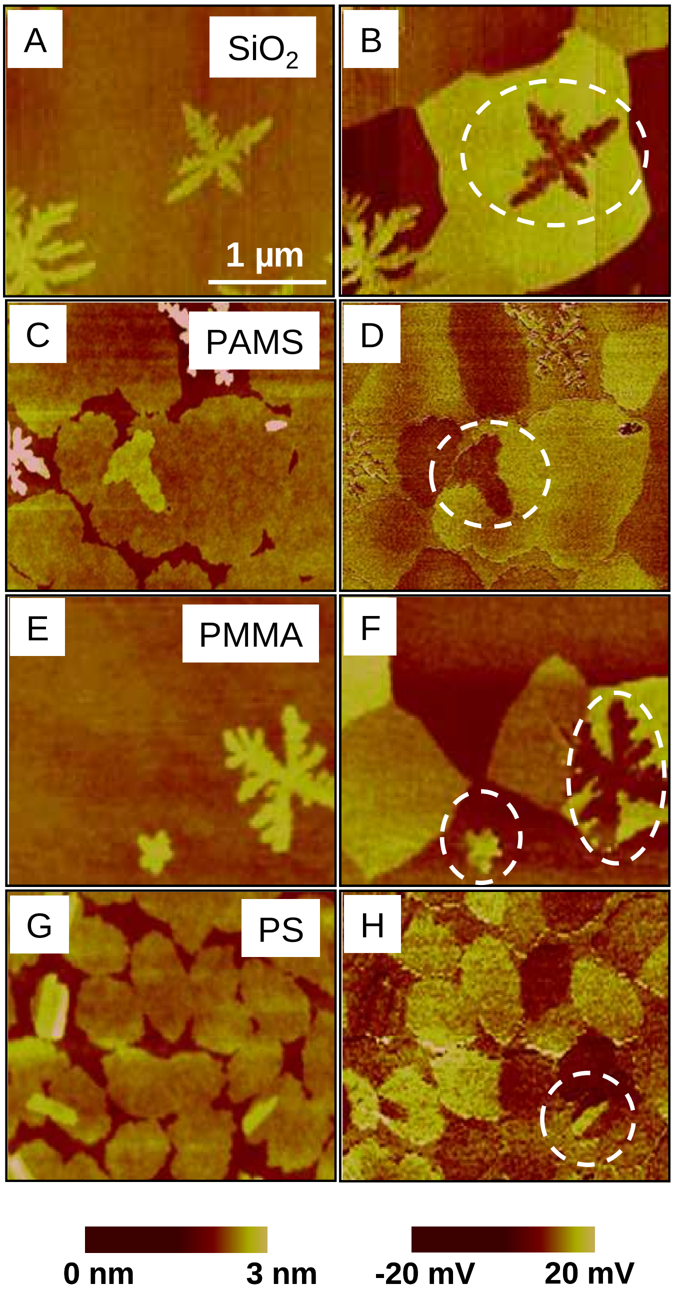

Figure 7.1 Pentacene Ultrathin Film growth on Polymers Height (left column) and corresponding TSM (right column) images of ultrathin (1-2 nm) pentacene thin films on (A, B) SiO_2, (C, D) PAMS, (E, F) PMMA, and (G, H) PS. All the height images show a fully grown first pentacene layer and few second layer islands. The dashed circles in the TSM images demonstrate that a bright second layer grows on top of a dark first layer or *vice versa*, indicating coincidence-II epitaxy between the two layers.

images in the right column reveal color domains corresponding to different grains in the polycrystalline first layer. Clear differences in the TSM signal between the second layer large islands and the first layer are also evident. As the TSM signal is sensitive to crystallographic orientation, the contrast indicates the absence of commensurism between the second and first layers of pentacene on all the polymeric substrates and SiO_2. Usually, one observes that a bright second layer grows on top of a dark first layer or a dark second layer grows on top of a bright first layer (dashed circles). As previously established on SiO_2 substrates,[33] this TSM contrast between the first and the second layer corresponds to coincidence-II epitaxy between the two layers. Figure 7.1 demonstrates that this “twisted epitaxy” is germane to pentacene on polymeric substrates as well.

In the nomenclature of epitaxy, the underlayer and the overlayer lattice vectors are related through a transformation matrix, where the matrix coefficients define the mode of epitaxy.[188] In case of coincidence-II epitaxy, all the matrix elements are rational and no column of the matrix consists of integers. In simple terms, this means that the coincidence-II epitaxy results in a precise registry of the underlayer and the overlayer molecules at the corners of a supercell. In our previous article,[33] we reported that the coincidence-II epitaxy between the pentacene second and first layers on SiO_2 implies a 4 X 4 supercell in the second layer.

A statistical analysis of hundreds of second layer pentacene grains on the polymeric substrates indicates that the growth mode of pentacene thin films on polymeric substrates is phenomenologically similar to that on SiO_2. As in the case of SiO_2 substrates, coincidence-II and commensurism coexist between the first and the second

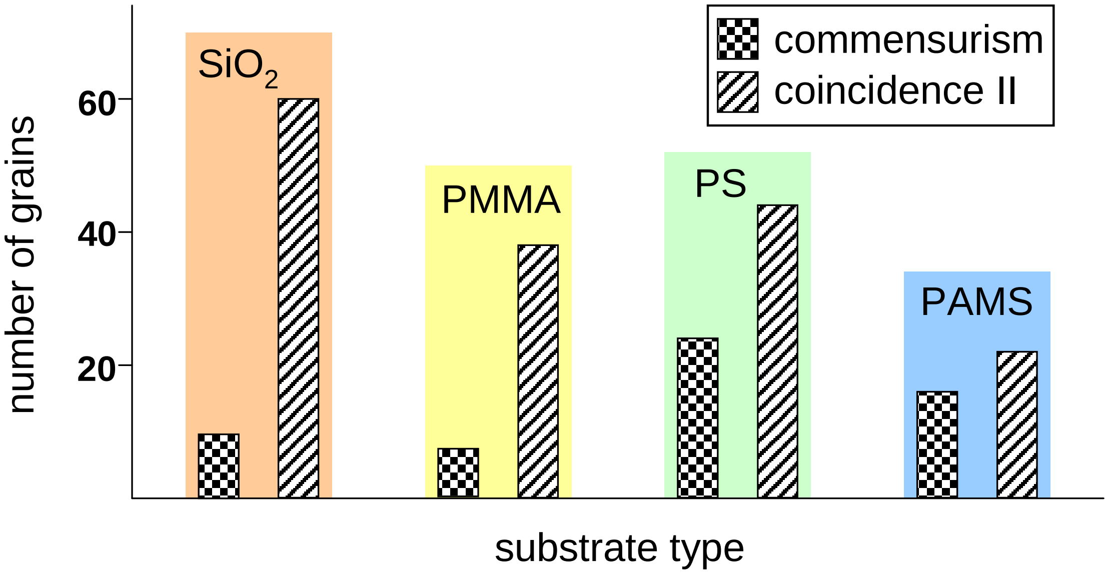

Figure 7. 2 Statistical Analysis of Pentacene Second Layer Growth on Polymers Histogram plot showing the population of coincidence-II and commensurism between the pentacene first and second layer on a variety of amorphous substrates. The plot demonstrates that both the epitaxial modes coexist on all the investigated substrates (SiO_2 and three polymers), but their relative population depends on the substrate type. Specifically, the relative populations of coincidence-II on different substrates are: SiO_2 = 85 % ± 5 %, PMMA = 87 % ± 7 %, PS = 64 % ± 7 %, and PAMS = 60 % ± 8 %.

pentacene layers on all the polymeric substrates. Figure 7.2 shows the histogram where the populations of coincidence-II and commensurate grains are plotted for all substrates. It is clear from the plot that coincidence-II and commensurism coexist on all substrates, but their relative population depends on the substrate type. This change is expected given the different chemistries and surface energies of the substrates. Specifically, the relative population of the two epitaxies is skewed towards coincidence-II in case of SiO_2 and PMMA, whereas in case of PS and PAMS the relative population is quite comparable. The dependence of the relative populations on the substrate type is currently under investigation. However, the most important point is the presence of coincidence-II epitaxy on all the substrates. This solidifies the generality of coincidence-II epitaxy in pentacene ultrathin films near the substrate interface.

In order to examine the epitaxial relationships further away from the pentacene/dielectric interface, we grew thicker (~ 4 layer) pentacene films for TSM analysis. Figure 7.3 shows the height and the corresponding TSM images of thicker films of pentacene on PMMA and SiO_2. The height images in the left column show a multilayered pentacene film. Careful inspection reveals that the second and subsequent layers grow in a 3-D mode, in contrast to the 2-D growth mode adopted by the first layer. This growth mode transition is discussed in more detail below. The TSM images in the right column show a similar TSM signal for the second and subsequent layers. This indicates that the in-plane crystallographic orientation of the second layer is similar to the subsequent layers, resulting in commensurism between them. The observation is general for SiO_2 and all the polymeric substrates.

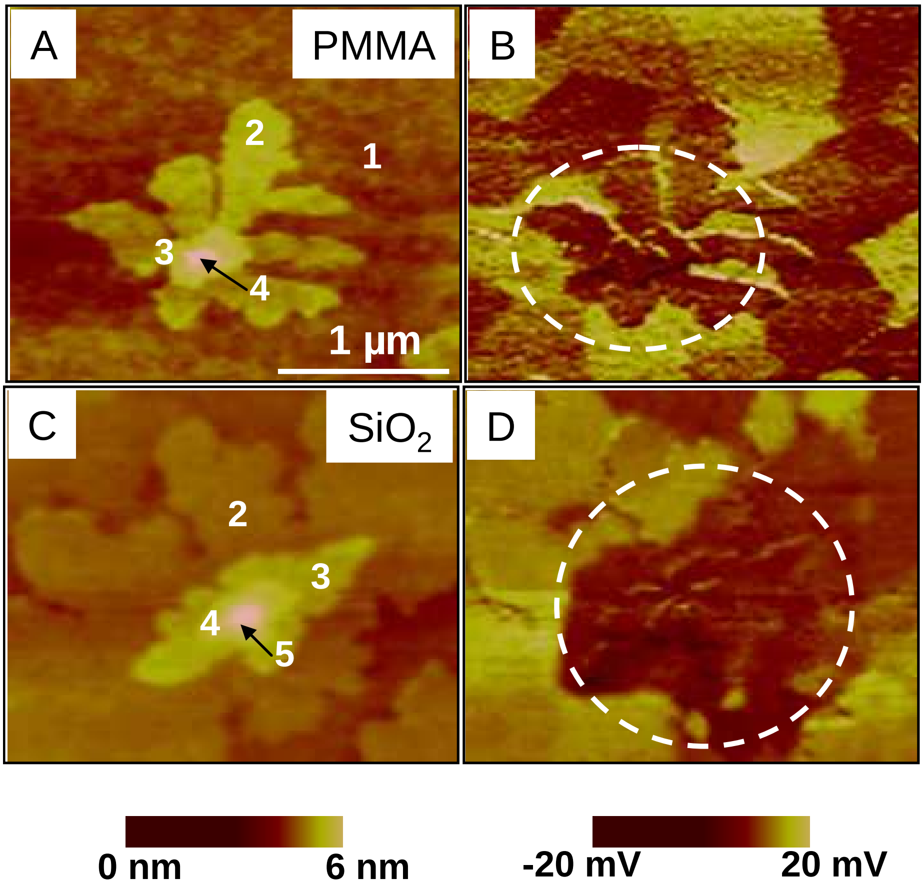

Figure 7.3 Third and Subsequent Pentacene Layers on Polymers Height (left column) and corresponding TSM (right column) images of a relative thick (~ 4 layers) pentacene film on (A, B) PMMA and (C, D) SiO_2. The height images show a multilayered pentacene film. The dashed circles in the corresponding TSM images demonstrate similar TSM signals for the second and subsequent layers, indicating commensurism between them.

In summary, we find that coincidence-II epitaxy exists along with commensurism for the pentacene second layer on all the substrates. For thicker pentacene films, only commensurism is found to occur, *i.e.*, there is no crystallographic twist between the second and the subsequent layers. This is an important finding as it indicates that the epitaxial relationships in pentacene films are different near and away from the interface, but follow the same trend for organic (polymeric) and amorphous inorganic (SiO_2) substrates. This observation also indicates the possible role of interfacial strain in deciding the mode of epitaxy.

7.2.2 Strain and Coincidence Epitaxy

In our previous article,[33] we postulated that large strain fields in the first and second layer induces a second layer twist on top of the first, as strain free conditions should have resulted in commensurism in homogeneous thin films. We can now justify the twisting mechanism by geometrical considerations based on the unit cell parameters. The coincidence-II epitaxy between the second and the first layer of pentacene results in the alignment of different diagonals in the two layers. For example, the [110] diagonal in the second layer aligns with the $[\bar{1}10]$ diagonal in the first layer or *vice versa*. The alignment of different diagonals in the two layers prompted us to calculate the strains along the diagonals in the two layers. In order to calculate the strains, we took the bulk pentacene unit cell parameters as the reference lattice parameters. The bulk packing is the most stable lattice configuration for any molecular system, in contrast to strained packing for molecules on top of an inherently different substrate or near an interface.

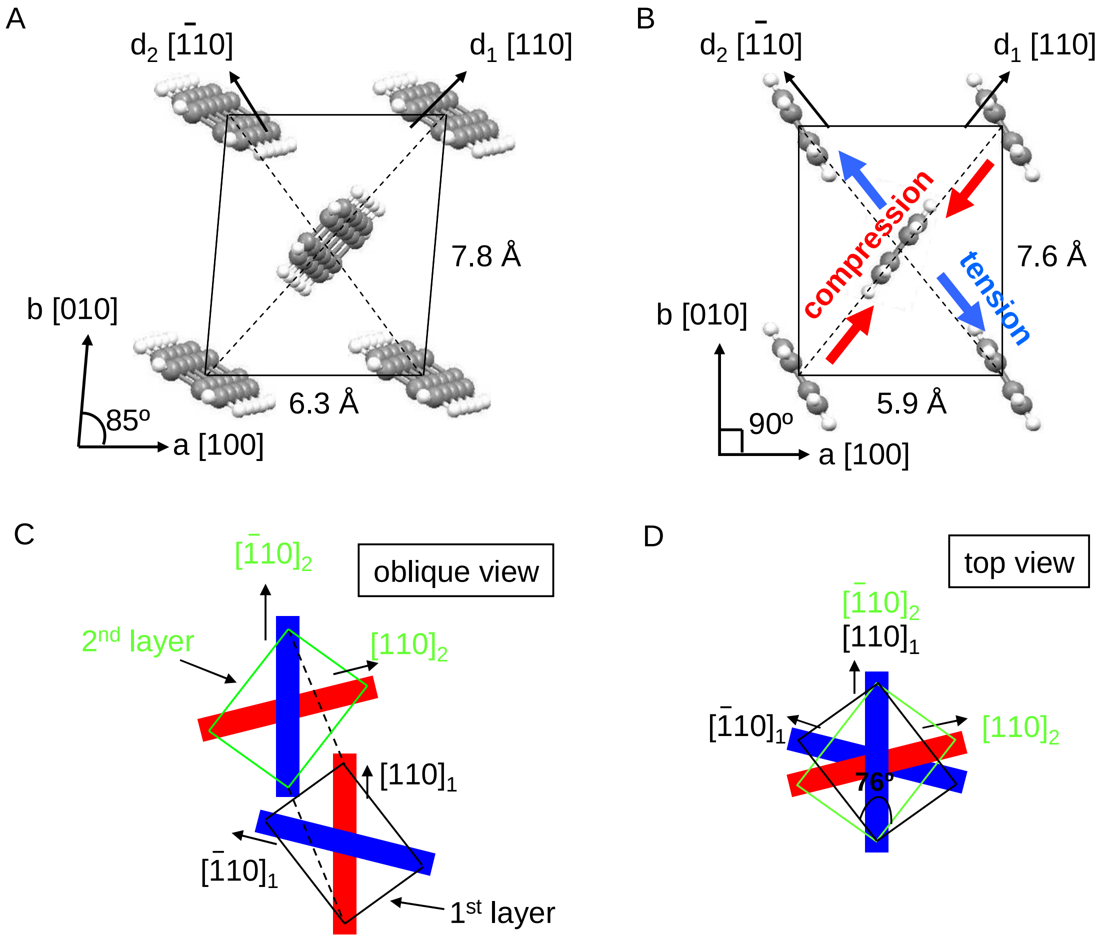

Figure 7.4 Pentacene Monolayer Strain Calculations The (001) plane of A) bulk pentacene: a = 6.266 Å, b = 7.775 Å, and γ = 84.68° [215], and B) a pentacene monolayer on SiO$_2$: a = 5.916 Å, b = 7.588 Å, and γ = 89.95° [18,21]. Assuming the bulk pentacene unit cell to be strain free, geometrical calculations reveal that the [110] diagonal is under compressive strain while the $[\bar{1}10]$ diagonal is under tensile strain (depicted schematically in Fig. 4B) in the monolayer unit cell. C) Oblique view and D) top view of the alignment of the two diagonals ([110] and $[\bar{1}10]$) in the pentacene first and second layer resulting in coincidence-II epitaxy between them.

Figure 7.4A depicts the (001) plane of bulk pentacene[215] (a = 6.266 Å, b = 7.775 Å, and γ = 84.68°) and Fig. 4B shows the (001) plane of a pentacene monolayer on SiO$_2$[18,21] (a = 5.916 Å, b = 7.588 Å, and γ = 89.95°). The pentacene unit cell parameters on polymeric substrates are unknown, but similar epitaxial relationships (Figure 7.2) and the presence of the "thin film phase" of pentacene thin films on SiO$_2$ and the polymers suggests that the unit cell parameters are similar on SiO$_2$ and polymeric substrates.[216,217, 218]. Geometrical calculations and comparison of Figs. 7.4A and 7.4B reveal that in the monolayer unit cell the spacing between the molecules along the [110] diagonal is smaller than the corresponding spacing along [110] in the bulk unit cell. Whereas, the spacing between the molecules along the $[\bar{1}10]$ diagonal is larger than the corresponding spacing in the bulk unit cell. Thus, the [110] diagonal in the monolayers is under compression while the $[\bar{1}10]$ diagonal is under tension (depicted schematically in Fig. 7.4B).

Comparison of the lengths of the diagonals in the two structures reveals that the percentage strain along [110] is ~ - 8 % and along $[\bar{1}10]$ is ~ + 2 %. These are large strains, much higher than the normal strains found in inorganic thin films (~ 0.5 to 1 %).[207207] However, such large strains are compatible with the relatively weak bonds holding the molecules together in organic thin films. Similar strains (~ 8 %) have been reported for organic crystalline films of 3, 4, 9, 10-perylenetetracarboxylic dianhydride (PTCDA) on Au (111) surfaces.[209]

It is useful to try to estimate the strain energy associated with the monolayer phase. The strain energy is given by the area under the stress-strain curve, *i.e.*, it is an integral of stress over strain along the curve.[219] This means that an exact calculation requires the knowledge of the stress-strain behavior in both the elastic and plastic regimes (a typical oligoacene yield strain is ~ 1 %). However, the elastic modulus (E) and strain (ε) are tensor quantities and to our knowledge, the tensor components are not available. One can get an approximate value of the strain energy by assuming a uniaxial stress condition along the maximum strain direction, *i.e.*, we view the monolayer strained state as arising from uniaxial compressive stress of the bulk structure along [110] (see Fig. 7.4). We then can bound the strain energy by computing the area under the hypothetical stress-strain curve assuming either ideal plastic (lower bound) or ideal elastic (upper bound) behavior up to 8 % strain. The elastic modulus for pentacene is ~ 10 GPa. [220] The calculations give the strain energy on the order of 11 - 48 mJ/m^2 or ~ 15 - 70 meV/molecule.

The unit cell lattice parameters of the second layer of pentacene are unknown, but a similar strained state for the second layer is expected because an abrupt change in the lattice parameters is highly unlikely in a homogeneous thin film. We hypothesize that the strain between the two layers is minimized when the second layer grows with coincidence-II epitaxy on top of the first layer, such that one of the diagonals of the second layer aligns with the other diagonal of the first layer. For example, the compressed [110] diagonal in the second layer aligns itself with the $[\bar{1}10]$ diagonal of the first layer which is under tension (as shown in Figs. 7.4C and 7.4D). Thus, this particular

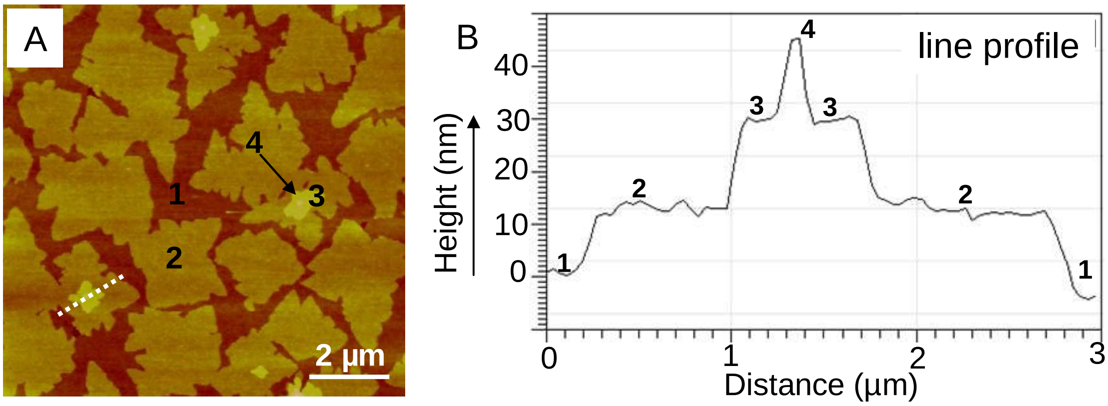

Figure 7.5 The Stranski-Krastanov Growth of Pentacene Thin Films A) Height image of a thick (~ 4 layers) pentacene film on SiO_2, B) A line profile of the white dashed line in Fig. 7.5A. The height image shows no substrate which demonstrates that the first pentacene layer completely covers the substrate surface. The line profile, along with the height image, demonstrates that the second and subsequent layers grow in a 3-D mode which is rationalized by the growth of subsequent layers before the complete growth of a previous layer.

coincidence-II epitaxy alignment releases some of the strain present in the pentacene layers. On the contrary, if there were no orientation between the second and the first layers then diagonals with similar stresses would have aligned (commensurism) resulting in minimal strain release. The partial strain release is the driving force for the coincidence-II epitaxy, which has been observed on all the investigated substrates.

The strain removal in the first two layers by coincidence-II epitaxy also explains the commensurate growth of the third and subsequent layers on top of their respective underlayers. When the third layer nucleates on top of the second layer, it grows on a less strained second layer and thus, grows commensurately. A similar growth mode is adopted by all the subsequent layers.

7.2.3 Growth Mode Transition

In this section, we address the growth mode transition for second and subsequent layers of pentacene thin films. Figure 7.5A shows a height image of a relatively thicker (~ 4 layer) pentacene film on SiO_2, and Fig. 7.5B represents a line profile of the white dashed line in Fig. 7.5A. The height image shows no substrate which demonstrates that the first pentacene layer completely covers the substrate surface. The line profile, along with the height image, indicates that the second and subsequent layers grow in a 3-D mode as evidenced by the growth of subsequent layers before the complete growth of a previous layer. Hence, there is a transition in the thin film growth mode from 2-D to 3-D and this mode is termed as the S-K thin film growth mode. Similar growth mode transition has been observed before for the pentacene/SiO_2 system using x-ray scattering studies.[221,222] In the S-K growth mode, initial layers (wetting layers) grow 2-D and after a critical number of wetting layers the growth mode changes to 3-D in order to relieve strain in the 2-D grown layers.[43]

To explain the growth mode transition, we consider the thickness variation of chemical potential of pentacene thin films. The following general equation describes the chemical potential of a molecule belonging to the nth layer $\mu(n)$ of a film:[223]

$$\mu(n) = \mu_\infty + [\varphi_a - \varphi_{a'}(n) + \varepsilon_d(n) + \varepsilon_e(n)] \qquad (1)$$

Where μ_∞ = chemical potential of the molecule in its bulk phase, φ_a = desorption energy of an adsorbate molecule from the surface of the same material, $\varphi_{a'}(n)$ = desorption energy of an adsorbate molecule from the substrate, $\varepsilon_d(n)$ = energy per molecule of the misfit dislocations present in the film, and $\varepsilon_e(n)$ = energy per molecule of the homogeneous strain present in the film.

The sign of the first derivative of the chemical potential ($d\mu(n)/dn$) gives the sign of the curvature of the free energy of the system and thus, decides the thin film growth mode. When $d\mu(n)/dn > 0$ (every subsequent layer has a higher chemical potential), the complete growth of the previous layer takes place before the start of the subsequent layer growth and this thin film growth mode is called Frank-van der Merwe growth (2-D or layer-by-layer growth). On the other hand, when $d\mu(n)/dn < 0$ (every subsequent layer has a lower chemical potential), the formation of the subsequent layer before the completion of the previous layer is thermodynamically favored which leads to 3-D island growth. This thin film growth mode is called Volmer-Weber growth. In the S-K growth, $d\mu(n)/dn > 0$ near the interface which results in the formation of wetting layers by 2-D growth, but $d\mu(n)/dn$ changes sign after the growth of a critical number of wetting layers. Thereafter, the strain stored in the wetting layers (ε_d) gets relaxed through either the introduction of misfit dislocations or the coherent 3-D island growth of the subsequent layers on top of wetting layers. The thickness of the wetting layer where 3-D island nucleation initiates or misfit dislocations get introduced is called the critical thickness h_c. For the pentacene thin film growth on the investigated substrates, h_c corresponds to the thickness of the first monolayer (~ 15 Å) as the second and subsequent layers exhibit 3-D growth. The thickness (or the number) of the wetting layers is inversely proportional to the strain present in the film. Only a single pentacene monolayer as the wetting layer indicates that the pentacene thin films are highly strained at the pentacene/SiO_2; indeed, this conclusion is consistent with the apparent ~ 8 % strain along [110] (Figure 7.4B).

The first derivative of the chemical potential ($d\mu(n)/dn$) is given by:

$$\frac{d\mu(n)}{dn} = -\frac{d\varphi_{a'}(n)}{dn} + \frac{d\varepsilon_d(n)}{dn} + \frac{d\varepsilon_e(n)}{dn} \qquad (2)$$

In order to understand the growth mode transition in pentacene thin films, we will consider each of the three terms in the right hand side of *Eq. (2)* for the pentacene first and second layer growth, as the two layers exhibit different growth modes.

First term: The S-K growth mode requires $\varphi_{a'}(n)$ to be greater than φ_a and the lattice mismatch to be nonzero (which is satisfied in our case because of the growth of polycrystalline pentacene films on amorphous substrates). During the S-K growth, $\varphi_{a'}(n)$ approaches φ_a as n increases meaning $d\varphi_{a'}(n)/dn$ will be always negative close to the interface. Therefore, the first term ($-d\varphi_{a'}(n)/dn$) will be always positive for pentacene thin film growth near the substrate interface, *i.e.*, for both the pentacene first and second layer growth.

Second term: The second term ($d\varepsilon_d(n)/dn$) represents a energy change in a thin film due to the introduction of lattice misfit dislocations. Previously, we have reported dislocations in some parts of the second layer islands which had grown beyond the grain boundary of the first layer underneath.[30,33] However, the second "seed" layer is free of dislocations. The epitaxial relationship between the first and the second layer, once the second layer crosses the grain boundary underneath, and the presence of dislocations in those regions are a part of current investigation. Also, we have not observed any dislocations in the first layer. Therefore, the second term in *Eq. (2)* will be zero for both the first and the second layer growth.

Third term: The third term ($d\varepsilon_e(n)/dn$) in *Eq. (2)* represents a change in the homogeneous strain present in a film by the addition of multiple layers. For the pentacene first layer growth on amorphous substrate, this term will be positive as unit cell calculations reveal that the first layer is under strain. For the second layer growth on top of the first layer, this term will be negative because the coincidence-II releases strain present in the two layers. As $d\varepsilon_e(n)/dn$ changes sign during the growth of the first two layers, it can be considered as a key parameter governing the transition in thin film growth mode.

Incorporating all the above points, $d\mu(n)/dn > 0$ for the pentacene first layer growth as the first and the third terms are positive and the second term is zero. Thus, the first layer grows in a 2-D mode and forms a wetting layer on the substrate. For the second layer growth, the first and the third terms are of opposite signs and the second term is zero. A change in the growth mode for the second and subsequent layers suggests that $d\mu(n)/dn$ changes sign for the second layer growth, meaning the absolute value of $d\varepsilon_e(n)/dn$ should be greater than ($-d\varphi_{a'}(n)/dn$). More importantly, the requirement of the third term ($d\varepsilon_e(n)/dn$) to be negative in order to justify the growth mode transition solidifies our previous conclusion that the coincidence-II epitaxy releases strain in the pentacene first and second layer.

7.2.4 Cause of Strain in the First Monolayer?

The question regarding the origin of strain present in the pentacene first layer still remains unanswered. In this section, we try to rationalize the first layer strain based on the upright position of pentacene molecules in the first layer, as opposed to the normally tilted configuration in the bulk crystal.[18] We discuss the strained packing in the first layer in terms of the anisotropic polarizability of pentacene molecules and the formation of a first layer induced molecular dipoles.[190,224]

Pentacene molecules diffuse on SiO_2 substrates with their long axis parallel to the substrate surface as this maximizes the Van der Waals interaction between the molecules and the amorphous substrate. When the diffusing molecules try to become a part of a first layer island, they stand up because the pentacene-pentacene edge-to-face interactions are favored over pentacene-SiO_2 interaction.[69,77] In the absence of any interface effect, the molecules should pack in a strain free bulk crystal structure and thus, exhibit a ~ 25° tilt

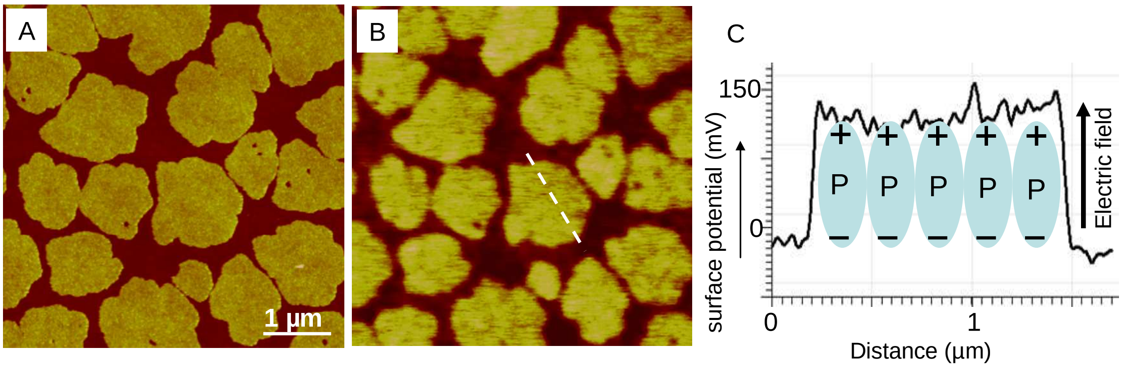

Figure 7.6 Pentacene Molecular Dipole A) Height (left column) and B) corresponding surface potential (right column) images of monolayer pentacene islands on SiO_2. The surface potential plot clearly demonstrates that the pentacene islands have more positive surface potential than the SiO_2 substrate. C) A line profile corresponding to the white dashed line in Fig. 7.6B, indicates that the surface potential difference is ~ 150 mV. It also shows a schematic of pentacene molecular dipoles at the substrate interface and its parallel alignment with the interface electric field.

in the **a**-**b** plane. Instead, they stand upright on the SiO_2 substrate without any molecular tilt in the **a**-**b** plane. We and others have previously observed by Kelvin probe force microscopy (KFM) that single monolayer pentacene islands have a more positive surface potential that the SiO_2 substrates.[30,190] Figures 7.6A and 7.6B show height and corresponding surface potential images of pentacene monolayer islands on SiO_2 substrate. Figure 7.6C displays a line profile corresponding to the white dashed line in Fig. 7.6B, showing the large ~ +150 mV surface potential change between pentacene and SiO_2. The potential difference implies that the pentacene molecules are polarized. Pentacene is known to have significant polarizability along its main π-conjugated axis. Given the known anisotropic polarizability of pentacene, the molecule will prefer to stand up with its long axis perpendicular to the SiO_2 substrate, as shown in Fig. 7.6C. [225]

The question of the origin of the interfacial polarization naturally arises. There are several possibilities, but a likely one is that dipoles inherent to the SiO_2 substrate, associated with oriented O-H bonds for example, induce the polarization of pentacene – a dipole-induced dipole interaction, which is directly proportional to pentacene polarizability. Clearly, more work will need to be done to determine the cause of polarization. That the pentacene molecules are polarized is firmly established by the 150 mV potential across the 1.5 nm thick pentacene layer, which corresponds to an effective field of 10^6 V/cm.

We propose then that the first pentacene monolayer structure involves competing energy terms. There is a significant energy cost in terms of strain for pentacene to adopt the monolayer unit cell structure shown in Fig. 7.4B. However, the strained state is stabilized by the polarization energy associated with induced pentacene molecular dipoles. One can make a quasi-quantitative assessment. We have estimated that the strain energy is on the order of ~ 15 - 70 meV/molecule, though the 70 meV/molecule upper limit is likely too large as the strain calculation assumed completely elastic deformation. On the other hand, if one views the first pentacene monolayer as a capacitor with a 150 mV potential difference, the effective electronic stabilization energy due to interfacial polarization is 30 meV/molecule (energy = $\frac{1}{2} CV^2 = \frac{1}{2} Ak\varepsilon_0 V^2/d$, where A is the area per molecule, k is ~3, and d = 1.54 nm). Thus, the polarization energy "gain" is at least comparable to, and likely larger than, the strain energy "cost". We propose that the strained pentacene monolayer phase on SiO_2 is a result of (and is stabilized by) interfacial electrical polarization.

7.2.5 Other Organic Semiconductor Ultrathin Films

Similar layer orientations of pentacene thin films on a variety of amorphous substrates motivated us to examine the generality of this growth behavior for other organic semiconductor thin films. Figures 7.7A and 7.7B correspond to height and TSM images of ultrathin films of napthalene-2thiophene-naphthalene (Fig. 7.7C) on SiO_2. The height image shows a fully coalesced first layer and two large second layer islands. The circled part of the corresponding TSM image clearly demonstrates that the second layer TSM signal is different from the first layer, indicating a lack of commensurism between the two layers. Similarly, Figs. 7.7D-E and G-H show height and corresponding TSM images of ultrathin films of PTCDI-C_8 (Fig. 7.7F) and para-sexiphenyl (Fig. 7.7I) on SiO_2. The circled regions in all the TSM images indicate a lack of commensurism

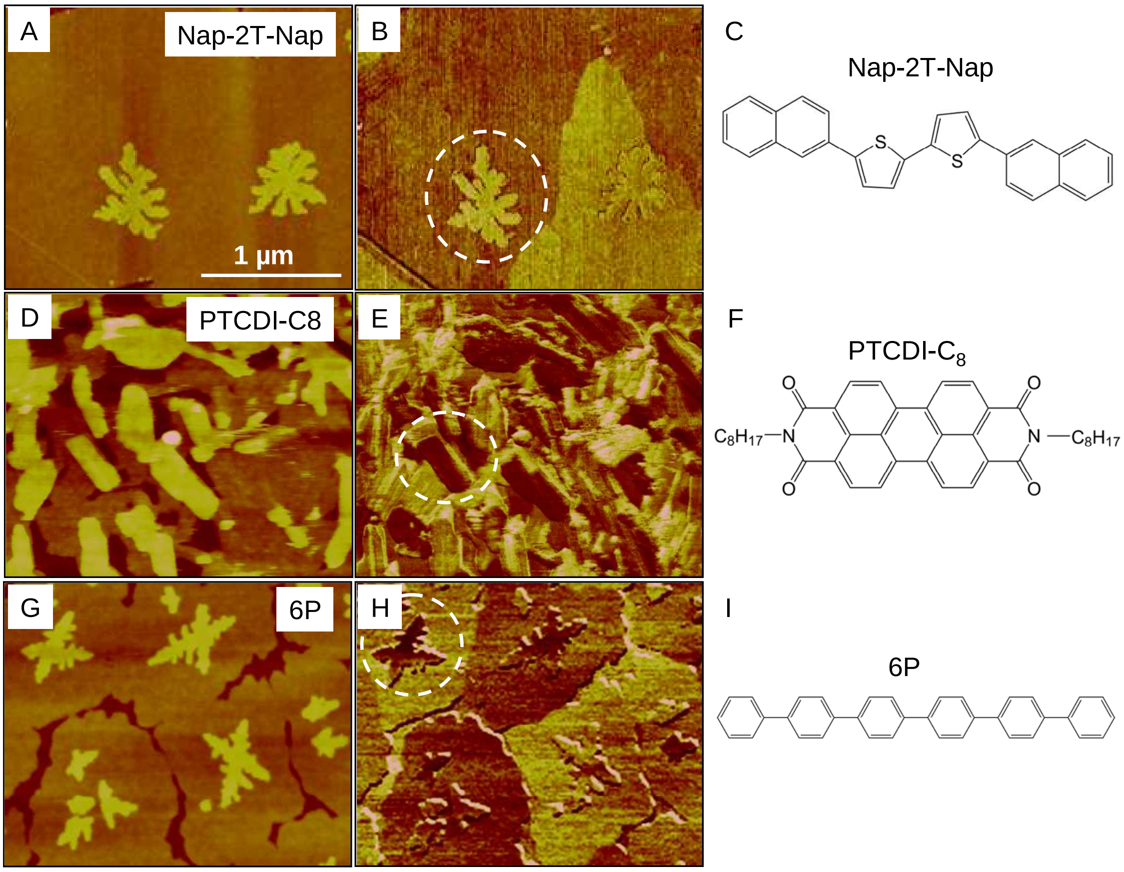

Figure 7.7 Organic Semiconductor Thin Films Thin film height (left column), corresponding TSM image (middle column), and molecular structure (right column) of (A, B, C) naphthalene-2thiophene-napthalene, (D, E, F) PTCDI-C_8, and (G, H, I) para-sexiphenyl. The circled regions in the TSM images show a TSM signal difference between the first and the second layer, indicating some in-plane "twist" between the layers. This indicates that the relative in-plane orientation between thin film layers near the interface is a general phenomenon for organic thin films.

between the first and the second layers. This indicates that the in-plane orientation between the thin film layers near the interface is a general phenomenon for organic thin films. The in-plane twist can be thought of as a fundamental strategy adopted by the organic thin films to release strain present in the wetting layers and can have a wide impact in determining various thin film properties especially near the interface.

7.3 Conclusion

In conclusion, we have developed a model relating strain and homoepitaxial growth for vacuum deposited ultrathin pentacene films on a variety of amorphous substrates (SiO_2 and three polymers). The model is based on the presence of compressive and tensile strains in the pentacene first monolayer, which induce an unusual in-plane twist of the second layer on top of the first layer, resulting in coincidence-II epitaxy. The driving force of the observed coincidence-II epitaxy is the partial strain release in the first two layers. The partial strain release allows the third and subsequent layers to grow commensurately on their respective underlayers. The partial strain release also results in a thin film growth mode switch from 2-D to 3-D growth, which is rationalized by the thickness variation of the thin film chemical potential. TSM analysis establishes the generality of in-plane twisting between ultrathin layers of rod-shaped molecules near the substrate interface. We have shown previously that different epitaxial domains in pentacene have different surface potentials, which connects film microstructure to electrical properties. Further work is ongoing to examine whether such structure-potential correlations are also general in other organic semiconductor films.

7.4 Experimental

Organic semiconductor thin film growth: Ultrathin films of pentacene and other organic semiconductors were grown by thermal evaporation of the corresponding source material onto insulating substrates under vacuum pressure of ~ 6×10^{-7} Torr and deposition rates of ~ 0.01 Å/sec. High purity organic semiconducting source materials (~ 99.8%) were purified by repeated sublimations before they were used to grow films. All the TSM images and analysis were based on freshly grown ultrathin films.

Thermally grown 300 nm thick amorphous silicon dioxide overlayer on p-doped silicon wafers were used as silicon dioxide substrates. Polymeric substrates were prepared by spin coating the silicon dioxide substrates with 1 wt. % toluene solutions at 4000 rpm. The resulting polymer film thicknesses were approximately 40 nm in all cases. The substrates were then left to dry overnight at room temperature in an inert atmosphere. All the polymers were purchased from Aldrich Chemical Company: PS (M_w = 350 kg/mol), PAMS (M_w = 838 kg/mol), and PMMA (M_w = 996 kg/mol).

7.5 Acknowledgements

This work was partially supported by the MRSEC Program of the National Science Foundation under Award Number DMR-0819885. Partial support was also provided by NSF through DMR-0706011. Parts of this work were carried out in the Institute of Technology Characterization Facility, University of Minnesota, which received partial support from NSF through the NNIN and MRSEC programs. V. K.

thanks the University of Minnesota for support through a Doctoral Dissertation Fellowship. The authors also thank D. J. Ellison for help with the KFM experiments.

Chapter 8

Future Work

This chapter describes some of the unpublished results from my thesis work. It discusses two current projects. The first project is related to the friction studies of organic semiconductor single crystals and the second project investigates the TSM studies of thin films of crystalline semiconducting polymers.

8.1 Friction Studies of Organic Semiconductor Single Crystals

Organic semiconductor single crystals are known to have anisotropic charge mobilities, *i.e.*, different charge carrier mobilities along different crystallographic directions.[125,126] It is not surprising because of the presence of anisotropic bonding that holds the molecules together in organic solids.[36] Due to the absence of complex microstructure, single crystals offer clear advantages over thin films for charge transport studies. The absence of grain boundaries makes it relatively simpler to correlate charge transport and anisotropic bonding. Yet, even the surface of single crystals can be less than ideal for charge transport studies because of the presence of defects, for example, step edges and line dislocations. However, organic semiconductor single crystals are extensively studied with the long term goal of elucidating the role of molecular structure and crystal packing on electrical transport.[125125]

As discussed in Chapter 3, friction measured from FFM experiments can be quantitatively related to the energy dissipation at the tip-sample interface. It is commonly believed that more available modes of energy dissipation should result in higher friction.[85] In a crystalline system, one of the modes of energy dissipation can be inter molecular vibration modes or lattice phonons, which can also impact charge transport through electron-phonon coupling. A stronger bonding or interaction between the molecules should result in less lattice vibration and *vice versa*. In an attempt to correlate charge carrier mobility and bonding anisotropy, we performed FFM and hole mobility measurements on pentacene single crystals.

Figures 8.1A and 8.1B show tensor plots of inverse normalized friction (measured by FFM) and hole mobilities (measured from single crystal air gap transistors) as a function of pentacene crystallographic direction. The plots demonstrate that both the quantities are anisotropic exhibiting maxima and minima. However, the most interesting observation is that both the plots trace each other. Specifically, the plots demonstrate that along pentacene $[\bar{1}10]$ one gets lowest friction and highest hole mobility. Whereas, along [110] one gets highest friction and lowest hole mobility. This observation indicates that there is a possible relation between the friction and the charge carrier mobility measurements in pentacene single crystals.

We postulate that bonding anisotropy is the cause of the observed anisotropy in friction and charge mobility measurements. A stronger bonding along $[\bar{1}10]$ not only results in higher hole mobility, but also results in less lattice phonons. On the other hand, along pentacene [110] a relatively weaker bonding results in lower hole mobility but more lattice phonons. Another possible explanation can be the preferential presence of structural defects along a crystallographic direction because the structural defects can

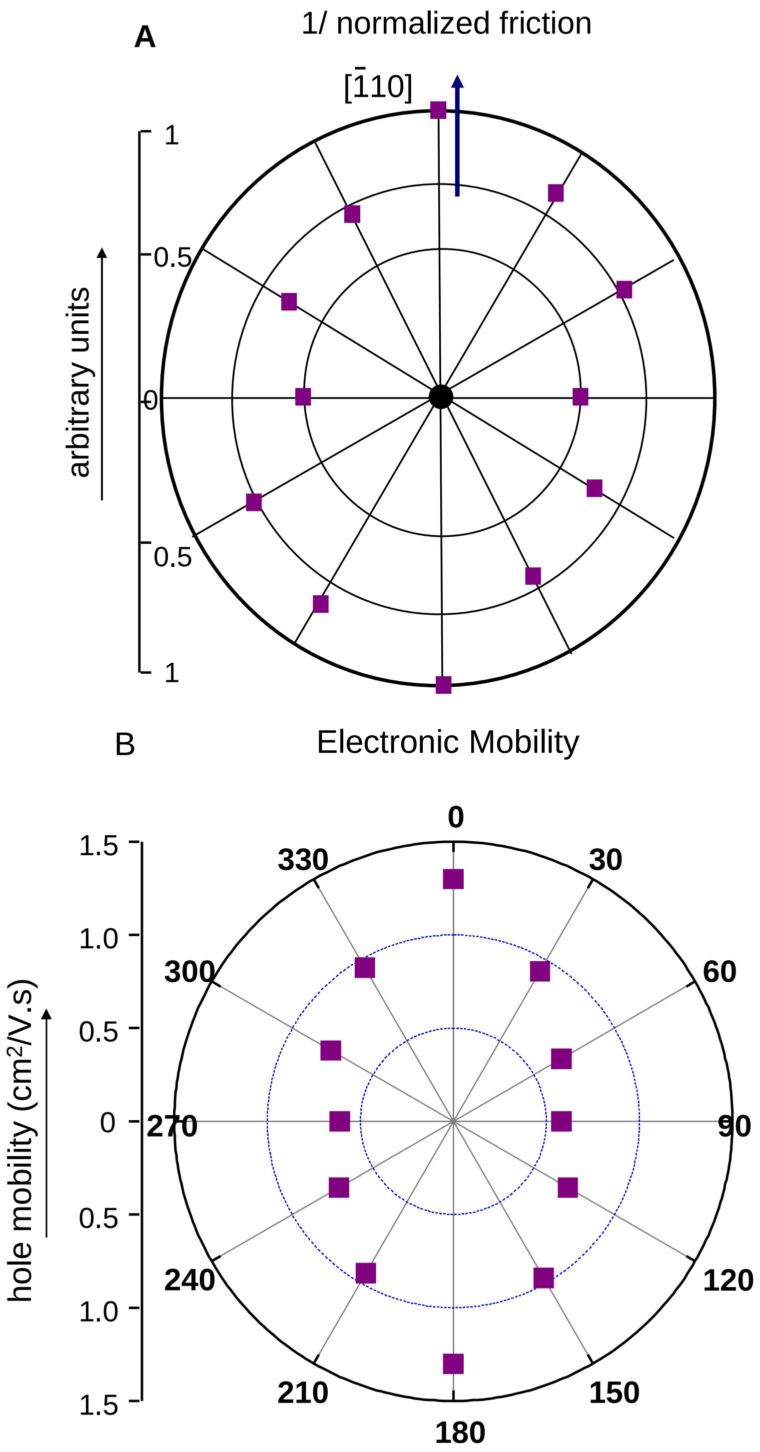

Figure 8.1 Tensor plots for Inverse Friction and Hole Mobility in Pentacene Single Crystal A) A tensor plot shows inverse of normalized friction as a function of pentacene crystallographic orientation. B) A tensor plot shows hole mobility as a function of pentacene crystallographic orientation. Both the tensors trace each other.

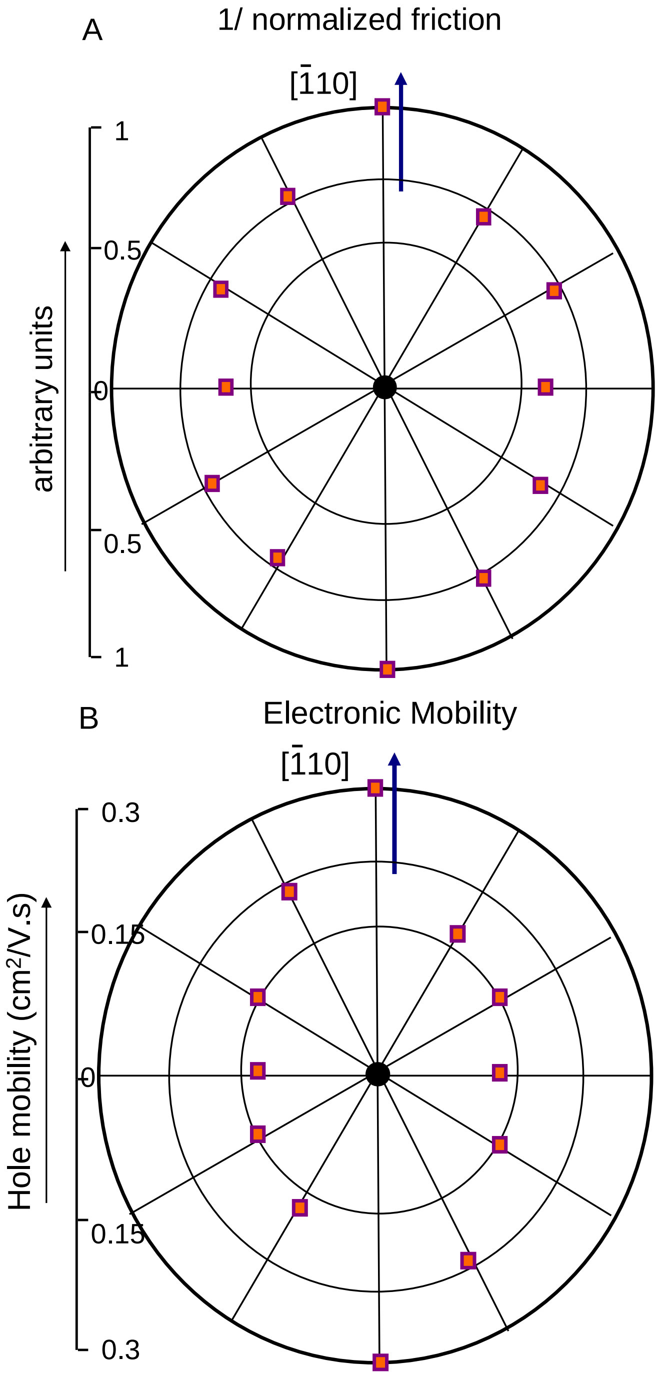

Figure 8.2 Tensor plots for Inverse Friction and Hole Mobility in Tetracene Single Crystal A) A tensor plot shows inverse of normalized friction as a function of tetracene crystallographic orientation. B) A tensor plot shows hole mobility as a function of tetracene crystallographic orientation. Both the tensors trace each other.

affect both the charge carrier mobility and the measured friction in FFM experiments (for more detail see Chapter 3). In order to check the validity of our hypothesis, we performed similar hole mobility and friction experiments on tetracene single crystals (Fig. 8.2), as the molecular structure and crystal packing of pentacene and tetracene are identical. Figures 8.2A and 8.2B show tensor plots of inverse normalized friction and hole mobilities as a function of tetracene crystallographic directions. Both the tensor plots of tetracene look similar to the corresponding plots of pentacene. More importantly, like in pentacene, the two plots trace each other.

Similar measurements were performed on rubrene single crystals, but no friction anisotropy was observed (although rubrene shows anisotropy in charge carrier mobility). The difference between rubrene and pentacene (or tetracene) measurements can be related to their different molecular structures and crystal packing. Pentacene and tetracene are planar molecules with no side groups and thus show some extent of flexibility in their packing. Whereas, rubrene has side groups which leads to interlocked packing, *i.e.*, the molecules are locked up at their respective positions. The extent of mobility of molecules in their respective solid state packings can be the reason behind different results for rubrene and pentacene. In order to understand the above behavior, we are currently investigating the phononic or inter molecular modes as a function of crystallographic direction on various single crystals using polarized Raman scattering.

8.2 TSM Studies of Crystalline Semiconducting Polymer Thin Films

Small molecule and polymer semiconductors are the two classes of organic semiconductors that are widely used in organic electronics.[36] Although significant

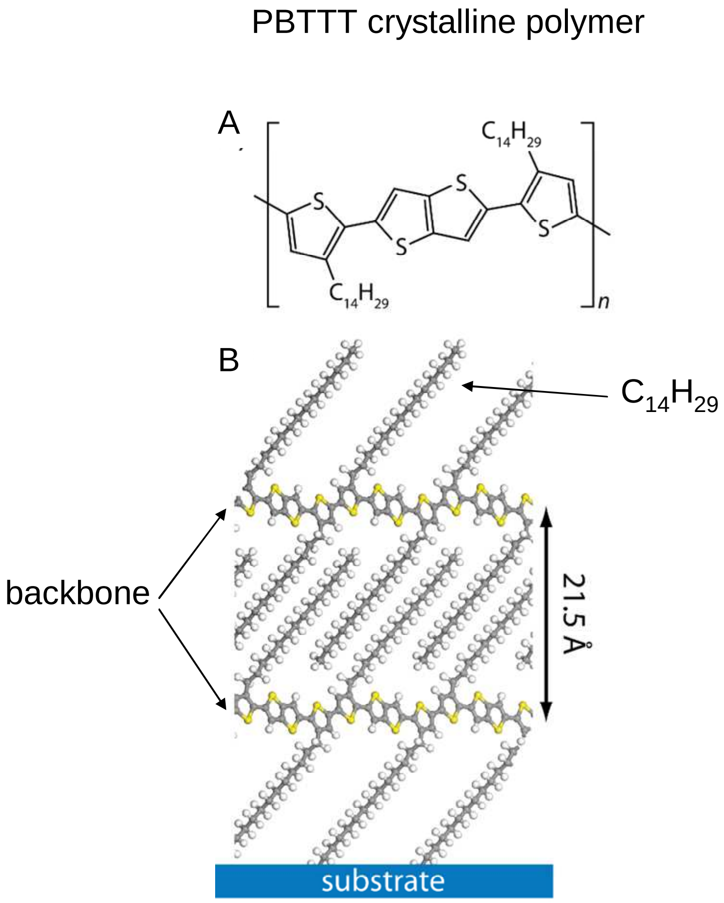

Figure 8.3 PBTTT A) Chemical structure, and B) Thin film packing.

progress has been made to improve the performance of solution-deposited small molecules, polymers offer significant advantages in terms of solution rheology and mechanical properties. Poly(2,5-bis(3-alkylthiophen-2-yl)thieno[3,2-b]thiophene), or PBTTT, is an example of polymer semiconductor which forms crystalline films.[226] Figures 8.3A and 8.3B show the chemical structure and thin film packing of PBTTT, respectively.

In order to investigate the applicability of TSM for polymers, we tried TSM on crystalline films of PBTTT. Ideally, TSM should work on any crystalline system with elastic anisotropy. Crystalline polymers, like any other polymer, exhibit significant mechanical anisotropy. For example, the mechanical modulus along the polymer backbone is usually bigger than the perpendicular modulus.

Figure 8.4 shows height and corresponding TSM trace and retrace images of PBTTT crystalline films. The height image demonstrates that the morphology is not rough and is terraced, indicating presence of crystalline domains. Simultaneously acquired TSM trace and retrace scans does not look as clear as those obtained for polycrystalline pentacene thin films. The possible reason for unclear TSM images can be the big side groups attached to the backbone of the polymer (Fig. 8.3A). During the TSM experiment, the AFM tip probes the side groups and not the polymer backbone, as evident in the PBTTT thin film packing structure shown in Fig. 8.3B. The side groups attached to the backbone are relatively compliant with respect to the backbone and do not offer enough resistance to the motion of the AFM tip. As a result, the TSM signal is weak and the images look unclear. However, some patches of the TSM images show good

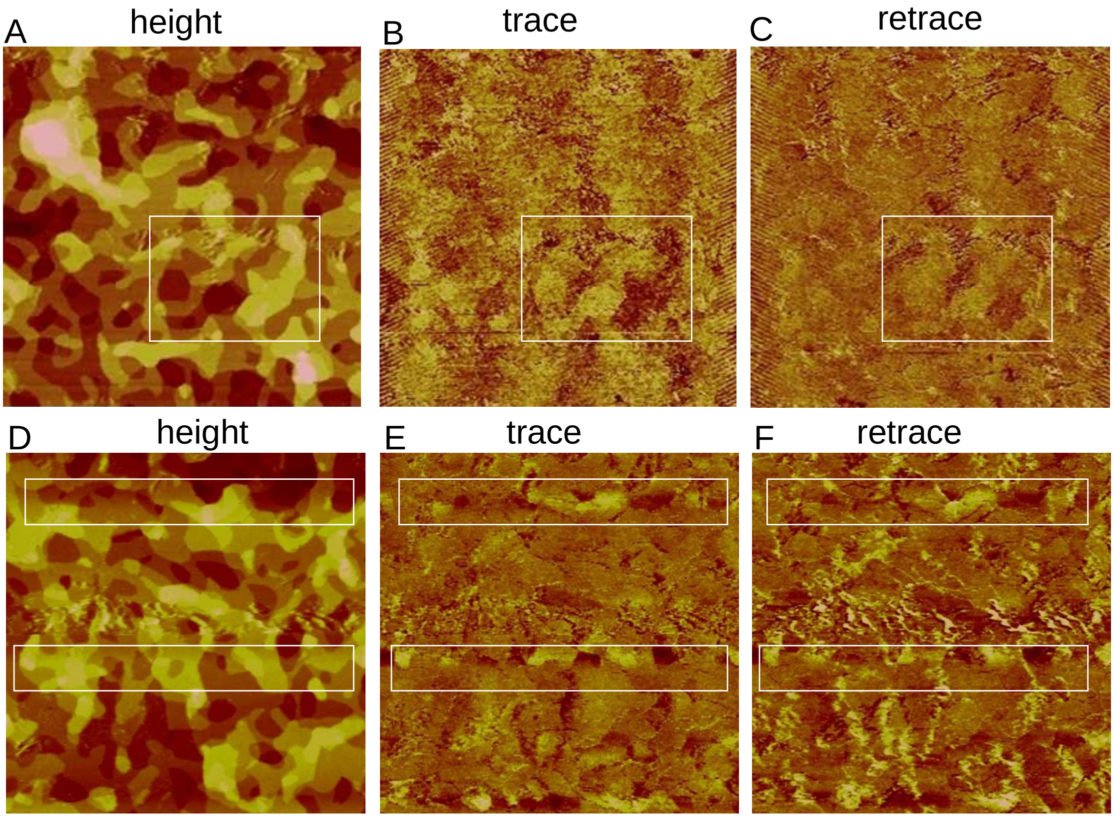

Figure 8.4 TSM of PBTTT crystalline polymer thin films Height and corresponding TSM trace and retrace images.

contrast revealing different crystalline domains on the polymer surface. We are in the process of optimizing the imaging parameters in order to get a clear TSM image. One possible way to get a good polymer TSM image might be to image at lower temperatures. Lower temperatures should lower the mobility of polymer side chains and then the chains would offer more resistance to the AFM tip motion.

Two critical observations from the TSM images shown in Fig. 8.4 are as follows:

1) Careful inspection of the trace and retrace images reveals that the trace signal is same as the retrace signal. This is not expected because one normally gets opposite signals from trace and retrace scans, as seen in case of small molecule crystalline thin films.[30,32] We suspect that the orientation of the side chains at the polymer surface is changing while probing it with AFM tip. This means that the tip is seeing different orientations of side chains during trace and retrace scans.
2) The TSM signal from one terrace is different from the other terrace and there is no signal variation with in a single terrace. This is an interesting observation because it indicates that the side group orientation is different on different terraces, but side groups maintaining one orientation within a terrace. It means that there are also grain boundaries in a plane perpendicular to the substrate surface.

References

---

[1] M. L. Chabinyc and A. Salleo, *Chemistry of Materials*, **16** 4509 (2004)

[2] H. Hoppe and N. S. Sariciftci, *Journal of Materials Research*, **19** 1924 (2004)

[3] P. F. Baude, D. A. Ender, M. A. Haase, T. W. Kelley, D. V. Muyres, and S. D. Theiss, *Applied Physics Letters*, **82** 3964 (2003)

[4] M. L. Chabinyc, W. S. Wong, A. C. Arias, S. Ready, R. A. Lujan, J. H. Daniel, B. Krusor, R. B. Apte, A. Salleo, and R. A. Street, *Proceedings of the IEEE*, **93** 1491 (2005)

[5] T. W. Kelley, P. F. Baude, C. Gerlach, D. E. Ender, D. Muyres, M. A. Haase, D. E. Vogel, and S. D. Theiss, *Chemistry of Materials*, **16** 4413 (2004)

[6] H. Sirringhaus, P. J. Brown, R. H. Friend, M. M. Nielsen, K. Bechgaard, B. M. W. Langeveld-Voss, A. J. H. Spiering, R. A. J. Janssen, E. W. Meijer, P. Herwig, D. M. De Leeuw, *Nature*, **401** 685 (1999)

[7] A. R. Murphy, P. C. Chang, P. VanDyke, J. Liu, J. M. J. Frechet, V. Subramanian, D. M. DeLongchamp, S. Sambasivan, D. A. Fischer, E. K. Lin. *Chem. Mater.*, **17(24)** 6033 (2005)

[8] S. Y. Yang, K. Shin, C. E. Park, *Adv. Funct. Mater.*, **15** 1806 (2005)

[9] C. D. Dimitrakopoulos, P. R. L. Malenfant, *Adv. Mater.*, **14(2)**, 99 (2002)

[10] L. L. Chua, K. H. Peter, H. Sirringhaus, R. H. Friend, *Adv. Mater.*, **16(18)** 1609 (2004)

[11] D. J. Gundlach, J. E. Royer, S. K. Park, S. Subramanian, O. D. Jurchescu, B. H. Hamadani, A. J. Moad, R. J. Kline, L. C. Teague, O. Kirillov, C. A. Richter, J. G. Kushmerick, L. J. Richter, S. R. Parkin, T. N. Jackson, J. E. Anthony, *Nat. Mater.*, **7(3)** 216 (2008)

[12] S. J. Jo, C. S. Kim, M. J. Lee, J. B. Kim, S. Y. Ryu, J. H. Noh, K. Ihm, H. K. Baik, Y. S. Kim, *Adv. Mater.*, **20(6)** 1146 (2008)

[13] M. L. Tang, A. D. Reichardt, N. Miyaki, R. M. Stoltenberg, Z. Bao, *J. Am. Chem. Soc.*, **130(19)** 6064 (2008)

[14] E. L. Granstrom, C. D. Frisbie, *J. Phys. Chem.*, **103** 8842 (1999)

[15] F. Dinelli, M. Murgia, P. Levy, M. Cavallini, F. Biscarini, *Phys. Rev. Lett.***, 92** 116802 (2004)

[16] P. Peumans, S. Uchida, S. R. Forrest, *Nature***, 425** 158 (2003)

[17] J. Kido, M. Kimura, K. Nagai, *Science***, 267** 1332 (1995)

[18] S. E. Fritz, S. M. Martin, C. D. Frisbie, M. D. Ward, M. F. Toney, *J. Am. Chem. Soc.***, 126(13)** 4084 (2004)

[19] R. Ruiz, B. Nickel, N. Koch, L. C. Feldman, R. F. Haglund, A. Kahn, G. Scoles, *Phys. Rev. B***, 67** 125406 (2003)

[20] J. Rivnay, L. H. Jimison, J. E. Northrup, M. F. Toney, R. Noriega, S. Lu, T. J. Marks, A. Facchetti, A. Salleo, *Nat. Mater.***, 8(12)** 952 (2009)

[21] S. C. B. Mannsfeld, A. Virkar, C. Reese, M. F. Toney, Z. Bao, *Adv. Mater.***, 21(22)** 2294 (2009)

[22] F-J. M. zu Heringdorf, M. C. Ruter, B. M. Tromp, *Nature***, 412** 517 (2001)

[23] L. F. Drummy, C. Kubel, L. Christian, A. White, D. C. Martin, *Adv. Mat.***, 14(1)** 54 (2002)

[24] A. Al-Mahboob, J. T. Sadowski, Y. Fujikawa, K. Nakajima, T. Sakurai, *Phys. Rev. B: Condens. Matter & Mat. Phys.***, 77** 035426 (2008)

[25] R. Ruiz, B. Nickel, N. Koch, L. C. Feldman, R. F. Haglund, A. Kahn, F. Family, G. Scoles, *Phys. Rev. Lett.***, 91** 136102 (2003)

[26] S. Pratontep, F. Nuesch, L. Zuppiroli, M. Brinkmann, *Phys. Rev. B***, 72** 085211 (2005)

[27] B. Stadlober, U. Haas, H. Maresch, and A. Haase, *Phys. Rev. B***, 74** 165302 (2006)

[28] C. Kim, A. Facchetti, T. J. Marks, *Science***, 318** 76 (2007)

[29] P. R. Ribic, V. Kalihari, C. D. Frisbie, G. Bratina, *Phys. Rev. B***, 80** 115307 (2009)

[30] K. Puntambekar, J. Dong, G. Haugstad, C. D. Frisbie, *Adv. Funct. Mater.***, 16** 879 (2006)

[31] J. Zhang, J. P. Rabe, N. Koch, *Adv. Mater.***, 20** 3254 (2008)

[32] V. Kalihari, E. B. Tadmor, G. Haugstad, C. D. Frisbie, *Adv. Mater.***, 20** 4033 (2008)

[33] V. Kalihari, D. J. Ellison, G. Haugstad, C. D. Frisbie, *Adv. Mater.***, 21** 3092 (2009)

[34] V. Kalihari, G. Haugstad, C. D. Frisbie, *Phys. Rev. Lett.***, 104(8)** 086102 (2010)

[35] J. L. Bredas, J. P. Calbert, D. A. da Silva Filho, and J. Cornill, *Proceedings of the National Academy of Science*, **99** 5804-5809 (2002)

[36] M. Pope and C. E. Swenberg, *Electronic Processes in Organic Crystals and Polymers*, 2nd ed. (Oxford University Press, New York, 1999)

[37] M. D. Curtis, J. Cao, and J. W. Kampf*, J. Am. Chem. Soc.,* **126** 4318 (2004)

[38] P. Pesavento, Ph. D. Thesis, University of Minnesota, (2005)

[39] D. Holmes, S. Kumaraswamy, A. J. Matzger, and K. P. C. Vollhardt, *Chem. Eur. J.*, **5** 3399 (1999)

[40] A. J. Lovinger, D. D. Davis, A. Dodabalapur, and H. E. Katz, *Chem. Mater.*, **8** 2836 (1996)

[41] T. M. Pappenfus, J. D. Raff, E. J. Hukkanen, J. R. Burney, J. Casado, S. M. Drew, L. L. Miller, and K. R. Mann*, Journal of Organic Chemistry,* **67** 6015 (2002)

[42] E. Haedicke and F. Graser, *Acta Crystallographica, Section C: Crystal Structure Communications* **C42,** 189 (1986)

[43] Milton Ohring, *Materials Science of Thin Films*, 2nd edition. (Academic Press, 2002)

[44] R. Kern, G. Le Lay and J.J. Metois, *Current topics in Materials Science*, **3** 139 (1979)

[45] J.G. Amar and F. Family, *Physical Review Letters*, **74** 2066 (1994)

[46] K.L. Chopra, *Thin Film Phenomena*, (McGraw Hill, 1969)

[47] Faktor and Garrett, *Growth of Crystals from the Vapor*, (Chapman and Hall, 1974)

[48] J.A. Venables, G.D.T. Spiller and M. Hanbucken, *Rep. Prog. Phys.*, **47** 399 (1984)

[49] P.A. Mulheran and J.A. Blackman, *Physical Review B*, **53** 10261 (1996)

[50] P.A. Mulheran and J.A. Blackman, *Philosophical Magazine Letters*, **72** 55 (1995)

[51] http://www.smart.tii.se/smart/events/events2003_se.php

[52] T.A. Witten and L.M. Sander, *Physical Review Letters*, **47** 1400 (1981)

[53] P. Jensen, A. Barabasi, H. Larralde, S. Havlin and H.E. Stanley, *Physical review B*, **50** 15316 (1994)

[54] R.C. Ball, R.M. Brady, G. Rossi and B.R. Thompson, *Physical Review Letters*, **55** 1406 (1985)

[55] T.C. Chang, I.S. Hwang and T.T. Tsong, *Physical Review Letters*, **83** 1191 (1999)

[56] J. Beben, I.S. Hwang, T.C. Chang and T.T. Tsong, *Physical Review B*, **63** (2000)

[57] W. D. Callister, *Materials Science and Engineering: An Introduction*, (fifth Edition, John Wiley and Sons Inc New York)

[58] http://en.wikipedia.org/wiki/Dislocation

[59] M. Hawley, I. D. Raistrick, J. G. Beery and R. J. Houlton, *Science*, **251** 1587 (1991)

[60] G. Springholz, A.Y. Ueta, N. Frank and G. Bauer, *Applied Physics Letters*, **69** 2821 (1996)

[61] A.R. Verma, *Nature*, **168** 783 (1951)

[62] http://www.minsocam.org/msa/collectors_corner/arc/screwdis.htm

[63] G. Witte and C. Woll, *J. Mater. Res.*, **19** 1889 (2004)

[64] A. C. Durr, F. Schreiber, M. Kelsch, H.D. Carstanjen, and H. Dosch, *Advanced Materials*, **14** 961 (2002)

[65] A. C. Durr, F. Schreiber, M. Munch, N. Karl, B. Krause, V. Kruppa and H. Dosch, *Applied Physics Letters*, **81** 2276 (2002)

[66] T. Ogawa, K. Kuwamoto, S. Isoda, T. Kobayashi and N. Karl, *Acta Crystallogr. B*, **55** 123 (1999)

[67] Y. Y. Lin, D. Gundlach, S. Nelson and T. Jackson, *IEEE Electron Device Letters*, **18** 87 (1997)

[68] R. B. Campbell, J. M. Robertson and J. Trotter, *Acta Cryst.* , **14** 705 (1961)

[69] C. D. Dimitrakopoulos, A. R. Brown and A. J. Pomp, *Journal of Applied Physics*, **80** 2501 (1996)

[70] S. Pratontep, M. Brinkmann, F. Nuesch and L. Zuppiroli, *Synthetic Metals*, **146** 387 (2004)

[71] S. Pratontep and M. Brinkmann, *Physical Review B*, **69** 165201 (2004)

[72] I. P. Bouchoms, W. A. Schoonveld, J. Vrijmoeth and T. M. Klapwijk, *Synthetic Metals*, **104** 175 (1999)

[73] T. Jentzsch, H. J. Juepner, K. W. Brzezinka and A. Lau, *Thin Solid Films*, **315** 273 (1998)

[74] D. Knipp, R. A. Street and A. R. Volkel, *Applied Physics Letters*, **82** 3907 (2003)

[75] R. Ruiz, D. Choudhary, B. Nickel, T. Toccoli, K. Chang, A.C. Mayer, P. Clancy, J.M. Blakely, R. L. Headrick, S. Iannotta and G. Malliaras, *Chem. Mater.*, **16** 4497 (2004)

[76] P. Guaino, D. Carty, G. Hughes, P. Moriarty and A. A. Cafolla, *Appl. Surf. Sci.*, **212** (2003)

[77] D. Choudhary, P. Clancy, R. Shetty and F. Escobedo, *Advanced Functional Materials*, **16** 1768 (2006)

[78] S. Lukas, G. Witte and C. Woll, *Physical Review Letters*, **88** 028301 (2002)

[79] B. Nickel, R. Barabash, R. Ruiz, N. Koch, A. Kahn, L. C. Feldman, R. F. Haglund and G. Scoles, *Physical Review B*, **70** 125401 (2004)

[80] P. J. Plau, *Friction Science and Technology*, (New York: Dekker) (1996)

[81] www.engineershandbook.com/Tables/frictioncoefficients.htm

[82] D. Tabor and R. Winterton, *Proceedings of the Royal Society London*, **A312** 435 (1969)

[83] J. N. Israelachvili and D. Tabor, *Proceedings of the Royal Society London*, **A331** 19 (1972)

[84] http://www.molec.com/what_is_afm.html

[85] R. W. Carpick and M. Salmeron, *Chemical Reviews*, **97** 1163 (1997)

[86] K. Puntambekar, Ph.D Thesis, University of Minnesota, (2006)

[87] G. Meyer and N. M. Amer, *Applied Physics Letters,* **57** 2089 (1990)

[88] D. F. Ogletree, R. W. Carpick, and M. Salmeron, *Review of Scientific Instruments,* **67** 3298 (1996)

[89] G. Haugstad, Course notes (Chem 5210, Materials Characterization)

[90] R. M. Overney, E. Meyer, J. Frommer, D. Brodbeck, R. Luethi, L. Howald, H. J. Guentherodt, M. Fujihira, H. Takano, and Y. Gotoh, *Nature*, **359** 133 (1992)

[91] C. D. Frisbie, L. F. Rozsnyai, A. Noy, M. S. Wrighton, and C. M. Lieber, *Science*, **265** 2071 (1994)

[92] R. W. Carpick, Q. Dai, D. F. Ogletree, and M. Salmeron, *Tribology Letters,* **5** 91 (1998)

[93] M. Liley, D. Gourdon, D. Stamou, U. Meseth, T. M. Fischer, C. Lautz, H. Stahlberg, H. Vogel, N. A. Burnham, and C. Duschl, *Science*, **280** 273 (1998)

[94] C. M. Mate, G. M. McClelland, R. Erlandsson and S. Chiang, *Physical Review Letters*, **59** 1942 (1987)

[95] G. J. Germann, S. R. Cohen, G. Neubauer, G. M. Mcclelland, H. Seki and D. Coulman, *Journal of Applied Physics*, **73** 163 (1993)

[96] S. Morita, S. Fujisawa, Y. Sugawara, *Surface Science Reports*, **23** 3 (1996)

[97] H. Takano and M. Fujihara, *Journal of Vacuum Science Technology B*, **14** 1272 (1996)

[98] G. A. Tomilson, *Philosophical Magazine*, **7** 905 (1929)

[99] J. B. Sokoloff, *Physical Review Letters*, **71** 3450 (1993)

[100] J. B. Sokoloff, *Physical Review B*, **52** 7205 (1995)

[101] J. Colchero, A. M. Baro and O. Marti, *Tribology Letters*, **2** 327 (1996)

[102] E. Reido, E. Gnecco, R. Bennewitz, E. Meyer and H. Brune, *Physical Review Letters*, **91** 8 (2003)

[103] A. E. Filippov, J. Klafter and M. Urbakh, *Physical Review Letters*, **92** 13 (2004)

[104] M. Evstigneev, A. Schirmeisen, L. Jansen, H. Fuchs and P. Reimann, *Physical Review Letters*, **97** (2006)

[105] M. Evstigneev and P. Reimann, *Physical Review B*, **73** 113401 (2006)

[106] A. Marti, G. Hahner and N. D. Spencer, *Langmuir*, **11** 4632 (1994)

[107] R. M. Overney, E. Meyer, J. Frommer and H. J. Guntherodt, *Langmuir,* **10** 1281 (1994)

[108] R. McKendry, M.E. Theoclitou, T. Rayment and C. Abell, *Nature*, **391** 566 (1998)

[109] X. Xiao, J. Hu, D. H. Charych and M. Salmeron, *Langmuir*, **12** 235 (1996)

[110] G. H. Haugstad and W. L. A. Gladfelter, *Interfacial properties on the Submicron scale*, (ACS Books 2001)

[111] H. Bluhm, U. D. Schwarz, K. P. Meyer and R. Wiesendanger, *Applied Physics A*, **61** 525 (1995)

[112] H. Schonherr, P. J. A. Kenis, J. F. J. Engbersen, S. Harkema, R. Hulst, D. N. Reinhoudt and G. J. Vansco, *Langmuir*, **14** 2801 (1998)

[113] R. M. Overney, H. Takano, M. Fujihara, W. Paulus and H. Ringsdorf, *Physical Review Letters*, **72** 3546 (1994)

[114] M. R. Falvo, J. Syeele, R. M. Taylor and R. Superfine, *Tribology Letters*, **9** 73 (2000)

[115] M. Hirano, K. Shinjo, R. Kaneko and Y. Murata, *Physical Review Letters,* **67** 2642 (1991)

[116] J. Y. Park, D. F. Ogletree, M. Salmeron, R. A. Rebeiro, P. C. Canfield, C. J. Jenks and P. A. Thiel, *Science,* **309** 1354 (2005)

[117] J. A. Last and M. D. Ward, *Advanced Materials,* **8** 730 (1996)

[118] C. M. Mate et al., Phys. Rev. Lett. **59,** 1942 (1987)

[119] B. Bhushan, *Introduction to Tribology,* (John Wiley & Sons, New York, 2002)

[120] E. Barrena et al., *Phys. Rev. Lett.,* **82** 2880 (1999)

[121] J. A. Hammerschmidt, W. L. Gladfelter, and G. Haugstad, *Macromolecules,* **32** 3360 (1999)

[122] S. Sills and R. M. Overney, *Phys. Rev. Lett.,* **91** 095501 (2003)

[123] D. J. Gundlach et al., *IEEE Elec. Dev. Lett.*, **18** 87 (1997)

[124] A. Dodabalapur, L. Torsi, and H. E. Katz, *Science*, **268** 270 (1995)

[125] V. C. Sundar et al., *Science*, **303** 1644 (2004)

[126] J. Y. Lee, S. Roth, and Y. W. Park, *Appl. Phys. Lett*., **88** 252106 (2006)

[127] Z. Tshiprut, S. Zelner, and M. Urbakh, *Phys. Rev. Lett.*, **102** 136102 (2009)

[128] D. B. Knorr, T. O. Gray, and R. M. Overney, *J. Chem. Phys.*, **129** 074504 (2008)

[129] E. Gnecco et al., *Phys. Rev. Lett.*, **84** 1172 (2000)

[130] J. D. Ferry, *Viscoelastic Properties of Polymers* (John Wiley & Sons, New York, 1980)

[131] F. Dinelli, C. Buenviaje, and R. M. Overney, *J. Chem. Phys*., **113** 2043 (2000)

[132] G. Haugstad et al., *Langmuir*, **11** 3473 (1995)

[133] P. L. Gould, *Introduction to Linear Elasticity*, (Springer-Verlag, New York, 1983)

[134] H. B. Huntington, S. G. Gangoli, and J. L. Mills, *J. Chem. Phys.*, **50** 3844 (1969)

[135] M. Schwoerer, H. C. Wolf, *Organic Molecular Solids*, Wiley, Weinheim (2007)

[136] H. Klauk, *Organic Electronics*, Wiley, Weinheim (2006**)**

[137] S. R. Forrest, *Nature***, 428** 911 (2004)

[138] N. Karl, *Synth. Met.***, 133** 649 (2003)

[139] P. M. Borsenberger, L. T. Pautmeier, H. Bassler, *Phys. Rev. B: Condens. Matter & Mater. Phys.***, 48(5)** 3066 (1993)

[140] T. W. Kelley, C. D. Frisbie, *J. Phys. Chem. B***, 105** 4538 (2001)

[141] E. M. Muller, J. A. Marohn, *Adv. Mater.***, 17(11)** 1410 (2005)

[142] H. L. Cheng, Y. S. Mai, W. Y. Chou, L. R. Chang, X. W. Liang, *Adv. Funct. Mater.***,** **17** 3639 (2007)

[143] G. Horowitz, M. E. Hajlaoui, *Adv. Mater.***,** **12(14)** 1046 (2000)

[144] R. J. Kline, M. D. McGehee, M. F. Toney, *Nat. Mater.***,** **5(3)** 222 (2006)

[145] A. C. Mayer, A. Kazimirov, G. G. Malliaras, *Phys. Rev. Lett.***,** **97(10)** 105503 (2006)

[146] L. Casalis, M. F. Danisman, B. Nickel, G. Bracco, T. Toccoli, S. Iannotta, G. Scoles, *Phys. Rev. Lett.***,** **90(20)** 206101 (2003)

[147] X. L. Chen, A. J. Lovinger, Z. Bao, J. Sapjeta, *Chem. Mater.***,** **13(4)** 1341 (2001)

[148] R. Jaeger, H. Schonherr, G. J. Vancso, *Macromolecules***,** **29** 7634 (1996)

[149] R. W. Carpick, D. Y. Sasaki, M. S. Marcus, M. A. Eriksson, A. R. Burns, *J. Phys.: Condens. Matter***,** **16** R679 (2004)

[150] R. W. Carpick, D. Y. Sasaki, A. R. Burns, *Tribol. Lett.***,** **7** 79 (1999)

[151] G. Horowitz, *Adv. Mater.***,** **10** 365 (1998)

[152] J. Cornil, J. P. Calbert, J. L. Bredas, *J. Am. Chem. Soc.***,** **123** 1250 (2001)

[153] R. Ruiz, A. Papadimitratos, A. C. Mayer, G. G. Malliaras, *Adv. Mater.***,** **17** 1795 (2005)

[154] G. S. Pawley, *Phys. Stat. Sol.***,** **20** 347 (1967)

[155] J. Y. Lee, S. Roth, Y. W. Park, *Appl. Phys. Lett.***,** **88** 252106 (2006)

[156] S. Weng, W. Hu, C. Kuo, Y. Tao, L. Fan, Y. Yang, *Appl. Phys. Lett.***,** **89** 172103 (2006)

[157] G. Kaupp, J. Schmeyers, U. D. Hangen, *J. Phys. Org. Chem.***,** **15** 307 (2002)

[158] K. Yamanaka, E. Tomita, *Jpn. J. Appl. Phys.***,** **34(5B)** 2879 (1995)

[159] J. Colchero, M. Luna, A. M. Baro, *Appl. Phys. Lett.***,** **68(20)** 2896 (1996)

[160] R. W. Carpick, D. F. Ogletree, M. Salmeron, *Appl. Phys. Lett.***,** **70(12)** 1548 (1997)

[161] S. Ge, Y. Pu, W. Zhang, M. Rafailovich, J. Sokolov, C. Buenviaje, R. Buckmaster, R. M. Overney, *Phys. Rev. Lett.***,** **85** 2340 (2000)

[162] A. Bolognesi, M. Berliocchi, M. Manenti, A. D. Carlo, P. Lugli, K. Lmimouni, C. Dufour. *IEEE Transactions on Electron Devices***,** **51** 1997 (2004)

[163] S.Verlaak, V. Arkhipov, P. Heremans, *Appl. Phys. Lett.***,** **82(5)** 745 (2003)

[164] P. E. J. Flewitt, R. K. Wild, *Grain Boundaries: Their Microstructure and Chemistry*, Wiley, New York (2001)

[165] J. A. Venables, *Introduction to Surface and Thin Film Processes*, Cambridge Univ. Press, Cambridge (2005)

[166] S. Verlaak, S. Steudel, P. Heremans, D. Janssen, M. S. Deleuze, *Phys. Rev. B: Condens. Matter & Mater. Phys.***,** **68** 195409 (2003)

[167] G. Haugstad, *Trib. Lett.***,** **19** 49 (2005)

[168] Q. Li, S. Kim, A. Rydberg, *Rev. Sci. Instrum.***,** **77** 065105 (2006)

[169] G. Gelinck, *Nature***,** **445** 268 (2007)

[170] M. E. Roberts, S. C. B. Mannsfeld, M. L. Tang, Z. Bao. *Chem. Mater.***,** **20(23)** 7332 (2008)

[171] R. A. Street, J. E. Northrup, A. Salleo, *Phys. Rev. B.***,** **71** 165202 (2005)

[172] R. J. Kline, M. D. McGehee, E. N. Kadnikova, J. Liu, J. M. J. Frechet, *Adv. Mater.***,** **15(18)** 1519 (2003)

[173] M. Cavallini, P. Stoliar, J.-F. Moulin, M. Surin, P. Leclere, R. Lazzaroni, D. W. Breiby, J. W. Andreasen, M. M. Nielsen, P. Sonar, A. C. Grimsdale, K. Mullen, F. Biscarini, *Nano Lett.***,** **5(12)** 2422 (2005)

[174] A. Bolognesi, M. Berliocchi, M. Manenti, A. D. Carlo, P. Lugli, K. Lmimouni, C. Dufour, *IEEE Transactions on Electron Devices***,** **51(12)** 1997 (2004)

[175] E. M. Muller, J. A. Marohn, *Adv. Mater.***,** **17** 1410 (2005)

[176] D. Knipp, R. A. Street, A. R. Volkel, *Appl. Phys. Lett.***,** **82(22)** 3907 (2003)

[177] M. Tello, M. Chiesa, C. M. Duffy, H. Sirringhaus, *Adv. Funct. Mater.***,** **18** 3907 (2008)

[178] M. Jaquith, E. M. Muller, J. A. Marohn, *J. Phy. Chem. B***,** **111** 7711 (2007)

[179] L. Chen, O. Cherniavskaya, A. Shalek, L. E. Brus, *Nano Lett.***,** **5(11)** 2241 (2005)

[180] P. G. Evans, B. Park, S. Seo, J. Zwickey, I. In, P. Paoprasert, P. Gopalan, *Physica B***,** **401-402** 686 (2007)

[181] C. D. Dimitrakopoulos, S, Purushothaman, J. Kymissis, A. Callegari, J. M. Shaw, *Science*, **283** 822 (1999)

[182] K. J. Wan, X. F. Lin, J. Nogami, *Phys. Rev. B: Condens. Matter & Mater. Phys.***,** **47** 13700 (1993)

[183] M. Hanbucken, *Stress and Strain in Epitaxy: Theoretical Concepts, Measurements and Applications*, Elsevier, Amsterdam (2001)

[184] Q. L. Zhao, *J. Appl. Cryst.***,** **26** 243 (1993)

[185]T. Maeda, T. Kobayashi, T. Nemoto, S. Isoda, *Philos. Mag. B.***,** **81** 1659 (2001)

[186] T. Kobayashi, S. Isoda, *J. Mater. Chem.***,** **3** 1 (1993)

[187] X. Zhou, Z. Xie, Y. Wang, *Polymer***,** **42** 4709 (2001)

[188] D. E. Hooks, T. Fritz, M. D. Ward, *Adv. Mater.***,** **13(4)** 227 (2001)

[189] H. Yoshida, I. Katsuhiko, N. Sato, *Appl. Phys. Lett.***,** **90** 181930 (2007)

[190] L. Chen, R. Ludeke, X. Cui, A. G. Schrott, C. R. Kagan, L. E. Brus, *J. Phys. Chem. B***,** **109(5)** 1834 (2005)

[191] A. Nazarov, D. Thierry, *Electrochim. Acta***,** **52** 7689 (2007)

[192] W. Li, D. Y. Li, *Philos. Mag.***,** **84** 3717 (2004)

[193] W. Li, Y. Wang, D. Y. Li, *Phys. Stat. Sol.:A***,** **201** 2005 (2004)

[194] R. F. Greene, D. R. Frankl, J. Zemel, *Phys. Rev.***,** **118** 967 (1960)

[195] A. K. Ghosh, A. Rose, H. P. Maruska, D. J. Eustace,T. Feng. *Appl. Phys. Lett.***, 37(6)** 544 (1980)

[196] M. R. Murti, K. V. Reddy, *Phys. Stat. Sol.***, 119** 237 (1990)

[197] P. V. Pesavento, R. J. Chesterfield, C. R. Newman, C. D.Frisbie, *J. Appl. Phys.***, 96(12)** 7312 (2004)

[198] S. F. Nelson, Y. Y. Lin, D. J. Gundlach, T. N. Jackson, *Appl. Phys. Lett.***, 72(15)** 1854 (1998)

[199] M. Nonnenmacher, M. P. O'Boyle, H. K. Wickramasinghe, *Appl. Phys. Lett.***, 58** 2921 (1991)

[200] H. O. Jacobs, H. F. Knapp, S. Müller, A. Stemmer, *Ultramicroscopy***, 69** 39 (1997)

[201] M. Fujihira, *Annu. Rev. Mater. Sci.***, 29** 353 (1999)

[202] J. E. Stern, B. D. Terris, H. J. Mamin, D. Rugar, *Appl. Phys. Lett.***, 53** 2717 (1988)

[203] G. Binnig, C. F. Quate, C. Gerber, *Phys. Rev. Lett.***, 56** 930 (1986)

[204] S. E. Shaheen, D. S. Ginley, G. E. Jabbour, *Mater. Res. Soc. Bull.***, 30** 10 (2005)

[205]A. Dodabalapur, *Solid State Commun.***, 102(2)** 259 (1997)

[206] L. B. Freund, S. Suresh, *Thin Film Materials: Stress, Defect Formation and Surface Evolution*, University Press, Cambridge (2003)

[207] W. K. Liu, M. B. Santos, *Thin Films: Heteroepitaxial Systems*, World Scientific, Singapore (2003)

[208] M. M. Roberts, L. J. Klein, D. E. Savage, K. A. Slinker, M. Friesen, G. Celler, M. A. Eriksson, M. G. Lagally, *Nature Materials*, **5** 388 (2006)

[209] P. Fenter, F. Schreiber, L. Zhou, P. Eisenberger, S. R. Forrest, *Phys. Rev. B.,* **56(6)** 3046 (1997)

[210] D. Y. Zhong, M. Hirtz, W. C. Wang, R. F. Dou, L. F. Chi, H. Fuchs, *Phys. Rev. B*, **77** 113404 (2008)

[211] M. Schwoerer, H. C. Wolf, *Organic Molecular Solids*, Wiley, Weinheim (2007)

[212] W. Chen, H. Huang, A. Thye, S. Wee, *Chem. Commun.*, **36** 4276 (2008)

[213] S. Seo, P. G. Evans, *J. Appl. Phys.***, 106** 103521 (2009)

[214] A. Pimpinelli, J. Villain, *Physics of Crystal Growth*, University Press, Cambridge (1998)

[215] C. C. Mattheus, A. B. Dros, J. Baas, G. T. Oostergetel, A. Meetsma, J. L. de Boer, T. T. M. Palstra, *Synt. Met.***, 138** 475 (2003)

[216] A.-L. Deman, M. Erouel, D. Lallemand, M. Phaner-Goutorbe, P. Lang, J. Tardy, *J. Non-Crsytalline Solids*, **354** 1598 (2008)

[217] H. Yang, C. Yang, S. H. Kim, M. Jang, C. E. Park, *Applied Materials & Interfaces*, **2(2)** 391 (2010)

[218] H. Yang, S. H. Kim, L. Yang, S. Y. Yang, C. E. Park, *Adv. Mater.*, **19** 2868 (2007)

[219] S. M.A. Kazimi, *Solid Mechanics*, Tata McGraw-Hill, New Delhi (2008)

[220] D. Tahk, H. H. Lee, D-Y. Khang, *Macromolecules*, **42(18)** 7079 (2009)

[221] A. C. Mayer, R. Ruiz, R. L. Headrick, A. Kazimirov, G. G. Malliaras, *Organic Electronics*, **5(5)** 257 (2004)

[222] S. Kowarik, A. Gerlach, F. Schreiber, *J. Phys.: Condens. Matter*, **20** 184005 (2008)

[223] I. V. Markov, *Crystal Growth for Beginners*, World Scientific, Singapore (2003)

[224] F. Rohoullah, Z. Mansour, *THEOCHEM*, **862** 7 (2008)

[225] S. Chandrasekhar, *Liquid Crystals*, Cambridge University Press, Cambridge (1994)

[226] I. Mcculloch et al., *Nature Materials*, **5** 328 (2006)

Appendix A

Mechanical Model for Transverse Shear signal

(Contributing Authors: Vivek Kalihari, Greg Haugstad, C. Daniel Frisbie)
(Reprinted with permission from *Physical Review Letters* 104 (2010))

In this appendix, we describe a mechanical model describing the origin of transverse shear signal and its dependence on elastic anisotropy at the sample surface. We discuss various forces acting at a tip-sample interface and specifically, the force which gives rise to torque about the cantilever axis (*i.e.*, the origin of TSM signal) when the cantilever is scanning parallel to its long axis. Furthermore, we also check the validity of the mechanical model by comparing it with our experimental findings.

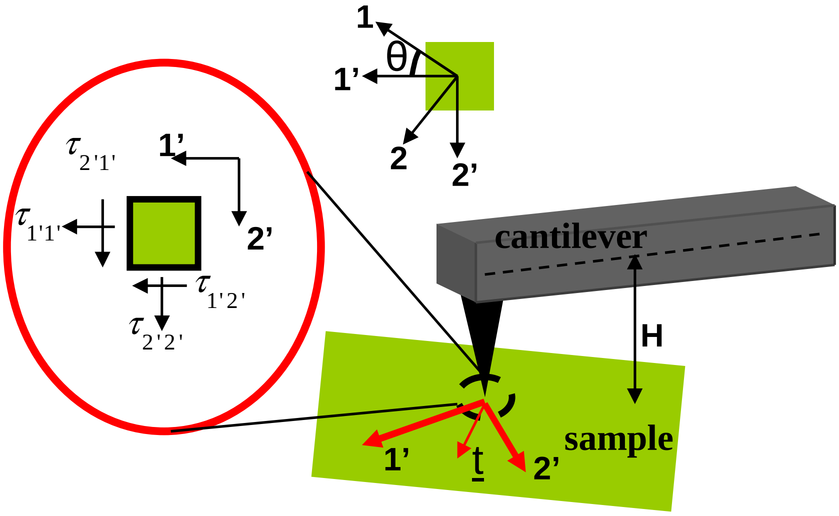

Figure A.1 Forces acting at a Tip-Sample Interface Direction 1' is parallel to the long axis of the cantilever and, hence, along the scanning direction. The coordinate system (1'-2') is oriented at an angle θ with respect to the principal coordinate system (1-2). The zoomed in figure shows the planar stress distribution on an infinitesimal area element of the sample.

Consider a small area element of a sample, with an in-plane normal **n** coinciding with the long axis of the cantilever (along 1'), as shown in Figure A.1. Traction exerted by the tip on this area element is given by[226]:

$$\mathbf{t} = \boldsymbol{\tau} \cdot \mathbf{n},$$

$$\mathbf{t} = \begin{bmatrix} \tau_{1'1'} & \tau_{1'2'} \\ \tau_{2'1'} & \tau_{2'2'} \end{bmatrix} \begin{bmatrix} 1 \\ 0 \end{bmatrix} = \begin{bmatrix} \tau_{1'1'} \\ \tau_{2'1'} \end{bmatrix} = \tau_{1'1'}\,\mathbf{e}_{1'} + \tau_{2'1'}\,\mathbf{e}_{2'},$$

where τ_{ij} = components of in-plane stress tensor,

n = area element normal pointing in 1' direction,

$\mathbf{e}_{1'}$ = unit vector along 1' direction,

$\mathbf{e}_{2'}$ = unit vector along 2' direction.

The component of the traction, which is perpendicular to the axis of the cantilever ($\tau_{2'1'}$), will give rise to a torque about the cantilever beam axis and results in cantilever twisting. The TSM torque (*T*) is given by:

$$T = HA\tau_{2'1'} \qquad \text{(A)}$$

where *H* is the vertical distance between the cantilever beam axis and the contact plane and *A* is the area of the sample.

Let γ be a uniaxial strain applied by the tip in direction 1', which is rotated by θ degrees with respect to the principal crystallographic axis 1. The components of the stress tensor in the 1'-2' coordinate system are given by the generalized Hooke's law:

$$\begin{bmatrix} \tau_{1'1'} \\ \tau_{2'2'} \\ \tau_{1'2'} \end{bmatrix} = \begin{bmatrix} C_{1'1'} & C_{1'2'} & C_{1'3'} \\ C_{2'1'} & C_{2'2'} & C_{2'3'} \\ C_{3'1'} & C_{3'2'} & C_{3'3'} \end{bmatrix} \begin{bmatrix} \gamma \\ 0 \\ 0 \end{bmatrix}$$

where $C_{1'1'}$ through $C_{3'3'}$ are components of the reduced elastic modulus tensor. By using the above notation, $\tau_{2'1'}$ can be expressed as:

$$\tau_{2'1'} = C_{3'1'}\gamma. \tag{B}$$

From (A) and (B),

$$T = HAC_{3'1'}\gamma. \tag{C}$$

According to equation (C), the TSM torque (*T*) depends on only one component of the elastic tensor, $C_{3'1'}$. Now, let us consider a general case where the reduced elastic modulus tensor, with respect to principal crystallographic coordinates 1, 2, 3, is given by[226]:

$$\begin{bmatrix} C_{11} & C_{12} & C_{13} \\ C_{21} & C_{22} & C_{23} \\ C_{31} & C_{32} & C_{33} \end{bmatrix} \tag{D}$$

The elastic constant tensor is a fourth order tensor. The components of the elastic tensor are written in reduced Voigt matrix notation as C_{mn}, where *m* and *n* are each indices corresponding to a pair of indices *ij* or *kl* in the *unreduced* form, according to the following conversion:

m or *n*	*ij* or *kl*
1	11

2	22
3	12
3	21

Using this matrix conversion and the reduced elastic tensor in (D), the components of the *unreduced* elastic tensor can be written as:

$$C_{1111} = C_{11},$$

$$C_{2222} = C_{22},$$

$$C_{1122} = C_{2211} = C_{12},$$

$$C_{1221} = C_{2112} = C_{1212} = C_{2121} = C_{33},$$

$$C_{1112} = C_{1121} = C_{1211} = C_{2111} = C_{13},$$

$$C_{2212} = C_{2221} = C_{1222} = C_{2122} = C_{23},$$

We are interested in only $C_{3'1'}$, as the twisting torque only depends on $C_{3'1'}$. $C_{3'1'}$ in the *unreduced* form, according to the matrix conversion, can be written as:

$$C_{3'1'} = C_{1'2'1'1'}\ . \tag{E}$$

$C_{1'2'1'1'}$ can be written in terms of principal crystallographic coordinate system 1, 2, 3, using rotational transformation rules for fourth order tensors, which is given by:

$$C_{1'2'1'1'} = \sum_{\alpha}\sum_{\beta}\sum_{\gamma}\sum_{\delta} Q_{\alpha 1} Q_{\beta 2} Q_{\gamma 1} Q_{\delta 1} C_{\alpha\beta\gamma\delta}, \tag{F}$$

where Q_{ij} is given by:

$$\begin{bmatrix} Q_{11} & Q_{12} \\ Q_{21} & Q_{22} \end{bmatrix} = \begin{bmatrix} \cos\theta & -\sin\theta \\ \sin\theta & \cos\theta \end{bmatrix}, \tag{G}$$

and α, β, γ, and δ can be either 1 or 2. Using equations (E), (F), and (G), $C_{3'1'}$ can be expressed as:

$$\begin{aligned} C_{3'1'} = {} & Q_{11}^3 Q_{12} C_{1111} + Q_{11}^2 Q_{12} Q_{21} C_{1112} + Q_{11}^2 Q_{12} Q_{21} C_{1121} + Q_{11}^3 Q_{22} C_{1211} + \\ & Q_{21}^2 Q_{11} Q_{12} C_{1122} + Q_{11}^2 Q_{21} Q_{22} C_{1212} + Q_{11}^2 Q_{21} Q_{22} C_{1221} + Q_{21}^2 Q_{11} Q_{22} C_{1222} + \\ & Q_{11}^2 Q_{21} Q_{12} C_{2111} + Q_{21}^2 Q_{12} Q_{11} C_{2112} + Q_{21}^2 Q_{12} Q_{11} C_{2121} + Q_{11}^2 Q_{21} Q_{22} C_{2211} + \\ & Q_{21}^3 Q_{12} C_{2122} + Q_{21}^2 Q_{22} Q_{11} C_{2212} + Q_{21}^2 Q_{22} Q_{11} C_{2221} + Q_{21}^3 Q_{22} C_{2222} \end{aligned}$$

$$\begin{aligned} = {} & C_{11}(-\cos^3\theta\sin\theta) + C_{22}(\cos\theta\sin^3\theta) + C_{33}(2\cos^3\theta\sin\theta - 2\cos\theta\sin^3\theta) + \\ & C_{12}(\cos^3\theta\sin\theta - \cos\theta\sin^3\theta) + C_{13}(-3\cos^2\theta\sin^2\theta + \cos^4\theta) + \\ & C_{23}(3\cos^2\theta\sin^2\theta - \sin^4\theta) \end{aligned}$$

Using the above equation for $C_{3'1'}$, and inserting in equation (C), the *TSM* torque (*T*) can be written as:

$$\begin{aligned} T = HA\gamma[& C_{11}(-\cos^3\theta\sin\theta) + C_{22}(\cos\theta\sin^3\theta) + C_{33}(2\cos^3\theta\sin\theta - 2\cos\theta\sin^3\theta) + \\ & C_{12}(\cos^3\theta\sin\theta - \cos\theta\sin^3\theta) + C_{13}(-3\cos^2\theta\sin^2\theta + \cos^4\theta) + \\ & C_{23}(3\cos^2\theta\sin^2\theta - \sin^4\theta)] \end{aligned}$$

The elastic modulus constants can now be replaced by the most general form of writing fourth order tensor components with quadruple subscripts.

$$\begin{aligned} T = HA\gamma[& E_{1111}(-\cos^3\theta\sin\theta) + E_{2222}(\cos\theta\sin^3\theta) + 2E_{1212}(2\cos^3\theta\sin\theta - 2\cos\theta\sin^3\theta) + \\ & E_{1122}(\cos^3\theta\sin\theta - \cos\theta\sin^3\theta) + 2E_{1112}(-3\cos^2\theta\sin^2\theta + \cos^4\theta) + \\ & 2E_{2212}(3\cos^2\theta\sin^2\theta - \sin^4\theta)] \end{aligned}$$

The above mathematical equation for the TSM torque (*T*) is general and can be used to calculate the TSM signal based on the components of the elastic modulus tensor and the scanning direction. In order to check the validity of the above equation for TSM signal, we compared it with our experimental data.

For the TSM calculations, we took the (1-2) plane as the (**a**-**b**) plane because the crystal plane under analysis is the **a**[100]-**b**[010] plane of pentacene. We tried to fit the calculations based on our experimental results. The fit can be used to calculate the relative **a**-**b** plane elastic constants for pentacene single crystals which are: $E_{1111} \sim 1.8\ E_{2222}$, $E_{1212} \sim 0.2\ E_{2222}$, $E_{1122} \sim 0.6\ E_{2222}$, $E_{1112} \ll E_{2222}$, and $E_{2212} \ll E_{2222}$. In order to verify the accuracy of the fit, we compared the obtained relative magnitudes of elastic constants of pentacene with that of anthracene single crystal.[134] The similar molecular structure and herringbone packing of anthracene and pentacene molecules makes anthracene's elastic constants an excellent choice, as the relative magnitudes of different elastic constants should be similar in the two organic crystals. In fact, a good agreement between the relative magnitudes of elastic constants in the two crystals indicates that the origin of TSM is elastic anisotropy at the sample surface, and that the mechanical elasticity model can predict the TSM signal.

Appendix B

Transverse Shear Signal for an Isotropic Material

(Contributing Authors: Vivek Kalihari, E. B. Tadmor, Greg Haugstad, C. Daniel Frisbie)
(Reprinted with permission from *Advanced Materials* 20 (2008))

In this appendix, we will describe the transverse shear signal based on the mechanical model (derivation given in Appendix A) for an elastically isotropic material. According to the derivation in Appendix A, the torque exerted on the cantilever depends on only one component of the elastic tensor, $C_{3'1'}$.

$$T = HAC_{3'1'}\gamma. \tag{A}$$

Let us consider the case where the sample is an isotropic elastic solid for which the reduced elastic constant tensor, with respect to principal crystallographic coordinates 1, 2, 3, is given by:

$$\begin{bmatrix} C_{11} & C_{12} & C_{13} \\ C_{21} & C_{22} & C_{23} \\ C_{31} & C_{32} & C_{33} \end{bmatrix} = \begin{bmatrix} \lambda+2\mu & \lambda & 0 \\ \lambda & \lambda+2\mu & 0 \\ 0 & 0 & \mu \end{bmatrix}, \tag{B}$$

where λ is the Lamé constant, and μ is the shear modulus.

The elastic constant tensor is a fourth order tensor. The components of the elastic tensor are written in reduced Voigt matrix notation as C_{mn}, where m and n are each indices corresponding to a pair of indices ij or kl in the *unreduced* form, according to the following conversion:

m or *n*	*ij* or *kl*
1	11

2	22
3	12
3	21

Using this matrix conversion and the reduced elastic isotropic tensor in (B), the components of the *unreduced* elastic tensor can be written as:

$$C_{1111} = C_{2222} = \lambda + 2\mu,$$

$$C_{1122} = C_{2211} = \lambda,$$

$$C_{1221} = C_{2112} = C_{1212} = C_{2121} = \mu,$$

$$\text{all other } C_{ijkl} = 0.$$

We are interested in only $C_{3'1'}$, as the twisting torque only depends on $C_{3'1'}$. $C_{3'1'}$ in the *unreduced* form, according to the matrix conversion, can be written as:

$$C_{3'1'} = C_{1'2'1'1'}\ . \tag{C}$$

$C_{1'2'1'1'}$ can be written in terms of principal crystallographic coordinate system 1, 2, 3, using rotational transformation rules for fourth order tensors, which is given by:

$$C_{1'2'1'1'} = \sum_{\alpha}\sum_{\beta}\sum_{\gamma}\sum_{\delta} Q_{\alpha 1}Q_{\beta 2}Q_{\gamma 1}Q_{\delta 1}C_{\alpha\beta\gamma\delta}, \tag{D}$$

where Q_{ij} is given by:

$$\begin{bmatrix} Q_{11} & Q_{12} \\ Q_{21} & Q_{22} \end{bmatrix} = \begin{bmatrix} \cos\theta & -\sin\theta \\ \sin\theta & \cos\theta \end{bmatrix}, \tag{E}$$

and α, β, γ, and δ can be either 1 or 2. Using equations (C), (D), and (E), $C_{3'1'}$ can be expressed as:

$$
\begin{aligned}
C_{3'1'} &= Q_{11}^{3}Q_{12}C_{1111} + Q_{21}^{3}Q_{22}C_{2222} + Q_{11}^{2}Q_{21}Q_{22}C_{1221} + Q_{21}^{2}Q_{11}Q_{12}C_{2112} + \\
&\quad Q_{21}^{2}Q_{11}Q_{12}C_{1122} + Q_{11}^{2}Q_{21}Q_{22}C_{2211} + Q_{11}^{2}Q_{21}Q_{22}C_{1212} + Q_{21}^{2}Q_{11}Q_{12}C_{2121} \\
&= (-\cos^{3}\theta\sin\theta + \cos\theta\sin^{3}\theta)(\lambda + 2\mu) + (\cos^{3}\theta\sin\theta - \cos\theta\sin^{3}\theta)\lambda + \\
&\quad (2\cos^{3}\theta\sin\theta - 2\cos\theta\sin^{3}\theta)\mu \\
&= 0.
\end{aligned}
$$

The above mathematical formulation shows that for an *isotropic* material, $C_{3'1'}$ or the torque about the cantilever beam axis (Equation (A)) will always be zero independent of the scan direction. This result is expected for TSM of an isotropic material. For an anisotropic material, $C_{3'1'}$ will be a function of θ and, hence, the cantilever twist generally will be *non- zero* and will depend on the scanning direction. Depending on the symmetry of packing in anisotropic materials, the cantilever twist can be zero in some directions.

Appendix C

Calculation of Diffusion Activation Energy of Pentacene on Silicon Dioxide

(Contributing Authors: Vivek Kalihari, E. B. Tadmor, Greg Haugstad, C. Daniel Frisbie)
(Reprinted with permission from *Advanced Materials* 20 (2008))

Here, we describe the calculation of diffusion activation energy (E_D) of pentacene molecule on SiO_2 surface. In the complete condensation (no desorption) regime, energy of nucleation (E_N) is given by:

$$E_N = \frac{E_i + iE_D}{(i+2)} \tag{C.1}$$

where i is the critical number of molecules required to form a stable cluster, E_D is the activation energy of diffusion, and E_i is the difference in free energy between i adsorbed molecules on the substrate (freely-diffusing) and i molecules in a cluster. Ruiz *et al.*[25] performed a detailed analysis on the cluster size distribution of pentacene on SiO_2 and reported $i = 3$.

Monolayer films of pentacene were deposited on SiO_2 at different substrate temperatures (25°C to 55°C) in order to measure the grain size variation with growth temperature. The above temperature regime was chosen as no desorption of pentacene molecules from SiO_2 was observed. According to the basic rate equations formulated by Venables *et al.*[165], the growth system can be characterized as being in the complete condensation regime. An Arrhenius plot (Figure 5.8) of the grain size (an effective radius) versus the substrate temperature (T) gives the activation energy of nucleation (E_N ~ 800 meV) for pentacene crystallites on SiO_2.

Figure C.1 shows the a[100]-b[010] plane view of pentacene molecules packed in a herringbone motif. The free energy of a three molecule cluster is estimated by using the reported interaction energies between two pentacene molecules in various crystallographic directions in a herringbone arrangement on inert substrates[166]: I [100] = 0.293eV, I [010] = 0.035eV, I [110] = 0.438eV, and I $[\bar{1}10]$ = 0.417eV. For example, the circled region in Figure C1 shows one possible cluster of three pentacene molecules and the corresponding interaction energy is given by I [100] + I [110] + I $[\bar{1}10]$. This particular configuration is termed as configuration 1 and there are six possible ways in which three pentacene molecules can form a cluster such that their interaction energy is given by the energy of configuration 1. Table C.1 lists all the possible configurations and the corresponding energies.

Nucleation is a totally random phenomenon, and thus any three pentacene molecules can come close together, without any preferred orientation and pack in a herringbone motif. So all the listed configurations are equally probable and the approximate value of the interaction energy of a three molecule cluster is calculated by taking the weighted average of possible configurations (~ 0.978eV). In the above calculation, the molecule-substrate interaction is neglected because the molecules are standing upright on the substrate.

The energy of three freely diffusing pentacene molecules on SiO_2 is approximated to be 3kT ~ 0.086eV, where k is the Boltzmann constant and T is the temperature at which pentacene molecules start desorbing from SiO_2 (*i.e.*, 60°C). The difference between these two energies is the estimated value of E_i ~ 0.892eV. Using equation (A) the activation energy of diffusion of pentacene on SiO_2 (E_D) is calculated to be approximately 1 eV.

Configurations	Energy (eV)	No. of possibilities
Configuration 1	$I[100]+I[110]+I[\bar{1}10] = 1.148$	6
Configuration 2	$I[010]+I[110]+I[\bar{1}10] = 0.890$	6
Configuration 3	$I[110]+I[110] = 0.876$	2
Configuration 4	$I[\bar{1}10]+I[\bar{1}10] = 0.834$	2

Table C.1 Interaction Energies of Stable Clusters Table summarizing number of ways in which three pentacene molecules can pack in a herringbone pattern and their corresponding energies. All the energy calculations are based on the theoretical interaction energies, reported by Verlaak et al.[166]

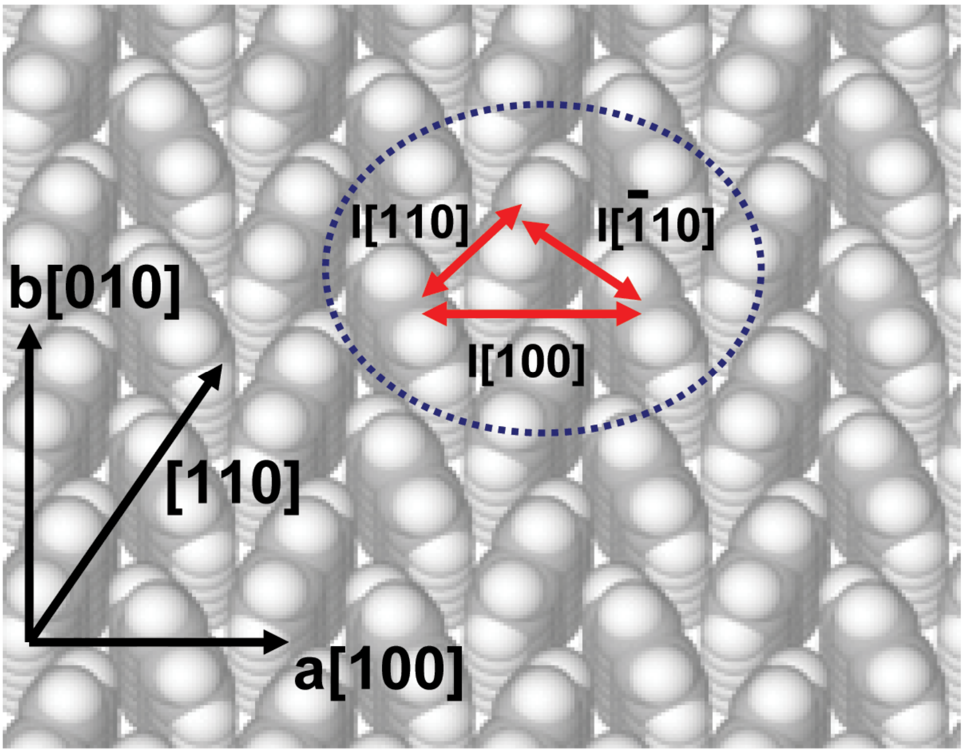

Figure C.1 Interaction Energy between Pentacene Molecules in a Herringbone Packing The figure depicts the herringbone packing motif of pentacene molecules on SiO_2. The energy of a three molecule cluster is estimated by using the interaction energies reported by Verlaak *et al.*,[166] for pentacene molecules in various crystallographic directions on inert substrates. The circled region shows one such cluster and the corresponding energy is given by I [100] + I [110] + $I[\bar{1}10]$.

Appendix D

Proposed Growth Model of Pentacene Monolayer on SiO_2

As seen in Chapter 2, growth morphology depends greatly on deposition parameters. Depending on the deposition rate and substrate temperature, different morphologies of first monolayer on a substrate can be obtained. The operating parameters I used for the single monolayer growth of pentacene thin film on silicon dioxide are:

- Substrate temperature = 50°C
- Deposition rate = 0.01-.02 Å/sec
- Operating pressure = 1 x 10^{-6} torr

The above parameters were used because minimum grain boundary density can be obtained by increasing the substrate temperature and decreasing the incoming flux to the substrate. The lowest possible deposition rate was limited by the sensitivity of the Quartz Crystal Microbalance (QCM), which was 0.01 Å/sec. 50°C was chosen as the substrate temperature because at a deposition rate of 0.01 Å/sec, considerable re-evaporation of pentacene admolecules was observed above 60°C. This observation was based on the difference between the QCM reading (nominal thickness) and the real coverage on the substrate.

Thin films with different substrate coverages were grown and then imaged using TSM to get snap shots of various stages of pentacene monolayer growth on SiO_2. At 50 $^{\circ}$C, the first pentacene monolayer was seen to completely coalesce around a nominal thickness of 16 Å. Figure D.1 shows the TSM images of first pentacene monolayer on SiO$_2$ at different stages of growth. Island heights on the substrate are same as the length

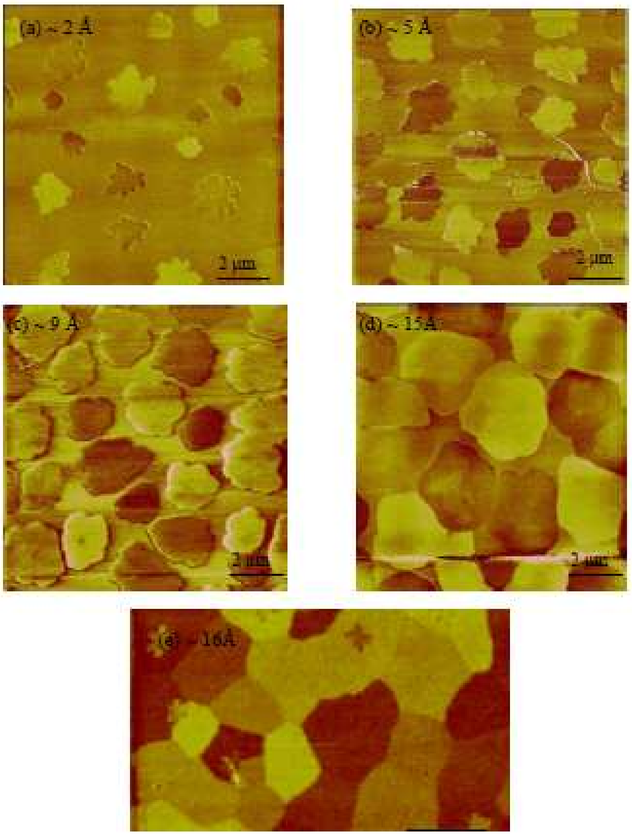

Figure D.1 TSM images of different stages of pentacene monolayer growth on SiO$_2$. Nominal thickness: (a) ~2Å, (b) ~5Å, (c) ~9Å, (d) ~15Å and (e) ~16Å

of the pentacene molecule along its long molecular axis, indicating that the pentacene molecules are standing upright on the SiO$_2$ substrate. The dendritic shape of the growing islands in the initial stage of growth indicates that the initial growth stage is diffusion limited. Islands loose their dendritic shape after a certain stage of growth and become smoother, and then they grow as more compact islands till they coalesce. The growth and the coalescence process can be treated separately for this system because the TSM images indicate that the coalescence takes place only in the final stage of the growth for all the grains.

In the proposed growth model desorption of molecules from the substrate is not taken into account because it was observed that at 50°C the substrate coverage is same as the nominal coverage. To confirm this point, a single monolayer pentacene film was grown on SiO_2 and the film was not quenched right after the growth but was kept at 50°C for an hour, and there was no indication of desorption of pentacene molecules from the substrate. The change in the shape of growing islands suggests a change in the dominating mechanism which governs the grain growth. In the following section I will address this critical point. To make the growth mechanism more clear, the nucleation and growth of first monolayer of pentacene on SiO_2 is divided into three different stages. Stage 1 covers nucleation, stage 2 describes the initial growth mechanism which gives rise to dendritic islands and stage 3 discusses the final growth mechanism which gives rise to compact islands and the coalescence process.

Stage 1

Initial nucleation process is expected to be spatially homogeneous throughout the substrate, especially on atomically flat, inert substrate like SiO_2. Stochastically nucleation is defined as the probability of meeting of a critical number of molecules together, moving randomly on the substrate, at a particular time and position. Figure D.2 shows diffusing flat lying pentacene molecules on SiO_2. When the critical number of pentacene molecules come together to form a stable island, the molecules flip and stand upright on SiO_2. The minimum number of pentacene molecules required to stabilize a cluster is four (Fig. D.2).[25]

Low deposition rate (as in my case) results in fewer pentacene molecules diffusing on SiO_2 per unit time per unit area, so the probability of forming a stable nucleus is less which gives rise to low nucleation density. Nucleation process will continue till the distances between the stable nuclei are comparable to the diffusion length of the pentacene molecules on SiO_2 because after that growth of stable nuclei will take place. Diffusion length of pentacene molecules diffusing on SiO_2 increases with temperature and hence the nucleation density decreases with an increase in substrate temperature.

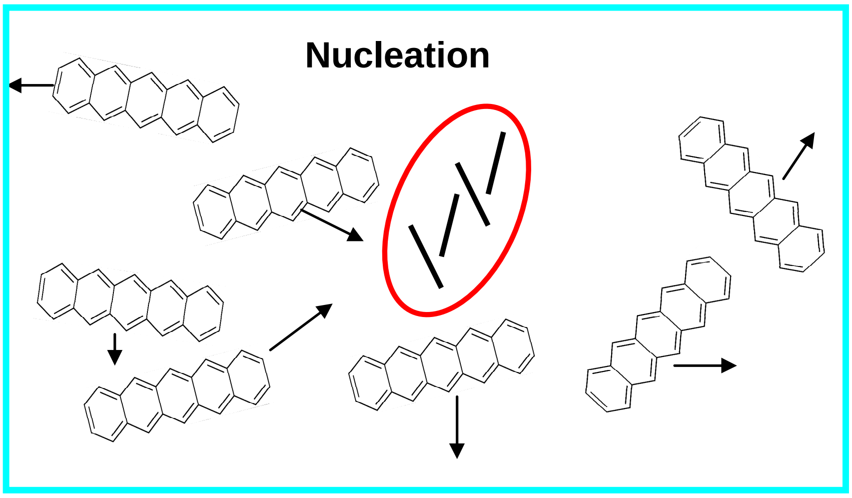

Figure D.2 Schematic showing stage 1 of pentacene monolayer growth on SiO_2 (nucleation process)

Time involving the formation of stable nuclei is much less compared to the total time of growth of the first monolayer, but the nucleation density itself determines the final grain size. Once enough stable nucleating centers are formed on the substrate, they start interacting with the neighboring centers to create depletion zones around them and the nucleation density saturates. In literature, this particular phenomenon has been described by the Capture Zone model.[49] The same island density is observed at different growth stages indicating that no secondary nucleation takes place during the growth and the concerned system fits well into the capture zone model. Fig.D.3 shows the comparison between the capture zone model and the obtained polycrystalline pentacene monolayer film on SiO_2.

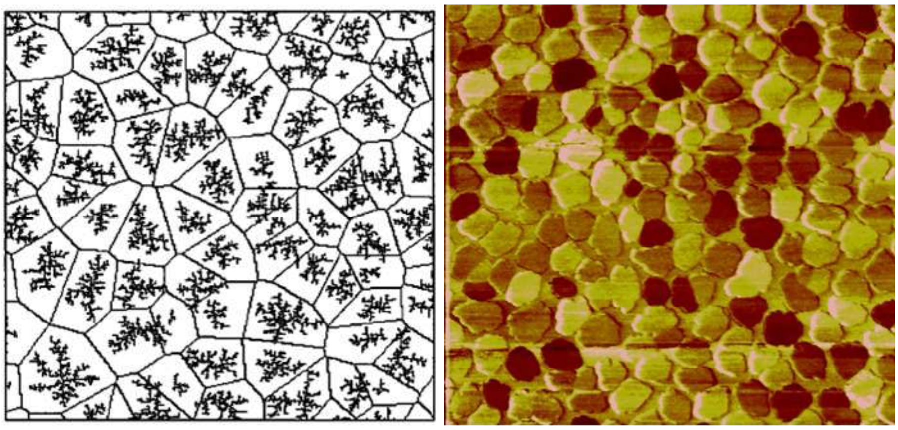

Figure D.3 Comparison between the Capture Zone Model and the experimentally obtained TSM image of pentacene monolayer on SiO_2[49]

Stage 2

$$\frac{d(n_x w_x)}{dt} = (i+1)U_i + \sigma_x D n_1 n_x + RZ$$

The above equation is same as the equation 2.6 which describes different mechanisms which contribute to grain growth. The first term in the right describes the incorporation of molecules to form a stable nucleus and can be neglected for the growth stages. In the second term, D is the diffusion coefficient of molecules on the substrate and this term dominates the growth when the island growth is dominated by the incorporation of diffusing molecules on the substrate. In the third term, Z denotes the surface coverage and the grain growth is controlled by this term at high covergaes or at high temperatures where there is significant re-evaporation of admolecules from the substrate. In case of monolayer growth of pentacene on SiO_2, there are two sources of incoming flux: (a) molecules which land on SiO_2, diffuse on SiO_2 and get incorporated into the growing pentacene islands and (b) molecules which land on top of the growing pentacene island, diffuse on the pentacene island and then jump down to SiO_2 and get incorporated at the island edge. Initial dendritic structure of the islands suggests Diffusion Limited Aggregation, where the pentacene molecules diffusing on SiO_2 controls the growth i.e. the second term in the equation 2.6 dominates.

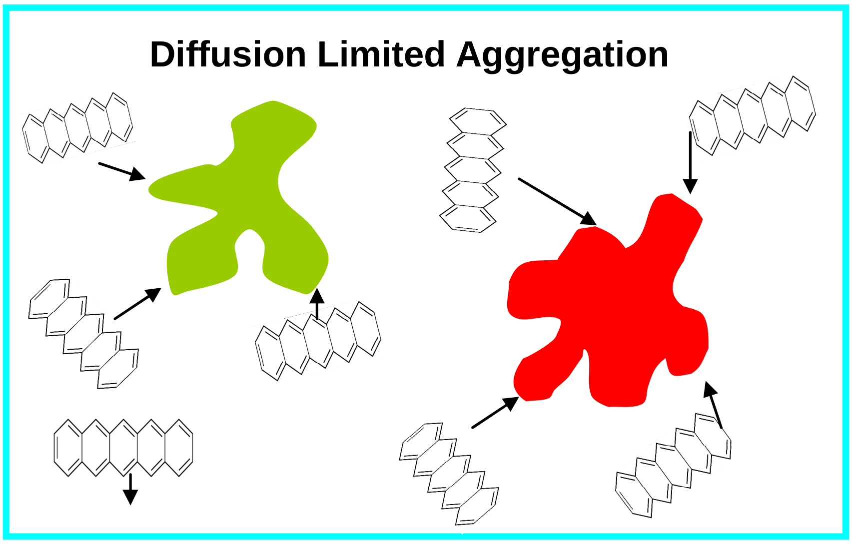

Figure D.4 Schematic showing Diffusion Limited Aggregation. Red and green dendrites are stable growing islands and incorporation of diffusing flat lying pentacene molecules on SiO_2 is the dominating mechanism which governs the grain growth (diagram not to scale)

In Diffusion Limited Aggregation atoms randomly diffuse on the substrate and whenever they encounter any island, they get incorporated because the sticking coefficient of the molecule incorporation into an island is approximately one. Figure D.4 shows the stable dendritic island growth by the incorporation of diffusing pentacene molecules on SiO_2. The diagram is not to the scale because the flat lying pentacene molecules are shown to be comparable in size with the growing dendritic islands, but in reality pentacene molecules are very small compared to the dendritic islands. Dendritic shape does not provide much projected area for the incoming atoms to sit on the stable islands; therefore the second source of incoming flux can be neglected in the initial growth stages. Low deposition rates ensure that the density of pentacene molecules on SiO_2 is low enough so that the molecules can perform Brownian motion and get attached to the growing island whenever they encounter any island edge, giving rise to a dendritic island shape in the process.

Stage 3

As the coverage of the substrate increases, the second source of incoming flux comes into picture, *i.e.*, the third term in equation 2.6 becomes dominating. The change of shape from the dendrites to the compact looking islands can be attributed to this second source of incoming flux, as shown in Fig.D.5.

As an island grows the projected area of an island increases for the incoming flux of molecules and it results in a number of molecules directly landing on top of an island. Distribution of pentacene molecules on top of the first pentacene monolayer islands is homogeneous and the probability of any molecule to diffuse to the tip of the dendritic branch, make a jump and get incorporated at the tip is very less. Instead, a molecule will find the nearest edge and will diffuse to that edge and get incorporated after jumping down to the substrate, and this process will make islands more compact in shape.[226] The probability of a molecule to jump from the first monolayer to the substrate depends on the value of Ehrlich-Schwoebel barrier. Ehrlich-Schwoebel barrier is defined as the energy barrier associated with the movement of an atom from the nth layer to (n-1)th layer.[226, 226] Almost complete coverage of the first pentacene monolayer before the start of the second layer growth indicates that this energy barrier is less for the movement of pentacene molecules from the second layer to the first layer.

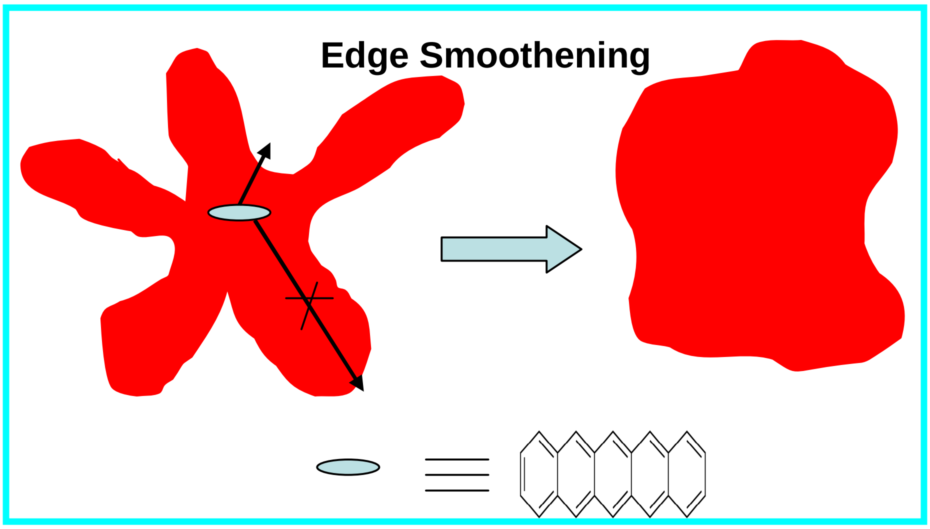

Figure D.5 Schematic showing diffusion of admolecule from top of the first monolayer to the substrate at the edge of an island

The movement of atoms from the first monolayer to the substrate can also be understood in terms of bond strength. When a molecule jumps down onto the substrate and gets incorporated into the growing face, it gets stabilized by the edge to face quadrupole interaction with the neighboring molecules. This extra stability acts as a driving force for the molecules to jump from the first monolayer to the substrate and get incorporated into the growing island. Islands continue to grow, form compact shapes and finally coalescence occurs where the molecules fill in the space between the growing islands giving completely coalesced pentacene first monolayer on SiO_2.

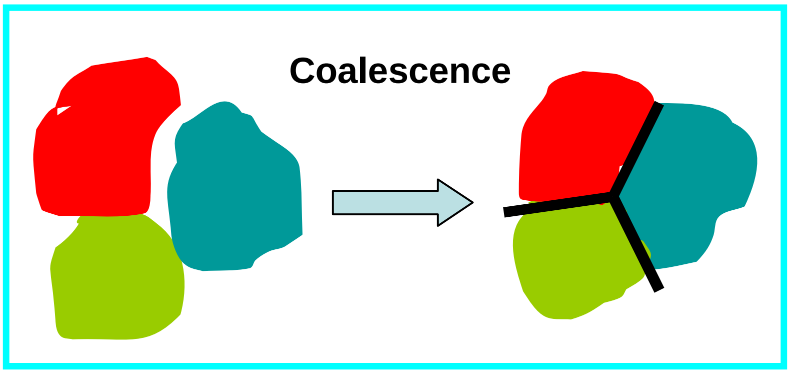

Figure D.6 Final growth stage: Grain Coalescence

Figure D.6 shows that during the coalescence there is again a change in shape of the grains, from compact rounded to compact faceted. These facets suggest the possibility of some preferred crystallographic planes and some preferred grain boundary angles. This faceted grain structure also suggests some form of quasi-equilibrium state and is discussed in detail in Chapter 5.

Appendix E

Physical Vapor Deposition of Organic Semiconductor Thin Films

Deposition of ultra-thin organic semiconductor films on solid substrates from the vapor phase is performed in a modified thermal evaporation system from Denton Vacuum (model DV-502). The vacuum system consists of a stainless steel chamber and a glass bell jar. The vacuum system is evacuated with the help of a water cooled diffusion pump (main pump) and an oil-sealed mechanical pump (backing pump), allowing for pressures in the range of $1x10^{-6}$ to $1x10^{-7}$ torr. A liquid nitrogen cooled trap and a baffle separates the diffusion pump from the main chamber, in order to avoid the heated oil molecules from the diffusion pump to enter into the main chamber. The source material is placed in an alumina crucible and resistively heated with a Luxel Radak I furnace coupled with a K type thermocouple and an external Eurotherm controller. The source temperature can be controlled in the range 22-1500°C. The substrates are attached to the substrate holder with a screw and clamp system. The substrate holder is mounted to a resistively-heated, water cooled sample stage which in turn is connected to cartridge-type heater, K type thermocouple and water lines. Sample stage is also coupled with an external Eurotherm to control the temperature of the sample stage in the range 25-350°C. In-situ film thickness is measured with an Inficon quartz crystal microbalance (QCM) which is placed near the sample stage and has got a sensitivity of 0.01Å/s.

Most of the organic semiconductor ultra-thin films are grown on SiO_2. For an ultra-thin film formation the substrate plays an important role. It is very important to have substrates that are relatively free of particles to prevent heterogeneous nucleation during the organic thin film growth. Heterogeneous nucleation can drastically change the final morphology of the ultra-thin films. After introducing the substrate and the source in the main chamber, the chamber is pumped down to the desired pressure. The source is preheated (~100°C) to get rid of the moisture. After reaching the desired vacuum inside the main chamber the source temperature is slowly ramped up to the sublimation temperature of the source material. During the initial stages of heating a shutter obstructs the sample holder form the view of the source crucible. This prevents any low molecular weight organic molecule in the source crucible from deposition onto the substrate. After reaching the sublimation temperature of the source material the shutter is opened and the thickness of the deposited film on the substrate is monitored in-situ with the help of the QCM.

The QCM thickness measurement system, with a high sensitivity of ~0.01 Å/s, is capable of monitoring the thickness within a few Å. The calibration between the QCM monitored thickness and the actual thickness is very sensitive to the relative alignment of the substrate and the source crucible. The tooling factor in the QCM takes care of the alignment between the source and the substrate. Multiple samples are grown with different thicknesses (*i.e.*, different thickness readings on the QCM) and then AFM is used to measure the actual deposited thickness. A comparison is drawn between the actual thickness and the QCM thickness number in order to get the right tooling factor, which differs for different source materials.

After growing the desired thickness of the thin film, the shutter is closed again and the source crucible and the substrate holder are water-cooled. When the source crucible cools down to ~60^0C, the vacuum chamber is isolated from the pumping system and the nitrogen gas is vented in to remove the glass bell jar and to take out the substrate.

Figure E.1 Physical Vapor Deposition Chamber

Additional references for Appendices:

227) J. P. Hirth, J. Lothe, *Theory of Dislocations* Ch.2 (Wiley, New York, 1982)

228) T. C. T. Ting, *Anisotropic Elasticity* (Oxford Univ. Press, New York, 1996)

229) Y. Luo, G. Wang, J. A. Theobald and P. H. Beton, *Surface Science*, **537** 241 (2003)

230) G. Ehrlich and F. G. Chzran, *Journal of Chemical Physics*, **44** 1039 (1966)

231) R. L. Schwoebel, *Journal of Applied Physics*, **40** 614 (1968)